**Title**

Anion Exchange Doping in Semiconducting Polymers



**Author**

Mehmedović, Zerina

**Publication Date**

2024

Peer reviewed|Thesis/dissertation

UNIVERSITY OF CALIFORNIA

Los Angeles

# Anion Exchange Doping in Semiconducting Polymers

A dissertation submitted in partial satisfaction of the

requirements for the degree Doctor of Philosophy

in Chemistry

by

Zerina Mehmedović

2024

ABSTRACT OF THE DISSERTATION

Anion Exchange Doping in Semiconducting Polymers

by

Zerina Mehmedović

Doctor of Philosophy in Chemistry

University of California, Los Angeles, 2024

Professor Benjamin J. Schwartz, Chair

Conjugated polymers (CPs) are organic semiconducting materials that offer a promising alternative to inorganic semiconductors as they are flexible, inexpensive, and solution-processable. The biggest challenge in integrating CPs into thermoelectric and other devices is their limited electrical conductivity, especially in comparison to their inorganic counterparts. Recent efforts have focused on enhancing the performance of CPs by using another molecule to dope the polymer and create charge carriers. The sequential processing (SqP) method [Aguirre et. al. Adv. Energy Mater. 2015, 1402020], developed by our group, works by casting the polymer and dopants from semi-orthogonal solvents. By separating the polymer and doping casting steps, the polymer has enough time to aggregate, allowing control over the polymer crystallinity by changing the regioregularity or polymer processing conditions. Using SqP, we can study the effects of tuning the polymer crystallinity with anion-exchange (AX) doping, in which a high concentration of inert

salt anion accompanies the introduction of the dopant [Yamashita et. al. Nature 572,634-638 (2019)]. In this dissertation, we will explore how introducing a molecular oxidant with and without an inert salt affects the conductivity of polymers with different crystallinities; we also will examine new spectroscopic features associated with AX doping that to date have been unassigned in the literature. The first chapter of this dissertation gives an overview of conjugated polymers, different doping mechanisms, and the tools we use to analyze doped-polymers including absorption, x-ray diffraction, and electrical Hall effect measurements. In chapter two we focus on AX doping and how the new doping mechanism affects the electrical properties of a well-studied polymer with varying crystallinities. Chapter three explores two new spectroscopic features that appear when using high concentration dopant and salt during the AX doping process. Using Resonance Raman spectroscopy and quantum chemistry calculations, we are able to assign these peaks to a salt-dopant complex that is formed during the exchange process. Chapter four explores the doping mechanism of a very strong oxidant that has been recently introduced to the polymer literature. Although there is debate on if the dopant counterion infiltrates the entirety of the polymer or just the amorphous regions, we show that the dopant does affect the crystal structure, indicating its intercalation into crystalline sites. Finally, chapter five discusses theoretical calculations on tungsten tetraboride, a synthetic inorganic material that has been discovered to have superhard characteristics. This chapter explores the various bonding properties of tungsten tetraboride to understand if the hardening affects are due to extrinsic or intrinsic affects. Although many unsolved questions remain in the conjugated polymer field, this dissertation breaks ground as foundational work in understanding new doping methods and molecular oxidants that have been introduced into the field.

The dissertation of Zerina Mehmedović is approved.

Justin R. Caram

Alexander M. Spokoyny

William M. Gelbart

Benjamin J. Schwartz, Committee Chair

University of California, Los Angeles

2024

*For my parents, Zijad and Zulfa, who scarified everything to give me this opportunity.*

*For my brother, Adnan, who would have fought anyone who got in my way.*

*For Selina, Stella, and Zayla. I am paving the way, so your road is not as treacherous.*

*For the rest of the Hodžić and Mehmedović family, who fought to survive the 1990s and every day afterwards.*

*For Bosnia and Herzegovina.*

*Nisam bila tu, ali borim se svaki dan za Bosnu moju.*

TABLE OF CONTENTS

# LIST OF FIGURES

# LIST OF TABLES

# ACKNOWLEDGEMENTS

From the first day of graduate school, I have been dreaming about writing this section of my thesis. I thought of it as if I was receiving a grammy and I had three minutes before the music started to play and I was slowly escorted off the stage.

I have always told my students that in order to be successful, one needs a solid foundation. My foundation was built in Walnut Creek, in the halls of Las Lomas High School. I would not have explored chemistry without the influence of Suzanne Morse and James Morgan. On the first day of AP Chemistry, Mr. Morgan gave us a pop-quiz and that mentality of always expecting surprises made graduate school less…surprising.

Mrs. Morse and Mr. Morgan inspired me to obtain my bachelor's degree in chemistry from San Francisco State University (SFSU). There, I had the privilege of working with Dr. Nicole Adelstein who took me into her group without having any prior knowledge in code. While in Dr. Adelstein's group I realized I had a deep curiosity for fundamental questions that could not be quenched with only two years of exploration. Besides my undergraduate advisor, three other professors made my SFSU career and heavily influenced my decision towards graduate school: Dr. Raymond Esquerra, Dr. Andrew Ichimura, and Dr. Nancy C. Gerber. While SFSU has a large biochemistry cohort, the pure chemistry class was small and therefore very close. Each of us took all the same classes together including Esquerra's quantum chemistry course. While incredibly difficult, I remember laughing most in that class. Somehow Dr. Esquerra made solving the Schrödinger's equation fun. It particularly helped when he brought in a puppet to teach the class. Dr. Andrew Ichimura was the professor for our physical chemistry lab class. As a theorist, I took lab classes for granted but Dr. Ichimura's class was the reason I did not apply to graduate school

as a theorist. His lab class made me want to explore the possibility of being an experimentalist, which I later became! Dr. Nancy Gerber was my area advisor and to whom I owe the first two years of my time at SFSU. As a first-generation college graduate, I did not know how to navigate university, let alone what it meant to become a professor. Dr. Gerber would spend up to two hours with me exploring different classes I should take, giving me extra readings, and advising me in which groups to join. Without these four professors, I would not have gotten into UCLA's graduate program.

I entered UCLA in 2018 where I first joined Dr. Anastassia Alexandrova's group. It was the perfect group for me when I first started graduate school because I was too afraid to explore being an experimentalist; I went to where I was comfortable. I am forever grateful to Anastassia for allowing me to spend my first two years in her lab.

During the height of the COVID-19 pandemic, I decided it was time to take a leap of faith and explore the reason my degree will say 'Physical Chemistry' instead of 'Theoretical Chemistry'. I joined Dr. Benjamin Schwartz's group in August of 2020 and never looked back. Ben, you took a chance on an incoming third year and I cannot thank you for that enough. You saw through my failures and instead showcased my persistence and resilience. In your lab I have flourished as a scientist, getting to mentor both graduate and undergraduate students. I am thankful that you allowed me to "not" bring in Cinnamon nearly every day. Thank you for letting her "not" shed all over your couch. I have learned so many soft skills while in your lab that I apply to every portion of my life.

Besides my PI, I would like to thank my committee members and a few professors at UCLA who made my success in this department possible: Drs. Alex Spokoyny, Bill Gelbart, Justin Caram, and Sarah Tolbert.

Despite being busy as chair, Dr. Spokoyny gave me his immediate attention when I came to his office frantic about funding. Without a second thought, he put down what he was doing to find a solution and later came to find me to tell me, "It's handled". This gave me so much confidence and security that we had a chair that will always listen to his students.

Dr. Gelbart advocated for me before I knew how to do so myself. In my transitional period between groups, he made sure that I was heard and fought to make sure I stayed in the program. He has always been kind in lending a listening ear whenever needed. He was particularly encouraging during my 4$^{th}$ year meeting when I felt quite overwhelmed as I was doing the meeting with only two years with Ben. Professors like Dr. Gelbart are the backbone to a good experience in graduate school.

I felt like a part of Dr. Caram's group for a long time because my best friend, Dr. Ashley Shin, was in his group and took me along to their group outings. I got to teach MCTP with Justin in my 5$^{th}$ year, it was the most fun I had had while teaching in a long time. I spent a lot of my time teaching underclassmen, and it was the first time I was teaching juniors and seniors. Justin made teaching for him a lot of fun. Besides that, he made me feel seen during visitation when he told me that he remembered my application and guessed my undergraduate institution on the first guess. I felt like he had my back when I was lost and was always ready to be silly with me. Thanks Juice.

Dr. Sarah Tolbert has been an integral part of my graduate career: from being a committee member when I was working for Dr. Alexandrova, to being essentially a co-PI of mine. Dr. Tolbert

told me the truth when no one else would, saving me from a miserable time. She guided me and helped me find a group that I would thrive in. She helped me in more ways than I could possible count including being a role model for women in the department and showing us that it is okay to not know something (frequently asking the 'organic people' in solar whether something is even possible). Sarah was one of the few professors in the department that believed in my abilities before I even knew I could; without Sarah, I would not be writing this acknowledgements section at all, for that, I will always be in her debt.

Beyond instructors, I have been truly fortunate to have worked with wonderful collaborators and mentors. My academic work would not exist in its current form without the mentorship and guidance of Dr. Dane Stanfield, Dr. Quynh Duong, Dr. Eric Wu, and Alex Leon Ruiz from the Schwartz group, and Dr. Charlene Salamat and Nesibe Akmansen-Kalayci from the Tolbert group. All of them contributed greatly to my Ph.D., helping me learn how to be an experimentalist, learning how to be safe in a lab again and exploring the structural components of conjugated polymers. Besides these students, I would like to thank some of the other members of the Schwartz group namely, Kara Lo, Diego Garcia Vidales, Reid Wilson, Dr. Andy Vong, Mariah Gomez, Stephanie Jimenez, and Amanda Nguyen. Each of you played a large role in my enjoyment and merriment in the group. Amanda, my undergraduate mentee, I am so proud of you for graduating with your B.S. in Chemistry from UCLA, receiving the NSFGRFP and committing to Northwestern University for graduate school. I cannot wait to hear what you do in Chicago.

Outside of my scientific bubble, I made wonderful friends that made my time at UCLA bearable including: Ashley Shin, Alex Leon Ruiz, Austin Bailey, David Pe, Brandon Jolly, and Will Laderer to name a few. A special shout-out to Nate Juareque who listened to me whine about

graduate school for hours, despite being as far removed from the area as possible. Out of all of these names, Dr. Ashley Shin has made the biggest impact in my life.

Ashley and I met during our UCLA recruitment in February, were forced to be roommates and then decided to live together for the entirety of your graduate career. Living with my best friend for five years is the thing I feel the most lucky to have experienced in LA. Ashley has encouraged me to grow in so many different ways, both as a human being and as a scientist. She influenced me into becoming a dog person through Gogi, then Noodle, and eventually influencing me in getting my own! Living in Westwood and doing hood rat things will always be such a wonderful memory. Living with you and Morgan in the Valley will be unforgettable. This may sound like I'm exaggerating but it is the God honest truth when I say I could not have gone through this experience, written this thesis, stayed in this program, if it weren't for you. Ashley, I owe you every ounce of success I have ever received during graduate school. I am forever indebted to you.

Lastly, I would like to thank my family. Maida and Elvis, you provided a home away from home when y'all lived in LA, a cozy place where I could run away from my problems. Later you gave me the greatest gift of all, being an aunt to your daughters. I am never happier than when I am with Selina and Stella and the fact that I get to do it all over again with Zayla, elates me. Velida, I am so proud of what you have achieved. I hope we continue to grow in our family and learn how to be kind to one another. Thank you for the sleepovers where we got to practice our accents, it's the first place I got to be myself. Anida, despite our struggles, I have always looked up to you and always wanted your acceptance. Thank you for the constant laughs. Ado, I am writing this on your birthday. You turn 25 today. While I do not remember the day you were born, my greatest identity and the one I cherish the most is being your sister. I am incredibly proud of your accomplishments, and I am looking forward to what else you do.

Mama i Baba. Vi ste mi dali sve što sam ikad hitjela. Nismo mogli ući u Barnes n' Noble da mi ne kupite knjigu. Ponekad sam tužna jer se osjećam kao da sam odrasla sama. Zaboravim da ste i vi bili djeca kad ste došli ovde da date meni i Adnanu bolji život. Vidi šta ste napravili. Elhamdulilah. Imamo sve što ste ikad hitjeli: zdravlje, a bogme i pamet. Ne samo jednu kuću, nego dvije! Da bome, da bome.

I think about my grandparents often. My grandfather survived a concentration camp, my grandmother is illiterate. To go from illiterate to PhD in just two generations shows the plight of the Bosnian people. The resilience and persistence I held onto throughout my graduate career was instilled in me by my family. Their fight to survive during the Bosnian Genocide in the 1990s is truly a feat I never tire of telling.

I would not be where I am without any of these people. To all of you, thank you.

Chapter one contains parts from an unpublished perspective by Zerina Mehmedović.

Chapter two is adapted from the unpublished manuscript, "Mehmedović, Z.; Salamat, C.Z.; Akmansen-Kalayci, N.; León Ruiz, A.O.; Nguyen, A.N.; Stanfield, D.A.; Tolbert, S.H.; Schwartz, B.J. Understanding the Role of Crystallinity on Structural and Electronic Properties of Poly(3-hexylthiophene-2,5-diyl) Upon Anion-Exchange Doping. *In preparation*" Experiments: ZM, CZS, AOLR, AN; data analysis; ZM, CZS and NAK; writing: ZM, CZS and NAK; editing: all authors; advising: SHT and BJS.

Chapter three is adapted from the unpublished manuscript "Mehmedović, Z.; Nguyen, A.N.; León Ruiz, A.O.; Lo, K.; Tolbert, S.H.; Schwartz, B.J. Formation of Li-F4TCNQ Complex during High Concentration Anion-Exchange Doping of Semiconducting Polymers. *In preparation*"

Experiments: ZM, ANN, AOLR, KL; data analysis: ZM and ANN; calculations: ZM; writing: ZM; editing: all authors; advising: SHT, BJS.

Chapter four contains unpublished results, "Mehmedović, Z.; Nguyen, A.N.; Akmansen-Kalayci, N.; Slimp, A.; Tolbert, S.H.; Schwartz, B.J. Magic Blue Doping Shows Intercalation into Crystalline Sites in Doped P3HT. *In preparation*." Experiments and data analysis: ZM, ANN, NAK, AS; writing: ZM; editing: all authors; advising: SHT, BJS.

Chapter five contains the work I accomplished during my time in the Dr. Alexandrova group that was later published in "Akopov, G.; Hu, S.; Shumilov, K.D.; Hamilton, S.G.; Pangilinan, L.E.; Mehmedović, Z.; Yin, H.; Robinson, P.J.; Roh, I.; Kavner, A.; Alexandrova, A.N.; Tolbert, S.H.; Kaner, R.B. (2024). Hardening in Tungsten Tetraboride with the Addition of Carbon, Zirconium, and Silicon: Intrinsic *vs* Extrinsic Effects. *Chemistry of Materials*, 36(7), 3233-3245." This chapter only includes theoretical work that I worked on in helping publish this manuscript.

# BIOGRAPHICAL SKETCH

## Education

2020 M.S. in Chemistry, University of California Los Angeles

2017 B.S. in Chemistry, San Francisco State University

## Selected Publications

1. **Mehmedović, Z.,** Salamat, C.Z., Akmansen-Kalayci, N., León Ruiz, A.O., Nguyen, A., Tolbert, S.H., Schwartz, B.J. Understanding the Role of Semiconducting Polymer Crystallinity on Structural and Electronic Properties upon Anion-Exchange Doping. In preparation.
2. **Mehmedović, Z.,** León Ruiz, A.O., Nguyen, A., Lo, K., Tolbert, S.H., Schwartz, B.J. Li-$F_4$TCNQ Complex Formation due to High Dielectric Environment in Anion Exchange Doped Semiconducting Polymers. In preparation.
3. Salamat, C.Z., Leon Ruiz, A.O., Akmansen-Kalayci, N., **Mehmedović, Z**., Lo, K., Wu, E.C., Stanfield, D.A., Das, P., Nguyen, A., Tagawa, R., Thompson B.C., Dunn, B.S., Tolbert, S.H., Schwartz, B.J. Anion Exchange Doping of Semiconducting Conjugated Polymers is Controlled by the Local Dielectric Constant and Solvent Swelling. In preparation.
4. Stanfield, D. A., **Mehmedović, Z**., & Schwartz, B. J. (2021). Vibrational stark effect mapping of polaron delocalization in chemically doped conjugated polymers. *Chemistry of Materials*, *33*(21), 8489–8500.
5. Akopov, G., Hu, S., Shumilov, K.D., Hamilton, S.G., Pangilinan, L.E., **Mehmedović, Z.,** Yin, H., Robinson, P.J., Roh, I., Kavner, A., Alexandrova, A.N., Tolbert, S.H., Kaner,

R.B. (2024). Hardening in Tungsten Tetraboride with the Addition of Carbon, Zirconium, and Silicon: Intrinsic *vs* Extrinsic Effects. *Chemistry of Materials*, 36(7), 3233-3245.

## Selected Awards and Honors

2024 George Gregory Dissertation Fellowship

2023-2024 Dissertation Year Fellowship

2023 Samantha T. Mensah Award for Diversity, Equity, and Inclusion

2022 Chemistry Departmental Fellowship

2021 Michael E. Jung Excellence in Teaching Award

2018 Competitive Edge Fellowship

2017 Summer Research Fellowship; SFSU

2014-2017 Middle Class Scholarship; SFSU

# Chapter 1

# Introduction to Semiconducting Polymers

## 1.1. Conjugated Polymers

Conjugated polymers (CPs) are a class of organic materials that are characterized by having alternating single- and double- carbon bonds along the polymer backbone. The overlapping p-orbitals along the backbone create a system of delocalized π-electrons, resulting in useful electronic properties.[1] CPs have been studied extensively as alternatives to inorganic semiconductors in many electronic devices, including photovoltaics[2,3], field-effect transistors[4,5], light-emitting diodes[6,7], thermoelectrics[8–10], and others.

The benefit of using CPs in thermoelectric devices instead of inorganic materials such as bismuth telluride ($Bi_2Te_3$) is their facile and low-cost synthesis, solution processability, and mechanical flexibility. In contrast, thermoelectric materials like $Bi_2Te_3$ are synthesized under harsh conditions that include releasing toxic nitrogen oxides or could result in explosions.[11] As such, CPs are better alternatives because their syntheses are much less dangerous.[1]

The major downside of CPs are that they have an intrinsically low electrical conductivity. To combat this, chemical doping methods can be used to increase the conductivity by adding electrical carriers into the polymer matrix either through oxidation or reduction depending on the type of polymer.[1,12–15] In the next section, I discuss the intricacies of chemically doping CPs.

### 1.1.1. Conventional Doping of Conjugated Polymers

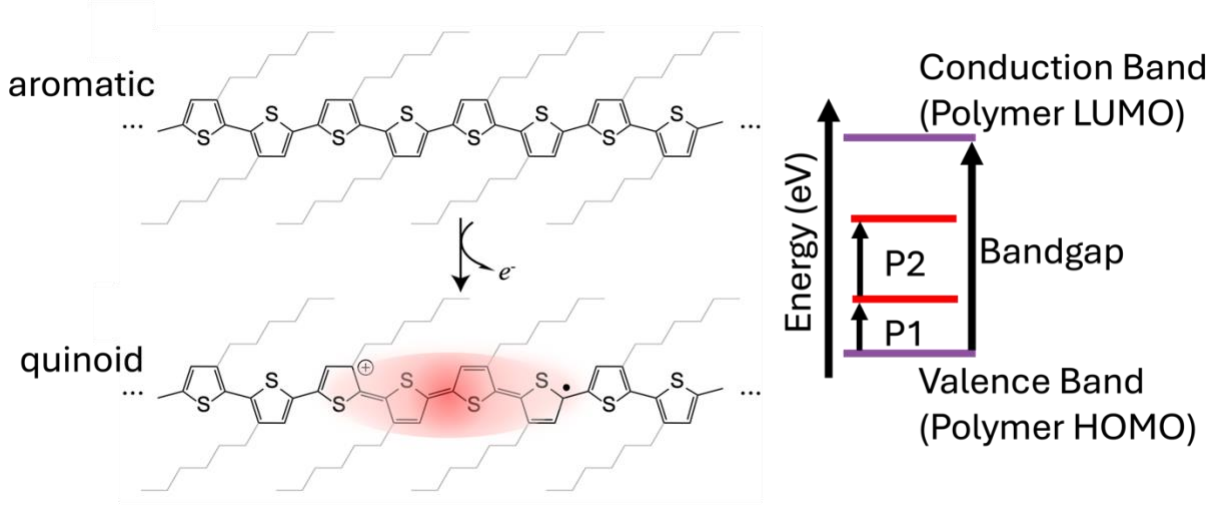


**Figure 1.1 Structural Rearrangement Scheme and an Energy Diagram of Doped CPs**
Figure 1.1 A) Depicts the structural rearrangement P3HT undergoes when a dopant removes an electron from its backbone. The structural change from aromatic to quinoid, the spin, and the positively-charged hole are referred to as a polaron. B) Shows a Jablonski diagram of a generic doped polymer, with each optical transition labeled. When a *p*-type CP is doped, two new intraband states are formed due to the structural change. They lead to optical transitions labeled P1 and P2.

There are three main methods of forming charge carriers in CPs: irradiating the material with light or high-energy radiation[16–18], charge injection from an electrode, referred to as electrochemical doping[15,19–21], and chemical doping.[1,22–24] This thesis focuses on the chemical doping of *p*-type polymers with various molecular oxidants. In a *p*-type CP, chemical doping involves introducing a molecular oxidant that removes electrons from the polymer valence band (VB), creating positively-charged mobile carriers as well as dopant counterions that ensure charge neutrality in the film.[25,26] The positively-charged hole, the unpaired spin, and the lattice rearrangement that is accompanied by its formation, is called a polaron[27,28], a cartoon of which can be seen in **Figure 1.1a**. The formation of polarons on the polymer creates two new intraband states within the polymer bandgap a diagram of which is shown in **Figure 1.1b**.

In order to have structural control over the polymer, sequential processing (SqP) can be used to cast and subsequently dope polymer films. SqP involves first spin casting a polymer film

onto a substrate before spin casting a dopant solution on top with a semi-orthogonal solvent that swells but does not dissolve the underlying polymer.[29,30] This processing method allows for greater control of the film quality and polymer crystallinity, as opposed to blend casting, in which the polymer and dopant are dissolved in the same solution before casting into a film. **Figure 1.2** shows a schematic and photos of the film quality difference between blend-cast films and sequentially-processed films. Blend-casting, as seen in **Figure 1.2**, usually has the doped polymer agglomerate before casting, creating a film that is blotchy and disconnected, rendering structural and electronic measurements quite difficult. In contrast, **Figure 1.2** shows that with SqP the doped polymer is able to uniformly coat the substrate. SqP also allows for greater tunability of the polymer structure by casting the original polymer film from different solvents[30]; this will be discussed in Chapter 2 of this thesis.

**Table 1.1 Various Dopant Redox and Conductivity Values**
Shows how three different dopants, $F_4TCNQ$, DDB-F72, and Magic Blue which all have different redox potentials, result in very different doping levels of P3HT. The higher redox-potential dopants require a lower concentration to achieve a higher film conductivity. In surface doping, the dopant solution is immediately spun off while soak doping allows the dopant solution to sit on top of the film for 80 seconds before being spun off.

| 93% RR P3HT | $F_4TCNQ$<br>Soak dope | DDB-F72<br>Surface dope | Magic Blue<br>Soak dope |
|---|---|---|---|
| [Dopant] (mg/mL) | 6 | 3[31] | 0.25 |
| Dopant Redox value (eV) | -5.2 | -5.7[31] | -5.8[32] |
| Conductivity (S/cm) | 1.6 | 12.8 | 12.1 |

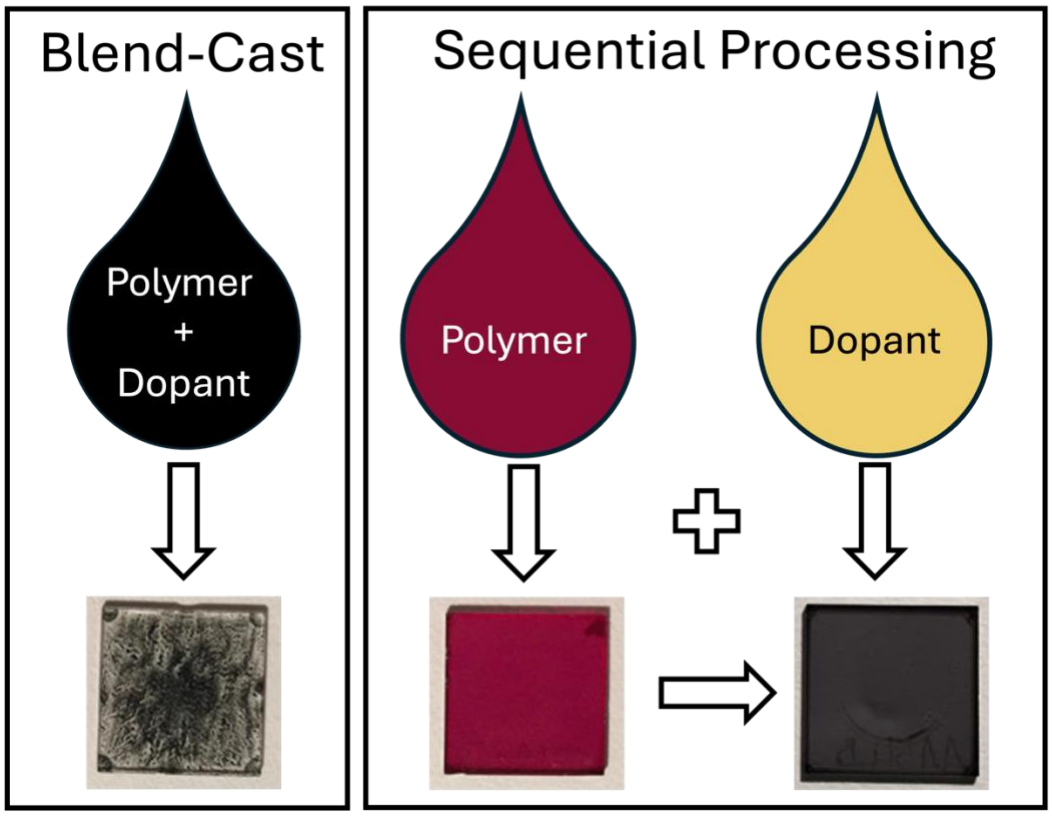


**Figure 1.2 Blend Casting versus Sequential Processing**
Adapted from Ref[30]. The left shows a photograph of a blend-cast film in which the polymer and dopant are cast from the same solution. This method creates uneven, blotchy films that are not uniform. The right shows a schematic for sequential processing (SqP) where first we cast the polymer film and then dope it in a subsequent step. The photograph shows how uniformly coated the polymer is on the substrate, allowing for better quality films. Subsequently, the dopant is introduced from an orthogonal solvent, and the resulting thin films are of much high quality than those made by blend-casting.

Many molecular oxidants have been used to dope *p*-type polymers including, dodecaborane clusters (DDBs)[31,33,34], tris(4-bromophenyl)ammoniumyl hexachloroantimonate (Magic Blue)[32,35], and the most popular dopant, 2,3,5,6-tetrafluoro-tetracyanoquinodimethane ($F_4TCNQ$)[25,30,36–38], structures of which are shown in Figure 1.3. To determine whether an oxidant is capable of doping a polymer, we look at the gap between the polymer's highest occupied molecular orbital ($HOMO_{polymer}$) and the dopant's lowest unoccupied molecular orbital, ($LUMO_{dopant}$). The two states must be positioned such that the $LUMO_{dopant}$ is lower than the $HOMO_{polymer}$, making the electron transfer energetically favorable: the larger the gap, the more favorable the electron transfer

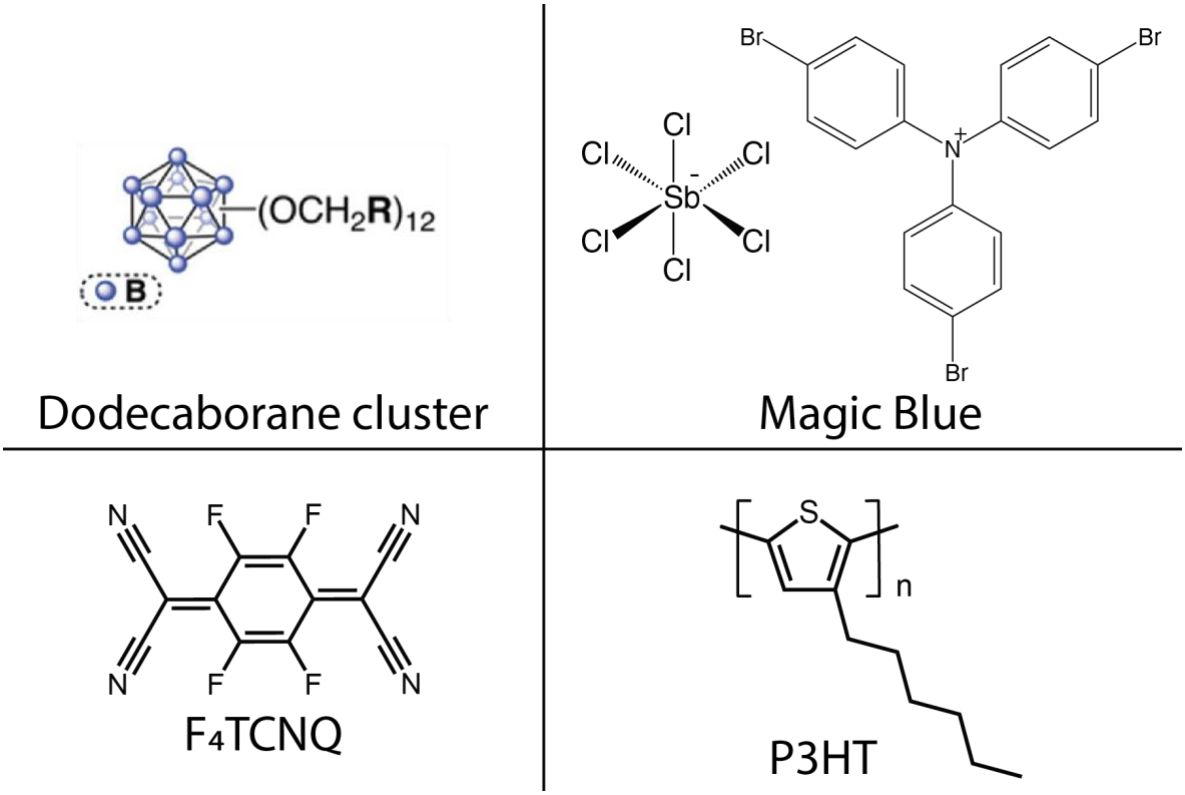


**Figure 1.3 Molecular Structures of Commonly Used Materials**
Figure 1.3 Chemical structures of three molecular oxidants: dodecaborane cluster (DDB), tris(4-bromophenyl)ammoniumyl hexachloroantimonate (Magic Blue), 2,3,5,6-tetrafluoro-tetracyanoquinodimethane ($F_4TCNQ$) and the polymer that will be use the most in this thesis: poly(3-hexylthiophene-2,5-diyl) or P3HT.

and therefore, the higher the doping potential. **Table 1.1** shows electrical conductivity values achieved using the three oxidants mentioned above to dope the work-horse polymer, poly (3-hexythiophene-2,5-diyl) or P3HT, the structure of which also can be found in **Figure 1.3**. The data in **Table 1.1** clearly shows that as the oxidation potential increases from $F_4TCNQ$ to DDB-F72 to Magic Blue, we can use less dopant to achieve the same (or even higher) electrical conductivity.

## 1.1.2 Anion Exchange Doping of Conjugated Polymers

There has been extensive research on conventionally doping CPs with various oxidants.[19,21,26,35,38–51] My thesis focuses on a new SqP doping method called anion-exchange (AX), developed by the Watanabe group in 2019, in which the initiator dopant (typically $F_4TCNQ$)

is introduced along with an inert salt such as lithium bis(trifluoromethane sulfonimide) (LiTFSI).[51] By incorporating the salt at a high concentration, once the $F_4TCNQ$ oxidizes the polymer, the salt anion can exchange with the $F_4TCNQ^-$ counterion by mass action. **Figure 1.4** shows a schematic of this doping process. This process is highly advantageous because it allows for tunability of the counterions within the polymer matrix.[51] Studies have shown that anion-exchange doped films with $TFSI^-$ as the counterion have greater stability, dedoping at a slower rate, than conventionally-doped films with $F_4TCNQ$.[39,43,51,52] Not only does this method allow for tunability and stability of doped CPs, but it has also given rise to incredibly high conductivity values, up to 3,000 S/cm.[32] **Figure 1.5** shows oxidation potentials obtained through cyclic voltammetry (CV) for P3HT, $F_4TCNQ$, and $F_4TCNQ$ with LiTFSI, taken by my colleagues in the Tolbert group at UCLA. The figure shows that with the incorporation of the inert salt, we can increase the oxidation potential range of $F_4TCNQ$ by ~300 meV, which helps explain why there is such a dramatic increase in conductivity upon anion-exchange doping.

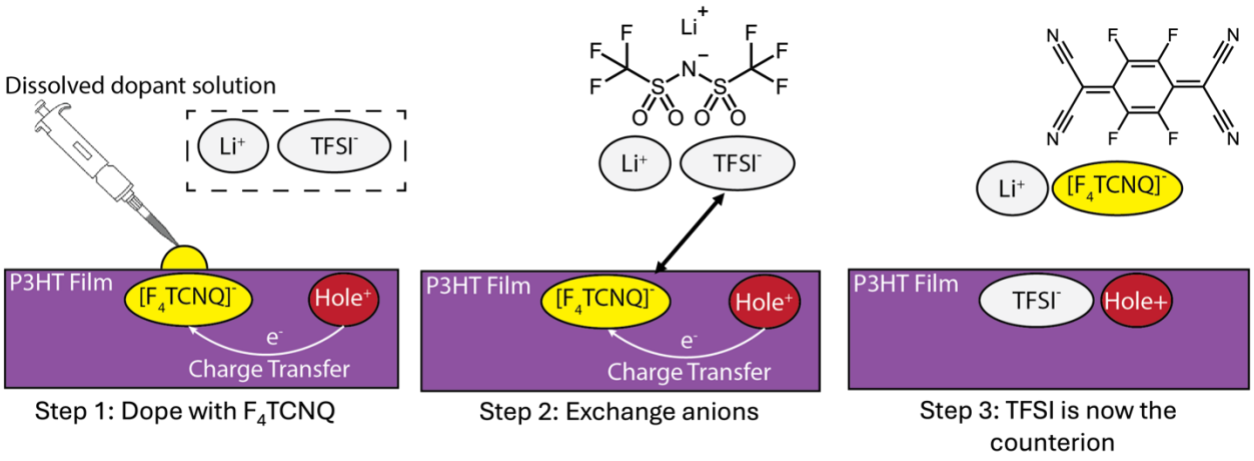


**Figure 1.4 Schematic of Anion-Exchange Doping**
Figure 1.4 Adapted from ref[51]. Shows the schematic of anion-exchange doping. First, the initiator dopant ($F_4TCNQ$) and the inert salt (LiTFSI) are dissolved in the same solution (typically *n*-Butyl acetate, *n*-Ba). After the polymer film has been cast onto a substrate, the dopant and salt solution is cast on top. First the $F_4TCNQ$ oxidizes the polymer, leaving a positively-charged hole on the backbone and an $F_4TCNQ^-$

counterion. Then, by mass action, the anion is exchanged for the $TFSI^-$, leaving it as the new counterion to the polaron in the polymer film.

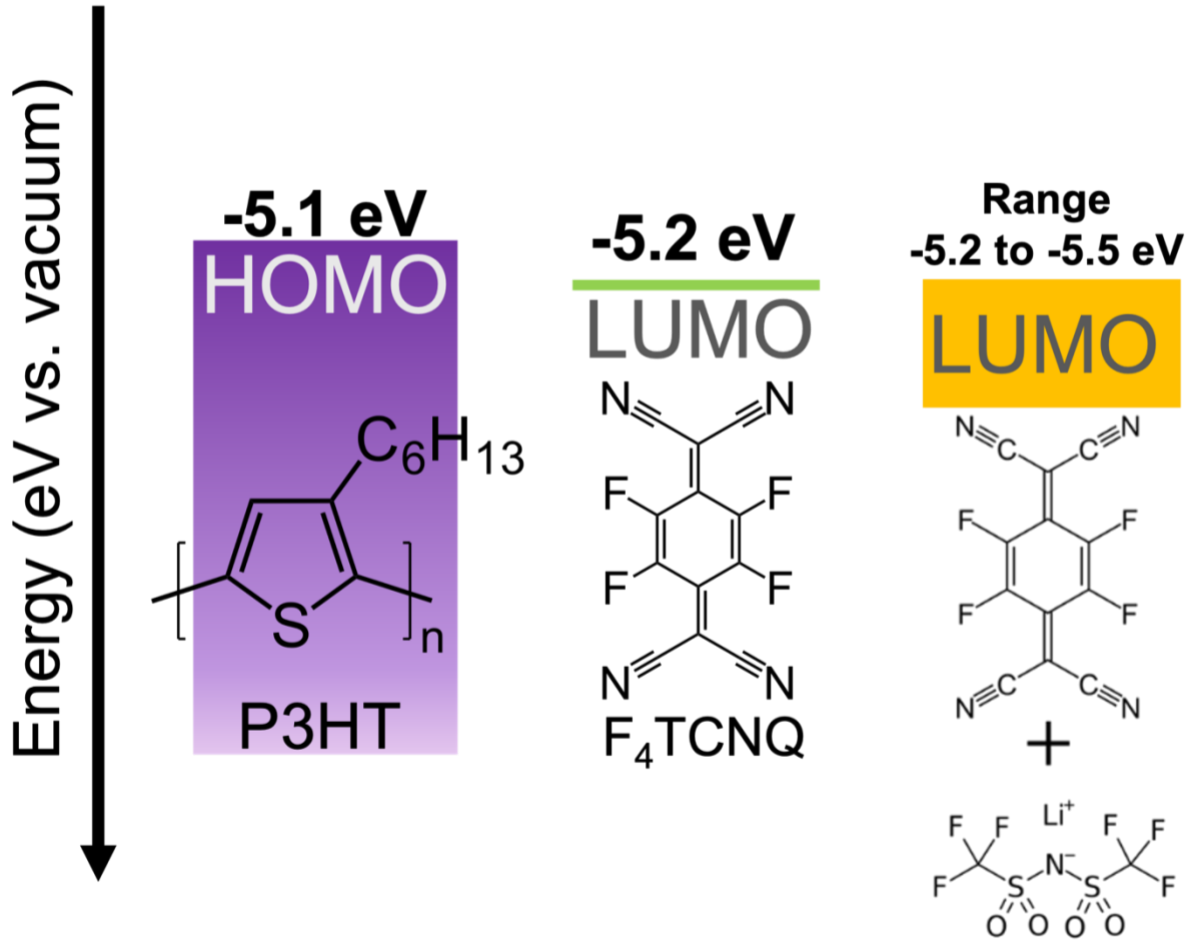


**Figure 1.5 Redox Potentials of P3HT, $F_4TCNQ$, and $F_4TCNQ$ with LiTFSI**
Figure 1.5 Obtained through cyclic voltammetry, the reduction potentials provide an explanation as to why AX doping produces films with higher conductivity. When an inert salt is introduced to the initiator dopant, the redox potential of the dopant effectively increases, creating a larger gap between the $LUMO_{dopant}$ and the $HOMO_{polymer}$, allowing for more energetically favorable electron transfer.

The overarching theme of my thesis focuses on understanding the chemistry of anion-exchange (AX) doping. The following section discusses the various tools I use to analyze the structural and electronic properties of the doped polymer films.

## 1.2 Analysis of Doped Conjugated Polymers

### 1.2.1 Structural Measurements

Through an ongoing collaboration with Prof. Sarah H. Tolbert's group at UCLA, we have been able to conduct studies of the structural dependence of the electronic properties of doped CPs.[2,29–31,34,36,42,53–56] This is mainly done using 2-D Grazing Incidence Wide-Angle X-Ray Scattering (GIWAXS), which for thin films requires a synchrotron light source. GIWAXS probes the crystalline regions of a polymer and is therefore used to understand structural changes to the crystal lattice upon doping.

The polymer that I focus on in this thesis, P3HT, is primarily an edge-on oriented polymer, meaning the side-chains align themselves perpendicular to the substrate. A schematic of the measurement for an edge-on polymer is seen in **Figure 1.6a** with a 2D diffractogram of undoped P3HT shown in **Figure 1.6b**. When a polymer like P3HT is oriented edge-on to the substrate, the information gathered from the out-of-plane direction (along the $q_z$ axis) pertains to the lamellar distance between the sidechains. In the diffractogram, this is denoted as the (100) lattice distance. The in-plane data (along the $q_{xy}$ axis) gives us the $\pi$-stacking distance, denoted as the (020) lattice orientation. Although the 2D diffractograms give quantitative data, they can be visually misleading depending on the color saturation used. Therefore, 1D diffractograms are used by integrating across the grey portions seen in **Figure 1.6b** to obtain easier-to-visualize insight on the structural properties of our films. Structural data obtained from GIWAXS will be discussed heavily in chapters 2 and 4 of this thesis.

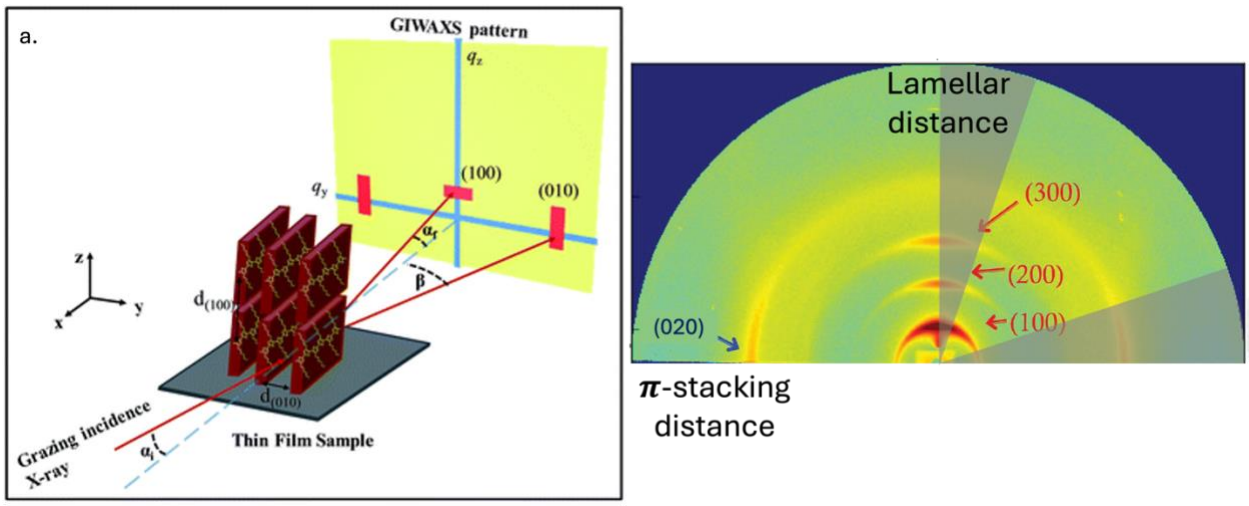


**Figure 1.6 GIWAXS Schematic and 2D Diffractogram of Undoped P3HT**
Figure 1.6 A) Adapted from ref[57], shows the schematic of how GIWAXS is performed for an edge-on oriented polymer like P3HT. B) Shows an example of a 2D diffractogram for undoped P3HT. The shaded regions show the area along which the data is integrated to obtain 1D spectra that give us quantitative values for the (100) distance, also known as the lamellar distance between the polymer stacks along the side-chain distance, and the (020) distance, shown here in the out-of-plane direction, between the π-stacks.

## 1.2.2 Spectroscopy

Absorption spectroscopy is one of the most valuable tools for analyzing doped conjugated polymers as it can confirm if doping has occurred. The black trace in **Figure 1.7** shows the absorption spectrum of undoped P3HT while the purple trace shows the spectrum of lightly-doped P3HT, with each peak labeled by the transition it represents. First, we note that the bandgap transition near 2.5 eV depletes upon doping and shows reduced resolution of vibrational features, which will be discussed in greater detail in chapter 2. The transition from the VB to the first intraband state is called P1, while the transition from the first to the second intraband state is called P2, the energy diagram for which can be found in **Figure 1.1**. These transitions are named "P" for polaron and are numbered in increasing order of their energy. If the P1 and P2 transition peaks appear in an absorption spectrum, that is a clear indication that the polymer is doped. As a polymer is doped further, the P1 peak height increases, and the bandgap continues to bleach. Although there

is potentially a transition from the VB to the second intraband state (called P3), this transition is typically symmetry forbidden. Absorption spectroscopy is used in every chapter in this thesis other than chapter 5.

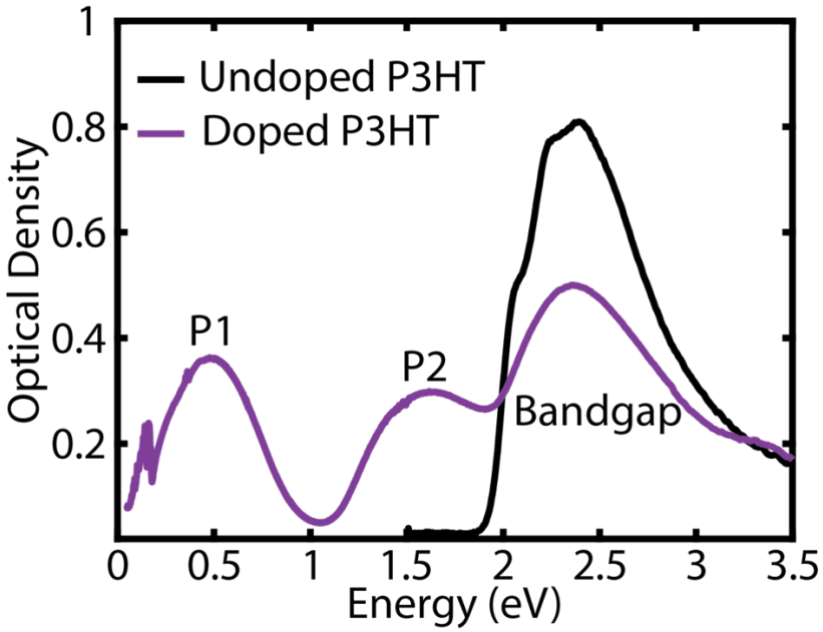


**Figure 1.7 Example Absorption Spectroscopy of Doped P3HT**
Figure 1.7 The black trace shows an undoped P3HT absorption spectrum while the purple trace shows P3HT doped with a low concentration of the powerful oxidant, iron (III) chloride, $FeCl_3$. Before doping, the polymer bandgap strongly absorbs at ~2.5 eV and has vibronic features indicating the crystalline nature of the polymer.[58] Upon the formation of polarons, two intraband states are formed leading to new absorptive transitions. The P1 transition absorbs at ~0.5 eV while the P2 transition absorbs at ~1.5 eV. Although the exact locations of these transitions varies with the polymer and doping conditions, the general trend is that as we dope the polymer, the P1 and P2 transition peaks appear, and the polymer bandgap transition depletes.

## 1.2.3 Electronic Measurements

Although absorption spectroscopy can give us insight into the electronic structure of CPs, it cannot give us direct values for the electrical conductivity. There are multiple methods for measuring the electrical conductivity, which I implement heavily in chapters 2 and 4 of my thesis.

### 1.2.3.1 Conductivity

The electrical conductivity of a doped polymer can be measured through several methods. The most common is four-point probe (4PP), in which four electrical contacts are used to measure the sheet resistance. The advantage of using four contact points instead of two is that it eliminates contact resistance effects that could cause large errors. The contacts can be in a linear geometry (linear 4PP), or they can be in a square geometry (van der Pauw (VdP)). We typically use the VdP geometry as it allows for the average resistivity of the bulk sample to be obtained whereas linear 4PP only provides the resistivity along the sensing direction. **Figure 1.8** shows a schematic of the VdP 4PP geometry and measurement setup. Two separate measurements are taken to obtain the sheet resistance ($R_{\text{sheet}}$) of the bulk film to calculate the resistivity ($\rho$). First, a current is sourced between points 1 and 2, and the resulting induced voltage is measured across points 3 and 4. The electrode geometry (or film) is then rotated by 90º such that the current is sourced now between points 2 and 3 while the induced voltage measured across points 1 and 4. The measurement gives a resistance $R$ for both orientations, which we label as $R_A$ and $R_B$. These values are plugged into equation 1.1 to obtain $R_{sheet}$.

$$\exp\left(-\frac{\pi R_A}{R_{sheet}}\right) + \exp\left(-\frac{\pi R_B}{R_{sheet}}\right) = 1 \qquad \textit{Eq. 1.1}$$

$R_{sheet}$ has units of ohms per square ($\Omega/\square$); thus, to obtain the resistivity, $\rho$, of the sample, the thickness, $d$, of the film must be measured. Film thicknesses in this thesis were all obtained using a Veeco Dektak 150 Surface Profilometer. Once both $R_{sheet}$ and $d$ are known, equation 1.2 yields $\rho$. The conductivity $\sigma$ is simply the inverse of $\rho$.

$$R_{sheet} = \frac{\rho}{d} \qquad \textit{Eq. 1.2}$$

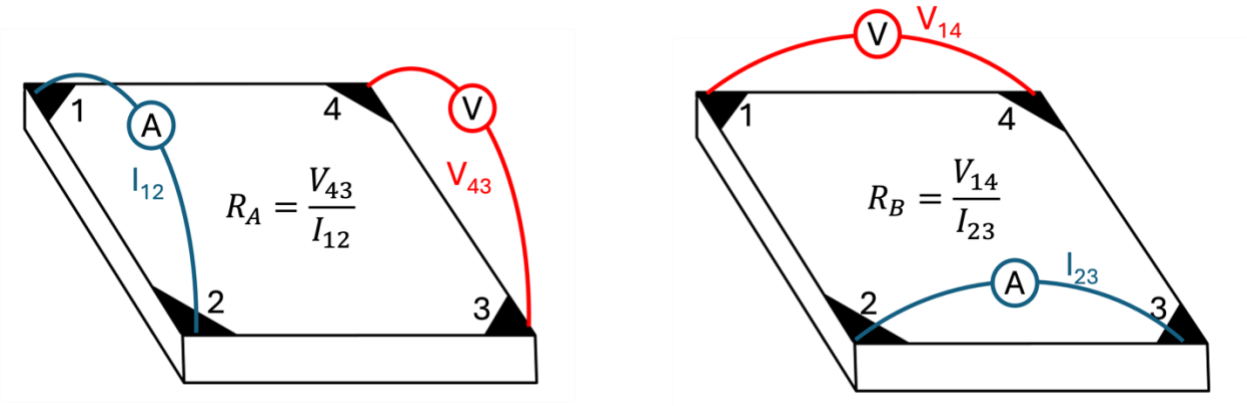


**Figure 1.8 Schematic of 4-Point-Probe Conductivity Measurement**
Figure 1.8 A general schematic of how a four-point-probe (4PP) measurement works using the van der Pauw (VdP) geometry. The first measurement applies a current between contacts 1 and 2 while measuring the induced voltage across contacts 3 and 4. The second measurement is taken by turning the contacts by 90º so that the current is applied between contact points 2 and 3 while the voltage is measured across contacts 1 and 4. The resistance obtained for each measurement gives the sheet resistance via Eq. 1.1, and with the sample thickness, Eq. 1.2, the conductivity of the doped polymer film.

### 1.2.3.2 Mobility and Carrier Density

The ultimate goal of doping CPs is to obtain a high figure of merit for application in thermoelectric devices.[9–11,24,59] Equation 1.3 defines the figure of merit, $ZT$:

$$ZT = \frac{S^2 \sigma T}{\kappa} \qquad \textit{Eq. 1.3}$$

where $S$ is the Seebeck coefficient and $\kappa$ is the thermal conductivity. To maximize $ZT$, a high $\sigma$ is desirable. In order to maximize the conductivity, we need to understand its individual components as highlighted in equation 1.4:

$$\sigma = ne\mu \qquad \textit{Eq. 1.4}$$

The individual components of $\sigma$ are the carrier density ($n$), the number of charge carriers per unit volume, and the carrier mobility ($\mu$), which measures how quickly the positively-charged hole can migrate throughout the *p*-type polymer matrix under the presence of an applied electric field. It has proved difficult to separate $n$ and $\mu$ experimentally. During my graduate research, we

purchased a M91 FastHall instrument from LakeShore Cryotronics because of its ability to use the Hall effect to measure the carrier density and conductivity, thereby determining the carrier mobility from Eq. 1.4.

A fundamental schematic of the Hall effect measurement can be seen in **Figure 1.9**. When a current is applied in the *x*-direction and a magnetic field is applied perpendicular to that, along the *z*-direction, it forces the charge carriers to migrate to opposing ends of the film, creating a measurable voltage along the *y*-axis, called the Hall voltage, labeled as $V_H$ in **Figure 1.9**. At a constant applied current and magnetic field, measuring $V_H$ provides a way to determine the $n$ using equation 1.5:

$$n = \frac{IB}{V_H e d} \qquad \textit{Eq. 1.5}$$

where $I$ is the applied current (typically 10 $\mu A$), $B$ is the magnetic field (1.0236 T for our instrument), $e$ is the electronic charge, and $d$ is the thickness of the film. The instrument measures the electrical conductivity using the same VdP 4PP method discussed previously and calculates the $\mu$ using equation 1.4. In chapter 2, we will explore the structural and counterion dependence of $n$ and $\mu$ upon anion-exchange doping.

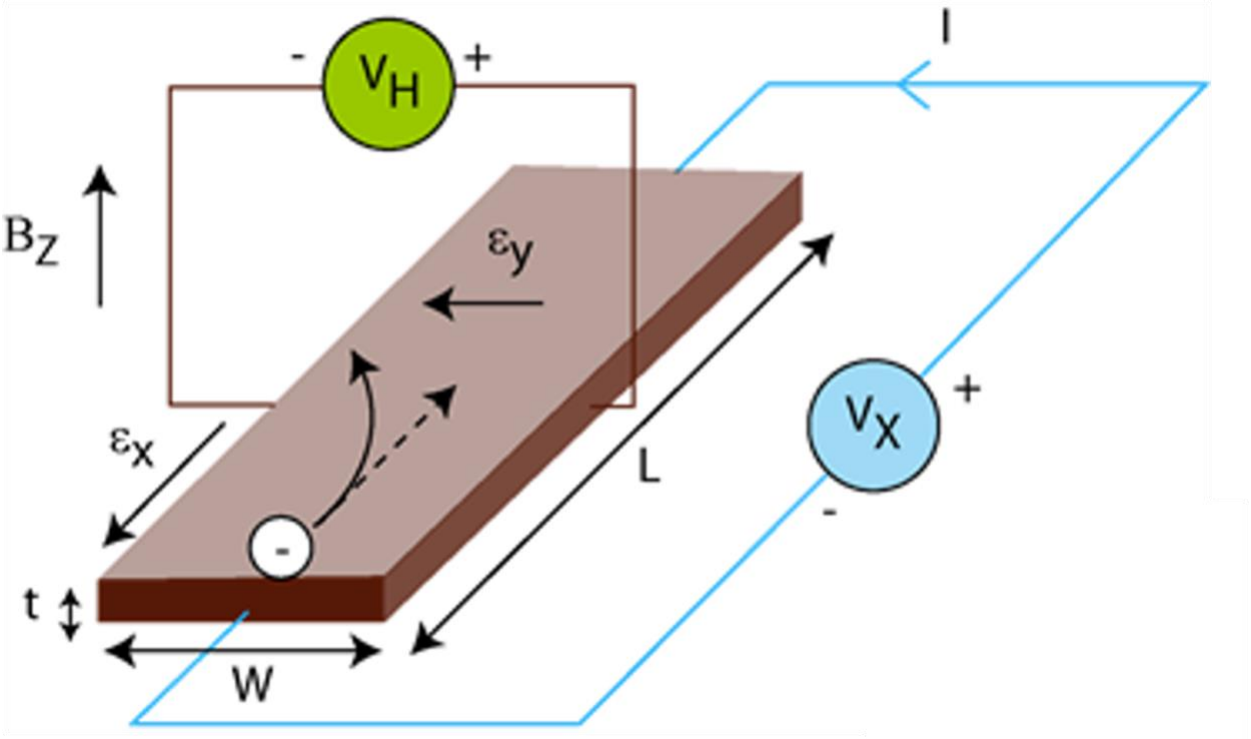


**Figure 1.9 A Schematic of the Hall Effect Measurement**
Figure 1.9 Adapted from ref[60]. A schematic of the Hall effect experiment to obtain the carrier density of a doped conjugated polymer film. First, a constant current is applied along the x-direction while a constant magnetic field is applied along the *z*-axis. This causes a force on the charge carriers, creating an induced voltage across the *y*-axis. This voltage, labeled $V_H$, is related to the carrier density of the doped film.

## 1.3 Overview of Thesis

This thesis is comprised of five chapters: chapters 2, 3, and 4 focus on my work on doped conjugated polymers in Dr. Benjamin J. Schwartz's lab. Chapter 5 focuses on my previous theoretical work from the Dr. Anastassia Alexandrova's lab.

### 1.3.1 Chapter 2: Understanding the Role of Crystallinity and Electronic Properties of Poly(3-hexylthiophene-2,5-diyl) upon Anion-Exchange Doping

The work in this chapter is currently unpublished but will be submitted soon. The biggest challenge in integrating conjugated polymers (CPs) into thermoelectric and other devices is their

limited electrical conductivity. Recent efforts have focused on enhancing the performance of CPs by using another molecule to dope the polymer and create charge carriers. The sequential processing (SqP) method developed by our group, works by casting the polymer and dopants from orthogonal solvents.[29] By separating the polymer and doping casting steps, it allows for greater control over the polymer crystallinity by changing the regioregularity or polymer processing conditions. Using SqP, we can study the effects of tuning the polymer crystallinity with anion-exchange doping (AXD), in which a high concentration of inert salt anion accompanies the introduction of the dopant.[51] Here, we will explore how introducing a molecular oxidant with and without an inert salt affects the conductivity of polymers with different crystallinities and two doping concentrations.

Combining absorption spectroscopy, Grazing Incidence Wide-Angle X-Ray Scattering, and Hall effect measurements, we have determined how the carrier mobility and carrier density vary with the polymer crystal structure and doping level. We show that a mobility-dominated conductivity increase is seen upon anion-exchange doping across all polymer crystallinities compared to conventional doping in the low-initiator-dopant-concentration regime. Meanwhile, a more structurally-dependent trend is seen when comparing the two doping methods in the high-initiator-dopant-concentration regime: when the initial polymer crystallinity is high, the conductivity increase is mobility-dominated, while a carrier-density-dominated conductivity increase is seen when the initial polymer structure is more amorphous.

### 1.3.2 Chapter 3: Formation of Li-$F_4$TCNQ Complex During High Concentration Anion-Exchange Doping of Semiconducting Polymers

The work in this chapter is currently unpublished but will be submitted soon. Anion-exchange doping has become a popular method to introduce polarons into *p*-type conjugated polymers to increase their intrinsically low conductivity.[39,43,47,51,52] Although many different initiator dopants are used, a common dopant-salt combination for anion-exchange doping is 2,3,5,6-tetrafluoro-tetracyanoquinodimethane ($F_4TCNQ$) and lithium bis(trifluoromethane) sulfonimide (LiTFSI). Depending on the concentration of initiator dopant, it is usually presumed that all the $F_4TCNQ^-$ ions are exchanged out by mass action for the salt anion, $TFSI^-$. When both LiTFSI and $F_4TCNQ$ are in excess however, we find that two new peaks appear that are not associated with the different initiator dopants and are not seen when conventionally doping without the addition of salt. Using a variety of experimental and theoretical techniques, we explored the formation conditions and electronic properties of the species responsible for these peaks. Resonance Raman and quantum chemistry calculations led us to assign these peaks to a Li-$F_4TCNQ$ complex that forms during the exchange process of anion-exchange doping.

### 1.3.3 Chapter 4: Unfinished Business: The Nuances of Magic Blue Doping

The work in this chapter is currently unpublished and will be submitted at a later date as the work is still undergoing. During my time in the Schwartz group, I worked on a few projects that were not my main focus but in which I was able to make a sizeable contribution; one of these will be discussed in this chapter.

There has been debate in the literature as to where the magic blue counterion resides once reduced by the polymer following doping. Although one study has claimed that the dopant infiltrates the amorphous regions as evidenced by a lack of structural change in X-Ray diffraction,[32] we ran GIWAXS experiments on P3HT doped with magic blue and showed that

indeed the crystal structure has not just one, but two different structural changes depending on the dopant concentration. We propose that the magic blue counterion is a special dopant that first oxidizes the amorphous regions in the polymer, and then the crystalline regions. This is evidenced by no structural changes in the low doping regime where absorption data show that doping is indeed taking place, indicating that the counterion is infiltrating the amorphous regions. After a certain doping concentration, GIWAXS shows a large structural change indicating the counterions are now intercalating into the crystalline sites. Once the doping concentration is high enough, we see the formation of bipolarons in the absorption spectrum that coincides with another structural change in the GIWAXS. This portion of chapter 4 dives into greater detail about the doping mechanism of magic blue.

### 1.3.4 Chapter 5: Theoretical Studies on the Hardening Effects of Doped $WB_4$

The work in this chapter was previously published in reference [61]. This work was performed while I was working with Dr. Anastassia N. Alexandrova as a theorist. Here, we focused on understanding the bonding of inorganic materials that are categorized as being 'superhard'. The inorganic materials discussed in this chapter are also doped; not molecularly as with organic CPs, but instead by crystal embedding. In this publication, my role was to run the calculations that were integral to understanding the doping process as well as to determine whether the hardening effects associated with doping are due to intrinsic or extrinsic effects.

Alloys of tungsten tetraboride ($WB_4$) with the addition of C and Si were prepared by arc-melting of the constituent elements. The phase purity was established by powder X-ray diffraction (PXRD) and surface morphology by scanning electron microscopy (SEM) analysis. Vickers hardness measurements showed hardness enhancement for alloys with a nominal composition of

($W_{0.98}Si_{0.02}$):11.6B and ($W_{0.95}C_{0.05}$):11.6B of 52.2 $\pm$ 2.5 GPa, respectively, compared to 41.2 $\pm$ 1.4 GPa for pure $WB_4$. ($W_{0.92}Zr_{0.08}$)11.6B was determined in previous work to have a hardness of 55.9 $\pm$ 2.8 GPa. Bulk moduli were calculated following analysis of high-pressure diffraction data and were determined to be 329 $\pm$ 4 (*K0'* = 2) and 390 $\pm$ 9 (*K0'* = 0.6) GPa for 8 atom % Zr and 5 atom % C-doping, respectively, compared to 326-339 GPa for pure $WB_4$. Computational analysis was used to determine the dopant positions in the crystal structure, and it was found that Zr primarily substitutes W in the 2c, Si substitutes for the entire B3 trimers, and C inserts in the $B_{hex}$-layer. The hardness enhancement in the case of Zr-doping is attributed primarily to extrinsic hardness effects (nanograin morphology), in the case of C—to intrinsic effects (interlayer bond strengthening), and in the intermediate case of Si—to both intrinsic and extrinsic effects (bond strengthening and fine surface morphology).

# Chapter 2

# Understanding the Role of Crystallinity and Electronic Properties of Poly(3-hexylthiophene-2,5-diyl) upon Anion-Exchange Doping

## 2.1 Introduction

Conjugated polymers offer great promise for use in solar cells, thermoelectrics, and other device applications, due to their solution processability and mechanical flexibility.[6,7,62–72] Although their electronic conductivity is typically lower than their inorganic counterparts, the conductivity of semiconducting polymers can be greatly enhanced by creating charge carriers via chemical doping.[14,41,50] For *p*-type conjugated polymers, chemical doping involves introducing a molecular oxidant to remove electrons from the HOMO or valence band (VB), creating positively-charged mobile carriers that contribute to the increase in electronic conductivity.[41,73–76] The positively-charged hole, its spin, and the lattice rearrangement that is accompanied by its formation, are together referred to as a polaron.[27,28] Doping conjugated polymers in this fashion leads to high conductivities due to an increase in both carrier density and carrier mobility.

The way in which doping affects the electrical properties of semiconducting polymers is dependent on their crystallinity.[2,36,77–79] One of the most well-studied semicrystalline *p*-type polymers is poly(3-hexylthiophene-2,5-diyl) (P3HT). Its degree of crystallinity can be controlled synthetically, by tuning the regioregularity, or through the choice of processing conditions, particularly if the doped films are created using the sequential processing (SqP) technique.[29,40,80,81]

SqP entails casting the polymer film first, followed by the introduction of the dopant in a second casting step from a semi-orthogonal solvent that swells but does not dissolve the polymer. In general, the VB of an ordered polymer, such as regioregular (RR) P3HT (**Figure 2.1a**) is higher in energy than a disordered polymer, such as regiorandom (RRa) P3HT (**Figure 2.1b**). This makes RRa P3HT more difficult to dope because there is less of an energetic driving force to transfer an electron from the polymer's VB to the LUMO or conduction band (CB) of a dopant.[82]

The effectiveness of the doping process is also dependent on the oxidizing strength and concentration of the selected dopant. Chemical doping of semicrystalline polymers like P3HT with molecular oxidants such as 2,3,5,6-tetrafluoro-7,7,8,8-tetracyanoquinodimethane ($F_4TCNQ$; **Figure 2.1c**) leaves a dopant counterion, to ensure charge neutrality, in the film; [25,30,36] this counterion can interact coulombically with the polaron.[25,30,36] In general, deep-trap states are doped first, which do not produce mobile charge carriers that contribute to the electrical conductivity. Once the deep traps are filled, crystalline sites are doped next as these have a more favorable energy for polaron formation, as discussed above.[83] Only at very high dopant concentrations or when using very strong oxidizing agents do the amorphous, disordered regions of the polymer start to dope. For example, strongly oxidizing dopants such as dodecaborane clusters,[33,84] magic blue,[44] and iron (III) chloride ($FeCl_3$)[8,54] all have been shown to dope both the crystalline and amorphous regions of polymers like P3HT. Therefore, the crystal structure of the polymer and the concentration and oxidizing power of the dopants all contribute to the effectiveness of the doping process.

Recently, a new doping method called 'anion-exchange' (AX) has been introduced, which allows dopants with only modest oxidizing power to dope disordered sites in conjugated polymer films.[43,51] In AX doping, a polymer film is exposed to a dopant solution containing both the initial

oxidant and a high concentration of inert salt. Once the oxidant dopes the polymer, its counterion is then exchanged for the salt anion by mass action. This method not only allows for tunability and control over the choice of counterion, but also provides enhanced electrical conductivity and greater doped film stability.[51] We note that some of the most common electrolyte counterions used with this method, such as bis(trifluoromethane) ($TFSI^-$) and hexafluorophosphate ($PF_6^-$) are hygroscopic, which can significantly lower the conductivity in the presence of ambient humidity.[52]

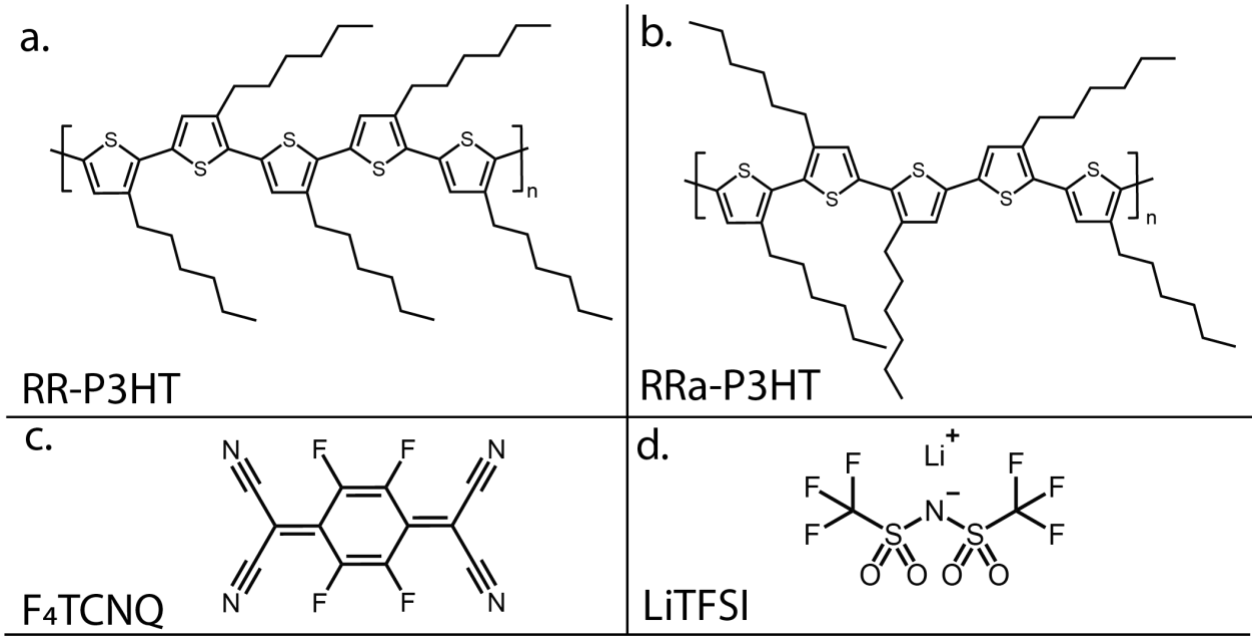


**Figure 2.1 Molecular Structures of RR and RRa P3HT, $F_4TCNQ$ and LiTFSI**

Although many groups have applied the AX method to dope a wide range of conjugated polymers,[39,43,51,52] a detailed understanding of how this new doping mechanism interacts with the polymer morphology to determine the resulting electrical properties is still needed. In this work, we use a variety of polymer regioregularities and processing solvents to prepare P3HT films with five different degrees of crystallinity. For all five polymer morphologies, we study the electrical properties using both conventional chemical doping with $F_4TCNQ$ and AX doping with $F_4TCNQ$ and lithium $TFSI^-$, **Figure 2.1d**). We dope the polymers using a low concentration of $F_4TCNQ$,

which we refer to as initiator-limited, where the total extent of doping is limited by the amount of $F_4$TCNQ. We also use a high concentration of $F_4$TCNQ such that the extent of doping is not limited by the amount of available dopant. The combination of five crystallinities, two doping methods, and two doping concentrations provides multiple axes of comparison that allow us to investigate the relationship between the structural and electronic properties of conjugated polymers and the anion-exchange doping process.

Here, we take advantage of Hall effect measurements to extract carrier densities and mobilities to correlate the electronic properties of AX-doped films with their initial degree of crystallinity. We find that when doping is initiator-limited, AX increases conductivity relative to conventional doping primarily by increasing the carrier mobility, regardless of the initial polymer crystallinity. At high dopant concentrations, however, we observe the way AX improves film conductivity relative to conventional doping depends on the polymer morphology. In highly crystalline polymer films, the increased conductivity seen upon high-concentration AX doping is dominated by a higher carrier mobility, whereas in more amorphous polymer films, higher carrier densities are what causes AX to have improved conductivity. The insights gained from this investigation can be used to predict how the carrier mobility and carrier density will be affected by polymer morphology upon introducing an inert salt with a relatively successful molecular oxidant.

## 2.2 Methods

We began our study by producing P3HT films with five different degrees of crystallinity using two methods. First, we used four commercially available P3HT polymers with different regioregularities: 99% regioregular (RR) (Tokyo Chemical Industry), 97% RR (Osilla), 90-95% (referred to hereafter as 93%) RR (Reike Metals), and Regiorandom (RRa) (Reike Metals). Spin-

coating each of the regioregular materials from a 2% w/v solution in 1,2-dichlorobenzene (ODCB) leads to films with three distinct degrees of crystallinity. In addition, we controlled the degree of crystallinity of the 93% RR P3HT material by casting films from two different processing solvents: 2% w/v in ODCB and 1% w/v in chloroform (CF). Because CF is a high vapor pressure solvent that evaporates quickly, the P3HT polymer chains have less time to crystallize than when films are cast from a low vapor pressure solvent like ODCB.[30,79] Finally, RRa P3HT was cast from a 1% w/v in CF to enhance the amorphous character of the polymer. In combination, this gives us P3HT films with five distinct structures: 99% RR P3HT in ODCB, 97% RR P3HT in ODCB, 93% RR P3HT in ODCB, 93% RR P3HT in CF, and RRa P3HT in CF.

To dope the P3HT films with different degrees of crystallinity, we used SqP.[30] Because swelling primarily affects the amorphous and not the crystalline regions of a polymer film, this method largely preserves the degree of crystallinity of a conjugated polymer film through the doping process.[30] We used SqP to conventionally dope our P3HT films of varying crystallinity with $F_4TCNQ$ dissolved in *n*-butyl acetate (*n*-BA) at two concentrations: ~3.5 mM (1 mg $mL^{-1}$), for the initiator-limited studies, and ~20 mM (6 mg $mL^{-1}$), for the high-concentration doping studies. To dope the different P3HT films via AX, we used solutions with the same two concentrations of $F_4TCNQ$ that also contained ~100 mM (30 mg $mL^{-1}$) of LiTFSI.

To prepare doped P3HT films using these solutions, we first cast polymer films onto 1.3 × 1.3 cm square glass substrates using either 20 μL (for ODCB cast polymers) or 35 μL (for CF cast polymers) of solution spun at 1,000 RPM for 1 minute followed by spinning at 4,000 RPM for 5 seconds. Once the pristine polymer films were dry, we used 100 μL of dopant (or dopant plus salt) solution to cover the polymer, allowing that solution to sit for 80 seconds before spinning it off at 4,000 RPM for 10 seconds.

Grazing incidence wide-angle X-ray scattering (GIWAXS), optical spectroscopy, and Hall effect measurements were used to analyze the structural and electronic properties of our pristine and sequentially-doped polymer films. GIWAXS was performed to monitor how P3HT regioregularity and processing conditions affect crystallinity, as well as to determine changes in the polymer crystal structure upon doping via the two different methods. These experiments were done at the Stanford Synchrotron Radiation Light source (SSRL) at beamline 11-3; details can be found in the Supporting Information (SI).

Hall effect measurements were run using a LakeShore M91 FastHall instrument, providing access to four-point-probe electrical conductivity, mobile carrier density, and carrier mobility. It is notoriously difficult to measure carrier mobilities in low-mobility materials, because carriers that move by hopping can screen the field and thus reduce the measured Hall voltage, resulting in an overestimation of the carrier density and an underestimation of the carrier mobility.[4,60,85] As a result, we were not able to obtain reliable Hall carrier densities or mobilities for our doped films composed of 99% RR or RRa P3HT because these samples pushed the limits of our instrument.

Given this limitation, to determine the carrier mobility and density in our 99% RR and RRa samples, we took advantage of the fact that the magnitude of the polaron absorption spectrum is proportional to the carrier density. As discussed in the SI, we made a correlation curve of the oscillator-strength integrated area of the polaron absorption against carrier density for the sample combinations where we were able to make reliable Hall measurements. We then used this correlation curve to estimate the carrier density in the samples for which Hall measurements were not possible. By estimating the carrier density, $n$, in this way, we then determined the carrier mobilities, $\mu$, from the measured electrical conductivities, $\sigma$, via $\sigma = nq\mu$, where $q$ is the fundamental charge. Together, the combination of our Hall and optical spectroscopy

measurements provide the tools needed for in-depth electronic property analysis of AX doping across a variety of different crystalline environments.

## 2.3 Results and Discussion

### 2.3.1 Characterization of Pristine P3HT Films of Varying Crystallinity using X-Ray Scattering and Optical Spectroscopy

We have previously found that modifying the regioregularity of P3HT prior to conventional doping with $F_4TCNQ$ enhanced the conductivity by increasing the carrier mobility.[79] This mobility increase was attributed to a greater polaron delocalization in more highly-ordered P3HT samples.[79] Here, we study the effects of crystallinity on AX doping to determine whether the AX method behaves in a similar fashion as conventional doping as a function of polymer morphology. As mentioned above, we explore AX doping using P3HT samples with five different degrees of crystallinity, which in order from most to least crystalline are: 99% regioregular (RR) P3HT cast from ODCB (red curves in the figures below), 97% RR P3HT cast from ODCB (orange curves), 93% RR P3HT cast from ODCB (yellow curves), 93% RR P3HT cast from CF (green curves), and regiorandom (RRa) P3HT cast from CF (blue curves).

Radially-integrated GIWAXS diffractograms for P3HT films with each of the five different degrees of crystallinity prior to doping are shown in **Figure 2.2a**. The (*h*00) peaks correspond to the distance between the backbones along the side-chain, or lamellar, direction, which for P3HT occur at multiples of $q$ = 0.40 $Å^{-1}$, corresponding to distance of 15.9 Å.[30,36] The presence of overtones, (200) and (300) peaks, in the higher-crystallinity films is indicative of more highly-ordered material.

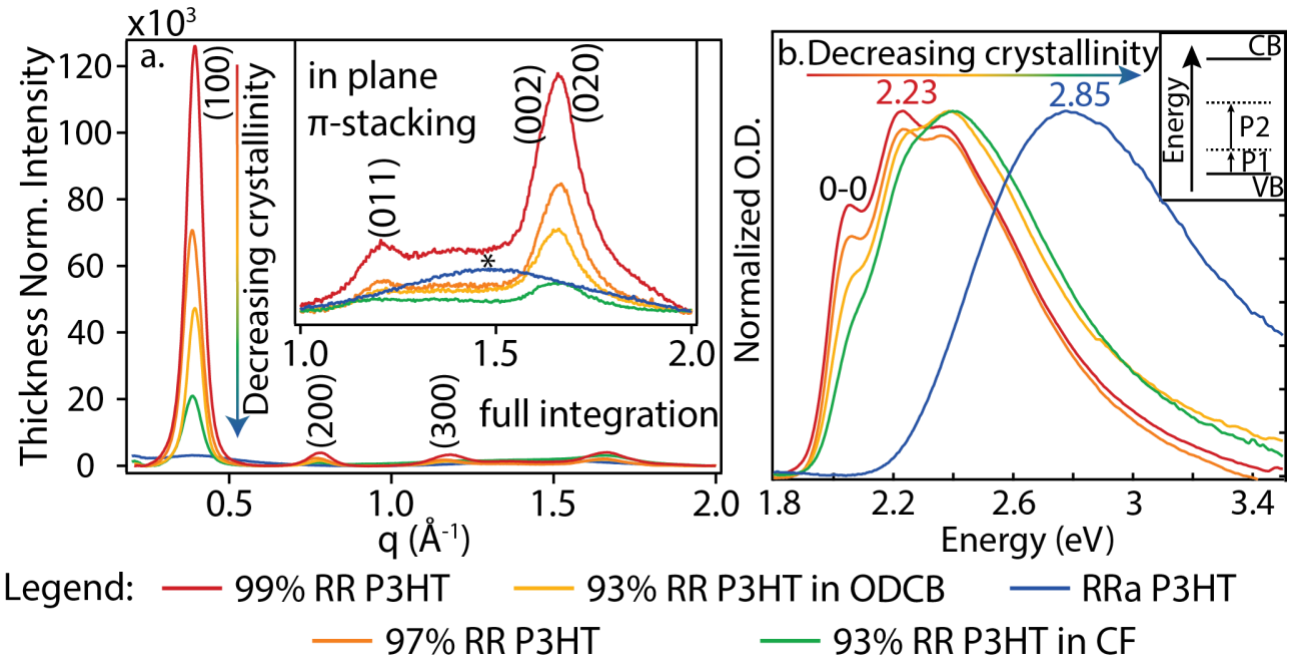


**Figure 2.2 Structural and Optical Spectra of Undoped P3HT with Varying Crystallinity**
Figure 2.2 a) Radially-integrated and thickness-normalized GIWAXS diffractograms of undoped P3HT films with different degrees of crystallinity. The (100) and (020) peaks decrease in intensity and broaden as crystallinity decreases, while the disordered π scattering peak (highlighted by an *) increases in the least-crystalline samples. b) Normalized UV-Visible absorption spectra of the same undoped P3HT films with different degrees of crystallinity. As the crystallinity decreases, the vibronic features decrease and the band-gap transition blue shifts. The inset in b) shows an energy level diagram highlighting the two intraband transitions (dotted) seen upon doping. Excitation from the VB to the lower mid-gap state is known as the P1 transition, and excitation from the first transition to the second mid-gap state is known as the P2 transition. The regioregularities associated with each color is shown in the legend underneath.

**Figure 2.2a** shows that films of undoped 99% RR P3HT have the highest-area (100) lamellar peak, followed by a progression (200) and (300) overtones. As the P3HT regioregularity decreases to 97% and then 93%, the scattering intensity for all the polymer diffraction peaks decrease, signifying a loss of crystallinity. For RRa P3HT films, the scattering has a complete absence of lamellar overtones and a very weak fundamental (100) peak, indicating the almost entirely amorphous character of this material.

The scattering from conjugated polymers also shows an (020) peak near 1.7 $Å^{-1}$, which corresponds to the distance between the polymer backbones in the $\pi$-stacking direction.[55] The inset

in **Figure 2.2a** shows this $\pi$-stacking peak, which decreases in intensity with the degree of polymer crystallinity in the same order as the (100) peaks. The in-plane scattering shown in the inset also shows a disordered $\pi$-stacking peak (highlighted with an asterisk), which is associated with amorphous material. Because RRa P3HT is primarily amorphous, the disordered $\pi$-stacking peak is most pronounced in this sample. Overall, the GIWAXS data in **Figure 2.2a** verifies that we are able to controllably produce P3HT samples with five distinct different degrees of crystallinity.

**Figure 2.2b** shows the UV-Visible absorption spectra of the same films whose X-ray scattering is shown in **Figure 2.2a**. The data show that the main absorption feature, which corresponds to the bandgap transition of P3HT (VB to CB see inset), undergoes a 0.6 eV blue-shift from the most to the least crystalline sample. A blue-shifted bandgap is associated with smaller conjugation lengths, as would be expected from a decrease in polymer order.[86,87] The data also show that the vibronic features accompanying this transition, particularly the height of the 0-0 band, disappear as the polymer crystallinity decreases. This phenomenon is well documented in the literature and has been explained theoretically by Spano and co-workers.[86,87] Thus, absorption spectroscopy also provides a strong indication that our five P3HT samples have significantly different degrees of crystallinity.

### 2.3.2 Characterization of Doped P3HT Films using Optical Spectroscopy and X-Ray Scattering

Now that we have established that we can produce P3HT films with five different degrees of crystallinity, we turn next to exploring the spectroscopic and structural changes that take place upon both conventional and AX doping of these films. **Figure 2.3a** shows the UV-Vis-IR absorption spectrum of 99% RR P3HT pristine (black trace), and 99% RR P3HT both

conventionally-doped with ~20 mM $F_4TCNQ$ in *n*-BA (red dashed trace) and AX-doped with ~20 mM $F_4TCNQ$ and ~100 mM LiTFSI in *n*-BA (red solid trace). Doping is confirmed in both cases by the appearance of the two polaron absorption peaks labeled P1 (~0.4 eV) and P2 (~1.6 eV) (cf. inset of **Fig. 2.2b**) as well as a depletion of the bandgap absorption (~2.4 eV).

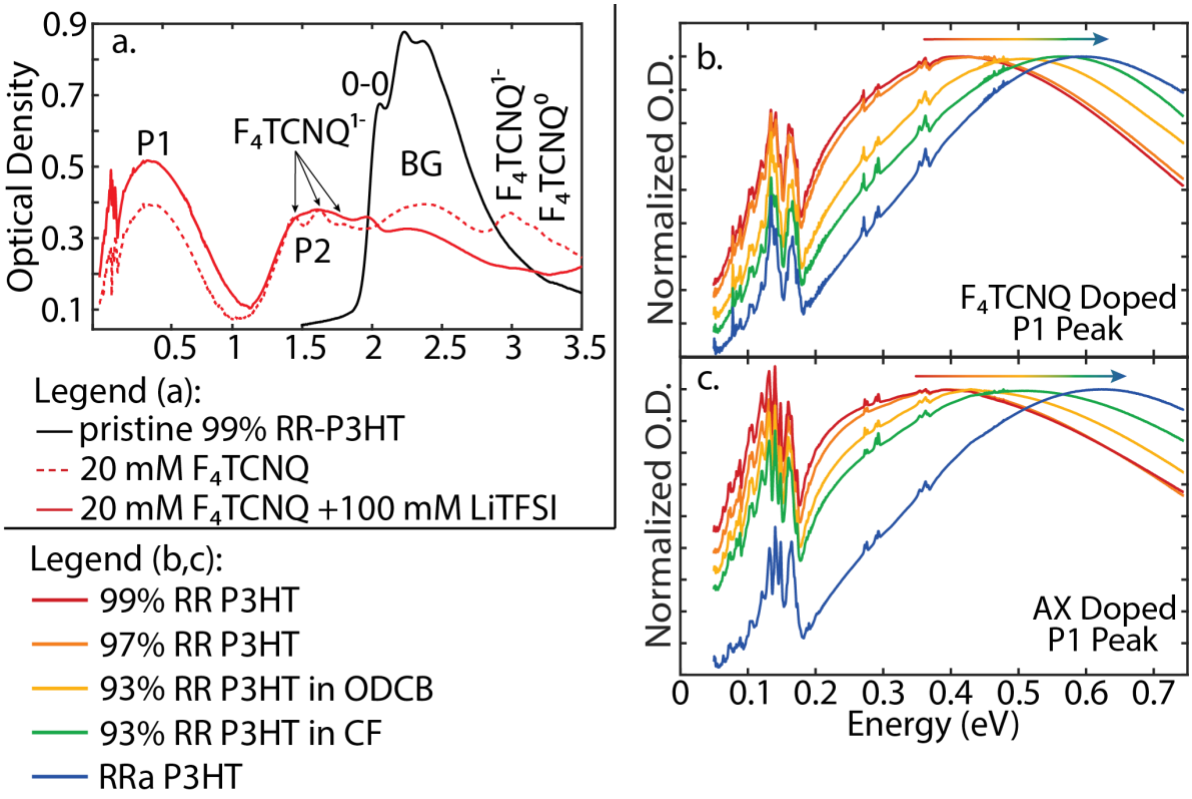


**Figure 2.3 UV-Vis-IR Spectroscopy of High-Concentration Conventional and AX Doped P3HT**
**Figure 2.3**. a) UV-Vis-IR spectroscopy of pristine 99% RR-P3HT (black curve), conventionally-doped with ~20 mM $F_4TCNQ$ in *n*-BA (red dashed curve), and AX-doped with ~20 mM $F_4TCNQ$ and ~100 mM LiTFSI in *n*-BA (red solid curve). Similar plots for the other four polymers can be found in the SI. The neutral polymer bandgap absorption is labeled BG, and the polaron absorption peaks are labelled P1 and P2. The four $F_4TCNQ^-$ absorption peaks and the absorption of neutral $F_4TCNQ^0$ is also labelled. Upon AX doping, the P1 and P2 peaks increase in intensity and the bandgap absorption is further bleached compared to conventional doping, indicating that AX can achieve higher doping levels at the same $F_4TCNQ$ concentration. b, c) Normalized IR absorption zooming in on the polaron P1 peak for all five P3HT crystallinities, with (b) showing conventionally-doped with ~20 mM $F_4TCNQ$ in *n*-BA and c) AX-doped with ~20 mM $F_4TCNQ$ and ~100 mM LiTFSI in *n*-BA. Although there is a clear blue-shift of the P1 transition for both AX- and conventionally-doped samples when the P3HT crystallinity decreases, the magnitude of the blue-shift is larger when anion-exchanged.

When conventionally doping P3HT with high concentrations of $F_4TCNQ$, the presence of $F_4TCNQ$ anions in the film are apparent from its absorption features located at 1.4, 1.6, 1.8 and 3.0 eV, which are labeled in **Figure 2.3a**. The spectrum also shows the presence of neutral $F_4TCNQ$ molecules, which absorb at 3.2 eV, indicating that at this high dopant concentration, not all the $F_4TCNQ$ molecules were able to oxidize the polymer backbone. In contrast, the AX-doped film has no $F_4TCNQ$ anion nor neutral absorption peaks, indicating that $TFSI^-$ anions successfully exchanged with the initial $F_4TCNQ$ anion species. We also see that the AX-doped film is more oxidized than the conventionally-doped sample, as indicated by higher P1 absorption intensity and greater depletion of the bandgap transition. These spectroscopic trends for the two doping methods are consistent across all five P3HT crystallinities, as shown explicitly in Figure S.3.1 in the SI.

When polarons become more localized, either because they reside on small-conjugation-length polymer segments or because they have a strong coulomb interaction with their counterions, their P1 absorption shifts to higher energies.[27,54,88,89] **Figures 2.3b** and **2.3c** show the normalized P1 absorption spectra for P3HT samples with all five degrees of crystallinity after conventional and AX doping, respectively, at high dopant concentration. For both doping methods, there is a clear blue-shift of the P1 band as the P3HT crystallinity decreases, indicative of increased polaron localization. When comparing the doped 99% RR and RRa P3HT samples in **Figure 2.3b**, there is a nearly 0.2 eV shift in the P1 peak position upon conventional doping, and an even larger shift upon AX doping, as seen in **Figure 2.3c**.

Along with the disorder-induced blue-shift, the spectra in **Fig. 2.3c** show a shape change of the compared to **Fig. 2.3b** due to a shoulder on the red-edge of the P1 band in the more highly crystalline P3HT samples. This red shoulder, located at ~0.25 eV, has been assigned as resulting from polarons present at high enough density that their P1 transition dipoles become *J*-coupled,

leading to a red-shift of the transition.[54] The AX-doped samples for all P3HT crystallinities also show broadening on the blue side of the P1 absorption band relative to the conventionally-doped samples, an indication that more localized polarons are being formed in amorphous regions of P3HT. This is because AX has a higher oxidative driving force for doping than conventional methods,[43] allowing more highly trapped polarons to be formed.

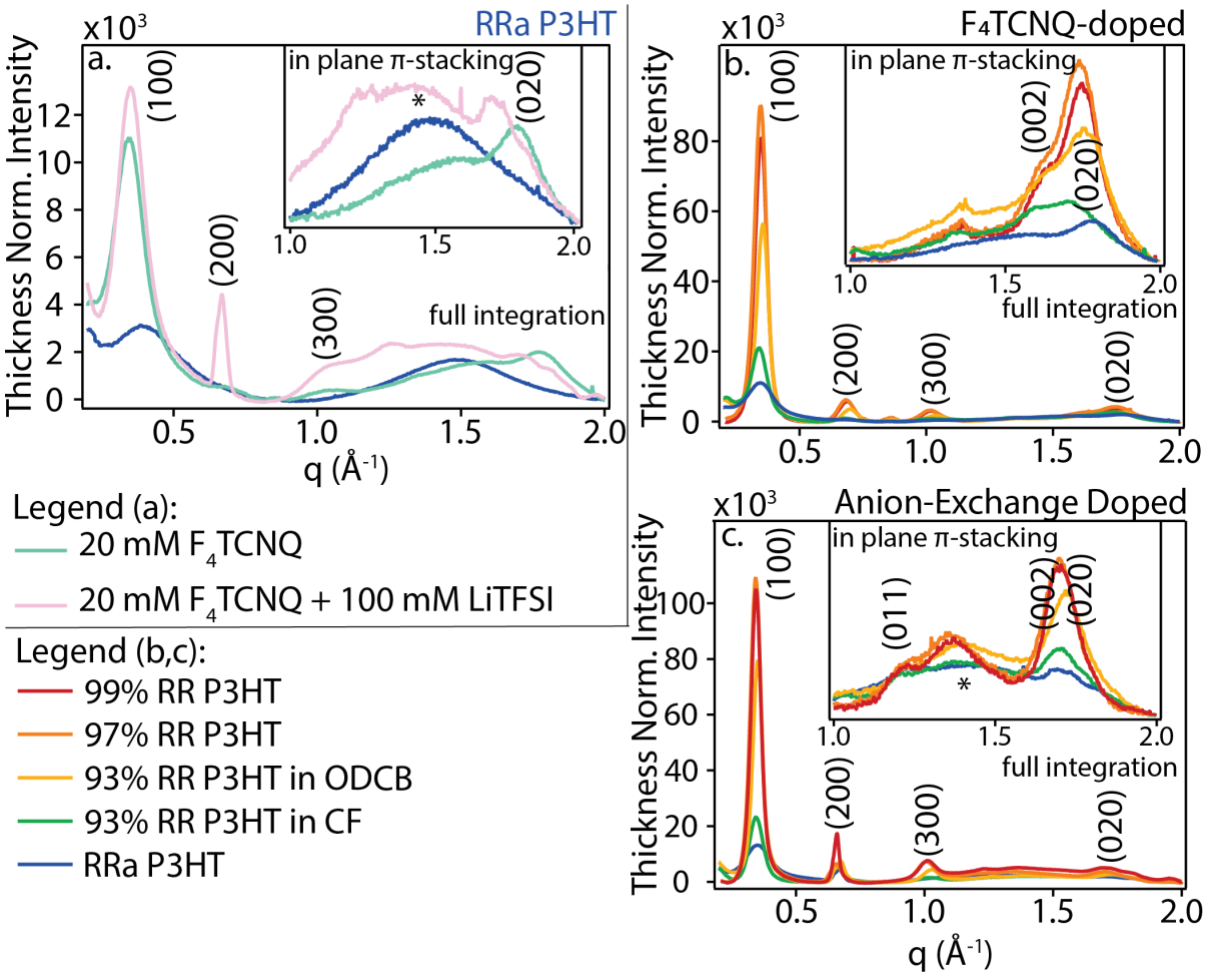


**Figure 2.4 Radially-Integrated GIWAXS for Conventionally and AX-Doped P3HT Films**
Figure 2.4. Thickness-normalized radial integrations of GIWAXS diffractograms of a) RRa P3HT undoped (blue), conventionally doped (aquamarine) with ~20 mM $F_4TCNQ$, and AX-doped (pink) with ~20 mM $F_4TCNQ$ and ~100 mM LiTFSI. AX-doping enhances the crystallinity of RRa P3HT such that overtones become apparent in the full integration. The in-plane integration is shown in the inset, expanded at high *q*, to emphasize the in-plane $\pi$-stacking component. Similar scattering plots for the other four polymers can be found in the SI. Radial integrations of GIWAXS diffractograms of all five polymers conventionally doped with ~20 mM $F_4TCNQ$ and AX-doped with ~20 mM $F_4TCNQ$ and 100 mM LiTFSI are shown in

figures b and c, respectively. As the initial film crystallinity decreases, the relative changes to the polymer film increases upon both doping methods.

In addition to the electronic structure of the doped P3HT films with different initial crystallinities, we also studied how the films' morphology changed upon doping and the formation of charge carriers. **Figure 2.4a** shows the radially-integrated GIWAXS diffractogram of RRa P3HT undoped (blue), conventionally doped with ~20 mM $F_4$TNCQ (aquamarine) and AX-doped with ~20 mM $F_4$TCNQ and ~100 mM LiTFSI (pink). The data shown in **Fig 2.4a** for RRa and **Figure S.2.4.1** for the other four polymers, show that both doping methods change the unit cell to accommodate the dopant counterion, causing a phase transition to a new polymorph. [90,91] Evidence for this phase transition includes the lamellar (*h*00) peaks shifting to lower *q* (larger *d*-spacing) and the $\pi$-stacking (020) peak shifting to higher *q* (smaller *d*-spacing). The doping-induced crystallinity increase is particularly evident for RRa P3HT, where the AX-doped sample shows a significant (200) overtone. In both doping mechanisms, but especially so in the AX-doping case, the relative degree of crystallinity increases upon doping, as evidenced by an increase in (100) peak intensity. This type of doping-induced ordering results from the dopant counterions filling space, allowing more ordered structures to be created from previously amorphous regions of the P3HT films.[33,53] The integrated GIWAXS diffractograms for all five polymers conventionally doped and AX-doped with high-concentration $F_4$TCNQ are shown in **Figure 2.4b** and **c**, respectively. In both doping methods, the relative crystallinities of the doped films retain their original order (although the 99% RR sample has a similar crystallinity as the 97% RR sample after doping; see the SI). Thus, the original degree of ordering largely survives the doping process, despite doping inducing order in regions of the films that were originally disordered.

## 2.3.3 Hall Effect Measurements on AX-Doped P3HT Films

Now that we understand the structural changes associated with conventional and AX doping of P3HT films with different degrees of crystallinity, we turn next to exploring the electronic properties of the doped films through Hall effect measurements.[85,92] **Figure 2.5** shows how the conductivity (**Fig. 2.5a**), carrier density (**Fig. 2.5b**), and carrier mobility (**Fig. 2.5c**) of doped P3HT films vary with crystallinity, dopant concentration, and doping method; the individual values are shown in **Table S.2.6.1** in the SI. The Hall data shows that the increase in conductivity for all five morphologies of the conventionally-doped samples upon increasing the doping concentration from ~3.5 mM to ~20 mM $F_4TCNQ$ is due to an equivalent increase in both carrier density and mobility. This is due to both reorganization of the amorphous regions and an increase in doping.

In AX doping there is a significant enhancement in conductivity relative to conventional doping regardless of the initial dopant concentration. For all five polymer crystallinities, AX doping results in an order of magnitude increase in conductivity relative to conventional doping when initiator limited at a ~3.5 mM $F_4TCNQ$ dopant concentration. The Hall measurements show that this conductivity increase in AX-doped films is primarily due to an increase in carrier mobility; the carrier densities for the more crystalline polymers, 99% RR, 97% RR, and 93% RR cast from ODCB increase only modestly with the addition of LiTFSI at initiator-limited $F_4TCNQ$ concentrations. Meanwhile the less crystalline 93% RR P3HT sample cast from CF shows a carrier density that doubles when AX-doped with initiator-limited $F_4TCNQ$ concentrations relative to the conventionally-doped sample. The carrier mobility for each crystalline sample AX-doped with ~3.5 mM $F_4TCNQ$, at least doubles, and in the 93% RR cast from CF case, triples in value, compared with the conventionally-doped samples at the same dopant concentration, indicating that initiator-limited AX predominantly increases the mobility.

RRa P3HT has no measurable conductivity when conventionally doped with ~3.5 mM $F_4$TCNQ, therefore no direct comparisons can be made in terms of its carrier density and carrier mobility upon the addition of LiTFSI. However, upon the addition of inert salt, a measurable conductivity of 0.16 S $cm^{-1}$ is observed at initiator-limited concentrations of $F_4$TCNQ in RRa P3HT.

Although for the initiator-limited case, the conductivity enhancement seen between conventional and AX doping is mobility dominated regardless of polymer morphology, this finding is not replicated in the high-concentration doping regime. When comparing AX and conventional doping at the higher $F_4$TCNQ concentration, we notice that the underlying cause of the conductivity increase is dependent on the initial polymer structure. Given that LiTFSI allows $F_4$TCNQ the potential to dope the amorphous sites, we would expect a large increase in carrier density resulting in an increase in conductivity. However, we find that this is only true in the less-crystalline polymer environments, such as 93% RR P3HT cast from CF and RRa P3HT. In high-concentration AX doping, CF-cast 93% RR P3HT experiences over an order of magnitude enhancement in carrier density compared to conventional doping, while both 99% RR and 97% RR P3HT, show a carrier density increase of only ~1.3 compared to conventional doping. We hypothesize this is due to $F_4$TCNQ's relatively modest doping potential; $F_4$TCNQ's weak ability to dope amorphous sites on its own means that the oxidative boost upon adding LiTFSI leads to a greater increase in carrier density that depends on the relative fraction of amorphous regions available for doping.

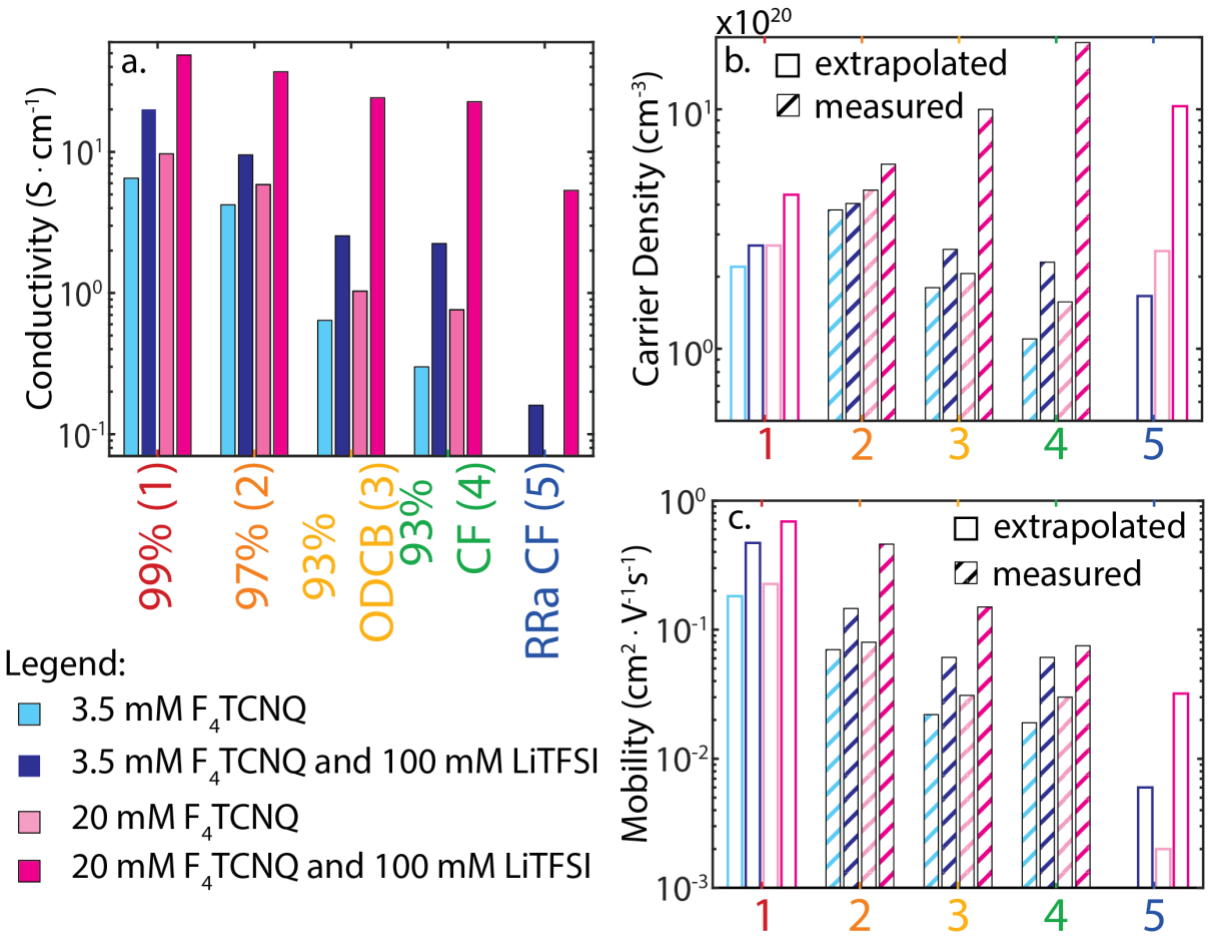


**Figure 2.5 Conductivity, Carrier Density, and Mobility Values for Conventionally- and AX-Doped P3HT with Varying Crystallinities**

Figure 2.5 A) Electrical conductivity of all five polymer crystallinities doped with two varying concentrations of $F_4TCNQ$, both conventionally and AX-doped. Hall effect measurements were used to plot B) the carrier density and C) carrier mobility of 97% RR P3HT, 93% RR P3HT cast from ODCB, and 93% RR P3HT cast from CF (filled bars). The values for 99% RR and RRa P3HT (open bars) are determined using carrier densities estimated using a calibration curve; see text. Corresponding values and errors for measurements can be found in Table S.6.1 in the SI.

Although the initially more amorphous P3HT samples experience a carrier-density dominated conductivity increase upon addition of LiTFSI, the more highly ordered materials, 99% RR and 97% RR P3HT, both show a mobility-dominated conductivity increase when comparing the conventional and AX doping methods at high concentrations of $F_4TCNQ$. The measured Hall data in **Figure 2.5c** shows that 97% RR P3HT experiences a significant increase in mobility from 0.08 $cm^2(V{\cdot}s)^{-1}$ when conventional doping to 0.46 $cm^2(V{\cdot}s)^{-1}$ with the addition of LiTFSI, a nearly 6-

fold increase. Although 97% RR P3HT does experience a slight increase (×1.3) in carrier density upon high-concentration AX doping, the material does not have enough initially amorphous regions to reorder and thus improve the carrier density to the same degree as an initially-disordered polymer. Similarly, the (extrapolated using the integrated P1 peak area) data for the 99% RR P3HT sample shows that the conductivity enhancement from conventional doping to AX doping at the high $F_4TCNQ$ concentration is mostly due to a 3-fold increase in carrier mobility. Although both 99% RR and 97% RR P3HT do show a slight carrier density increase with AX doping at high concentrations, the conductivity increase is primarily dominated by the mobility enhancement.

Thus far, we have established that relative to conventional doping, more highly ordered polymers experience a carrier-mobility dominated conductivity enhancement upon high concentration AX doping while more disordered P3HT samples show a carrier-density dominated conductivity increase upon AX doping. This makes it interesting to explore how AX doping changes the conductivity of the 93% RR P3HT cast from ODCB samples, which have an intermediate degree of order. The 93% RR P3HT cast from ODCB sample experiences a greater than 20-fold increase in conductivity upon AX doping, from 1 $S \cdot cm^{-1}$ when conventionally doped with ~20 mM $F_4TCNQ$ to 24 $S \cdot cm^{-1}$ when adding ~100 mM LiTFSI. This conductivity increase results from a nearly 5-fold increase in both carrier density and carrier mobility. Because the polymer shows a significant crystallinity increase upon AX doping compared to conventional doping (see **Fig.S.2.4.1.c**), we can attribute the carrier density increase to amorphous regions reordering to accommodate more polarons.

Given that reordering of amorphous sites leads to an increase in carrier mobility, it is perhaps not surprising that the nearly 80-fold enhancement of RRa P3HT's conductivity upon the addition of salt in the high concentration regime results primarily from an increase in carrier mobility.

Indeed, the mobility values (extrapolated using the integrated P1 peak area) show that the carrier density increases by a factor of four while the mobility increases by over an order of magnitude. This is a direct reflection of the significant increase in coherence length RRa P3HT experiences upon AX doping (cf. **Fig. 2.4a**), indicating a substantial reordering of the polymer that increases the ability for a charge carrier to migrate through the formerly-amorphous matrix.

Overall, the trends observed in this study show how the initial degree of crystallinity determines how the doping method and concentration affect the electronic characteristics of doped P3HT. We observed a mobility-dominated conductivity increase for AX relative to conventional doping across all crystallinities at initiator-limited concentrations. This is likely due to polymer reorganization of amorphous regions upon AX doping, which has a greater impact on initially disordered materials. In contrast, at high doping concentrations, there is a significant structural dependence as to whether mobility or carrier density dominates the conductivity increase observed with AX doping. This is because at high dopant concentrations, the increased doping potential observed in AX allows the ability to both dope and induce order in regions that were initially amorphous. This induced order impacts initially amorphous polymers more significantly than initially crystalline materials. Thus, we see that the initially amorphous polymers' conductivity increase at high-concentration AX relative to conventional doping was primarily due to a carrier density increase, while the conductivity enhancement seen in crystalline polymers was mainly due to a mobility increase.

## 2.4 Conclusions

Many groups have used the AX doping technique to obtain some of the highest conductivities the field has seen thus far.[39,43,51] Here, we work to provide a fundamental understanding of how

the polymer structure interacts with the AX doping mechanism. By combining X-ray scattering, optical spectroscopy, and Hall effect measurements, we were able to study the carrier mobility and density produced by AX doping and how they are affected by the polymer morphology.

We tested AX doping on a series of P3HT polymers with five different degrees of crystallinity by using different polymer regioregularities and solvent casting conditions. First, we explored how AX increased the conductivity relative to conventional doping by using initiator-limited $F_4TCNQ$ concentrations. We observed a conductivity increase due to enhancement of the carrier mobility upon initiator-limited AX doping across all P3HT crystallinities, which we believe is due to the induced structural reordering seen upon doping.

The trends for high-concentration AX compared to high concentration conventional doping are more structurally dependent and showed both a mobility- and a carrier-density-dominated conductivity increase depending on the initial crystallinity of the material. We observed that when the P3HT was initially less crystalline, high-concentration AX doping reordered amorphous sites in a way that did not happen with conventional doing, leading to a net increase in doping level and therefore a carrier-density-dominated conductivity increase. Meanwhile, initially-crystalline polymers experience a significant increase in carrier mobility upon AX doping, likely due to the reduction of barriers at grain boundaries between distinct crystalline regions due to the extra doping power.

The relationship between polymer structure and its electronic properties is important to consider when designing a system for device applications. This study will, therefore, allow researchers to determine the dominating component of a conductivity increase seen in AX doping and thereby tune the enhancement for a particular application.

## 2.5 Supplemental Information for Chapter 2

1. Materials

The four different regioregularities of poly(3-hexylthiophene-2,5-diyl) (P3HT) were purchased from three different companies: 99% regioregular (RR) P3HT was purchased from Tokyo Chemical Industry, 97% RR P3HT was purchased from Osilla LTD, 93% RR P3HT and Regiorandom P3HT were both purchased from Reike Metals. All four polymers were used as-is. The molecular oxidant, 2,3,5,6-tetrafluoro-tetracyanoquinodimethane ($F_4$TCNQ) was purchased from Osilla LTD and used as received. The inert salt, lithium bis(trifluoromethane) sulfonimide (LiTFSI) was purchased from Sigma-Aldrich and was also used as received. The solvents, 1,2-dichlorobenzene (ODCB, anhydrous, 99%), chloroform (CF, anhydrous, >99%) and *n*-butyl acetate (*n*-BA, anhydrous, >99%) were all purchased from Sigma-Aldrich and used as received. Gold shot, used for thermally evaporating metal contacts for the electrical measurements, was purchased from the Kurt J. Lesker Company.

2. Experimental Methods

2.1 *Film Preparation*

Glass substrates were cut into 1.3 x 1.3 cm squares after which they were cleaned by sonication for 10 minutes in soapy water, and subsequently sonicated for 5 minutes each in DI water, then acetone, then isopropanol after which they are dried using nitrogen gas. The cleaned and dried substrates were plasma etched for 30 minutes before transferring them to a nitrogen glove box for sample deposition.

2.1.1 *Polymer Casting Conditions*

99%, 97%, and 93% RR P3HT were all dissolved in ODCB at a 20 mg $mL^{-1}$ (2% w/v) concentration. The solutions were heated at 45 ºC for 45 minutes or until all the polymer was dissolved. 93% RR P3HT and RRa P3HT were also dissolved in CF at a 10 mg $mL^{-1}$ (1% w/v) concentration without heating until they were completely dissolved. To make uniformly coated films, 20 μL of polymer solution was used to cast the ODCB-dissolved polymers while 35 μL was used to cast the CF-dissolved polymers. All polymer films were spin-coated onto the substrate at 1000 RPM for 60 seconds, followed by spinning at 4000 RPM for 10 seconds. The polymer films were left to completely dry for at least 30 minutes prior to doping.

### 2.1.2 *Polymer Doping Conditions*

Conventional dopant solutions containing $F_4TCNQ$ and anion-exchange dopant solutions containing both $F_4TCNQ$ and LiTFSI were freshly prepared by dissolving them in *n*-BA and given time to fully dissolve. 100 μL of dopant solution was pipetted on top of the pre-cast P3HT polymer films. An 80 second delay was implemented before spinning off the excess solution for 10 seconds at 4000 RPM.

## 2.2 Absorption Spectroscopy

Samples were prepared as discussed on glass substrates for UV-Visible absorption spectroscopy. UV-Vis was taken on a Jasco V-770 spectrophotometer at a scan speed of 400 nm/min from 250-3200 nm with a sampling interval of 1 nm and a slit width of 1 nm. In order to capture the entirety of the P1 peak, Fourier Transform Infrared spectroscopy (FTIR) was taken using the Agilent Technologies Cary 600 Series FTIR Spectrometer from 400-6000 cm-1. Samples were cast onto KBr plates for FTIR. UV-Vis and FTIR data were stitched together in the same way as highlighted in ref [93].

## 2.3 GIWAXS Measurements

Films for 2-D GIWAXS measurements were prepared on 1.5 cm x 1.5 cm silicon substrates. The substrates were cleaned following the same process as for the glass substrates. Measurements were performed at the Stanford Synchrotron Radiation Lightsource on beamline 11-3 using a wavelength of 0.9742 Å with an incidence angle of 0.12°. 2D diffractograms (shown in figure S.4.1) were radially integrated (0-10° for in-plane, 70-80° for out-of-plane, and 0-180° for full integrations) to obtain the 1D diffraction patterns shown in the main text.

## 2.4 Electrical Measurements

Before conducting any electrical measurements, a 45 nm-thick layer of gold was deposited onto the film using an Angstrom Engineering Nexdep thermal evaporator at pressures below $1x10^{-6}$ torr at a deposition rate of 0.5 Å/s.

Resistivity, carrier density, and mobility values were obtained using LakeShore Cryotronics' MeasureReady M91 FastHall instrument. For these measurements, a constant current of 10 μA was used along with a 1.0236 Tesla magnetic field for the Hall measurements. We converted the measured resistivity values to conductivities using the thickness of each sample measured using a Dektak 150 surface profilometer. Each sample was measured at least three times to ensure an accurate thickness was measured.

Hall voltages were measured and converted to carrier densities using equation 1.5 or $n = \frac{IB}{V_H ed}$, where $n$ is the carrier density, $I$ is the applied current, $B$ is the applied magnetic field, $V_H$ is the Hall Voltage, $e$ is the fundamental charge, and $d$ is the sample's thickness. It is important to note that there are disadvantages of the measurement. For example, during the process, we flip the direction of the magnetic field by physically turning the magnet. The time in which the magnet is

flipped can take up to 30 seconds and as such, the two measurements of the hall voltage can be separated by a decent amount of time. If the temperature or humidity of the sample changes between the two measurements, this error will be incorporated into the calculation of the Hall coefficient.[52]

Additionally, it is vital for the geometry of the electrodes to be as perfectly square as possible to mitigate the misalignment voltage, which is the measured voltage at zero magnetic field and is often the largest intrinsic error in a Hall measurement.[94] This error is purely due to the geometry of the electrodes. Therefore, we have machine-shopped evaporation masks that perfectly place 1mm square-electrodes 1cm apart as an attempt to mitigate any geometrical errors in the Hall effect measurements.

3. UV-Vis-NIR Spectra of High-Concentration and Initiator-Limited Samples

**Figure S.2.3.1** shows the absorption spectra of a) 97% RR P3HT cast from ODCB, b) 93% RR P3HT cast from ODCB, c) 93% RR P3HT cast from CF, and d) RRa P3HT cast from CF, conventionally doped with ~20 mM (6 mg $mL^{-1}$) $F_4TCNQ$ and anion-exchange doped with ~20 mM (6 mg $mL^{-1}$) $F_4TCNQ$ and ~100 mM (30 mg $mL^{-1}$) LiTFSI. It is clear that across all five polymers, the $F_4TCNQ^{1-}$ peaks at 1.4, 1.6, 1.8, and 3.0 eV disappear upon the addition of salt, confirming exchange of the counterions. Each polymer also experiences a nearly complete depletion of the bandgap upon AX doping, as well as an increase in P1 intensity, further confirming an increase in carrier density. Although the peak at 3.0 eV from $F_4TCNQ^{1-}$ has been completely exchanged upon the addition of salt, all of the polymers still show an absorption peak at 3.2 eV, which is where the $F_4TCNQ^0$ species absorbs, indicating that despite the increase in doping potential with the salt and the driving force for AX, at these high dopant concentrations, there is still some $F_4TCNQ$ that is not able to dope the polymer and remains in the film.

**Figure S.2.3.2.** shows the P1 absorption spectra for all five polymers at the low doping regime of ~3.5 mM (1 mg mL$^{-1}$) $F_4TCNQ$ conventionally doped and ~3.5 mM (1 mg mL$^{-1}$) $F_4TCNQ$ with ~100 mM (30 mg mL$^{-1}$) LiTFSI for initiator-limited AX doping. Overall, each polymer shows a higher P1 peak intensity upon AX compared to the conventional doping case, confirming an increase in doping and therefore an increase in carrier density. Each peak also experiences a slight red-shift in the P1 peak location which has been attributed to an increase in mobility in a previous publication.[31]

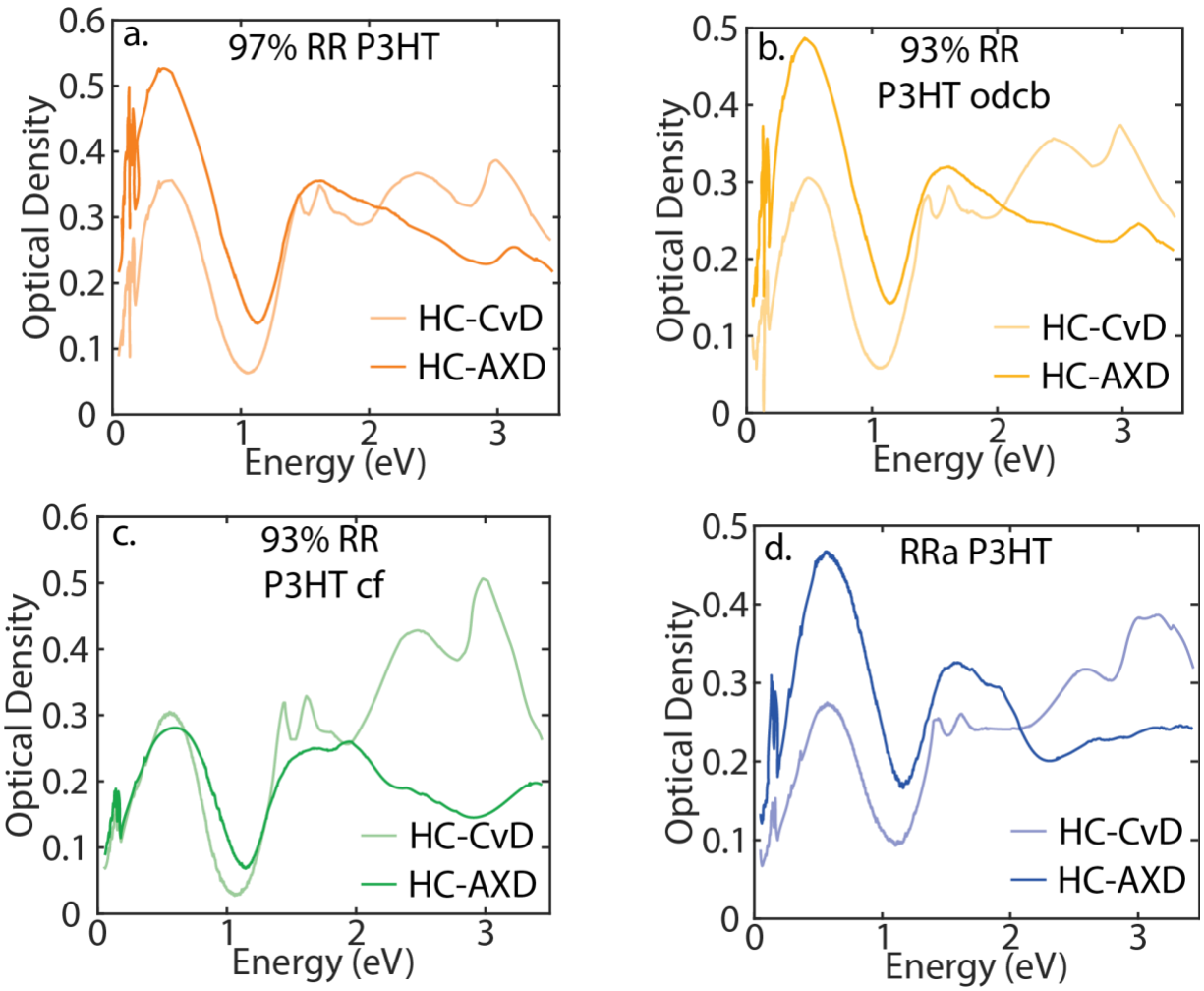


**Figure S.2.3.1 UV-Vis-NIR of High Concentration $F_4TCNQ$**

Figure S.2.3.1 UV-Vis-NIR plots for a) 97% RR P3HT, b) 93% RR P3HT cast from ODCB, c) 93% RR P3HT cast from CF, and d) RRa P3HT conventionally doped with ~20 mM $F_4TCNQ$ (HC-CvD) and anion-exchange doped with ~20 mM $F_4TCNQ$ and ~100 mM LiTFSI (HC-AXD).

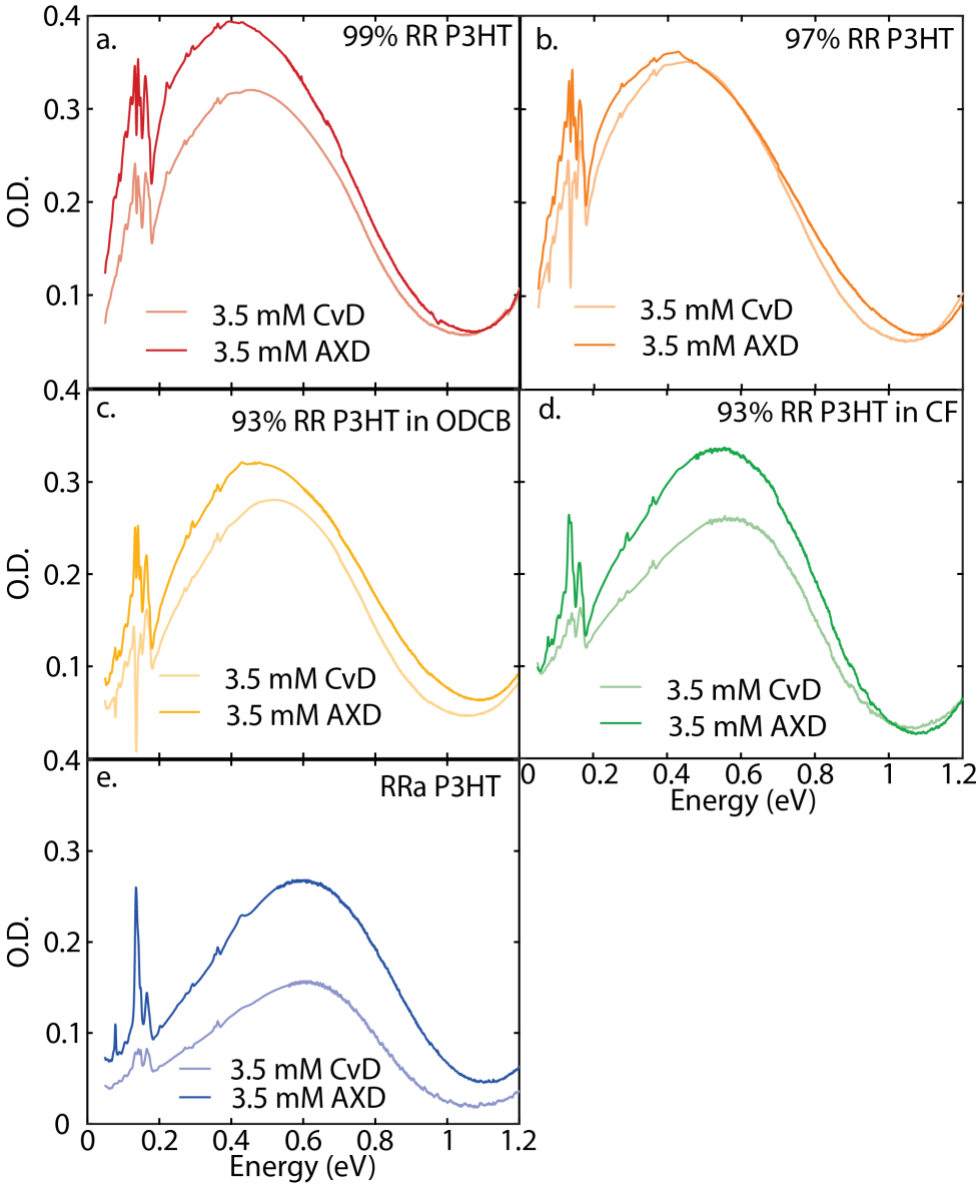


**Figure S.2.3.2 UV-Vis-NIR Spectra of Five Varying P3HT Crystallinities Initiator Limited with 3.5 mM $F_4TCNQ$**

Figure S.2.3.2 Absorption spectroscopy for all five polymers conventionally doped with ~3.5 mM (1 mg $mL^{-1}$) of $F_4TCNQ$ (CvD) and anion-exchange doped with ~3.5 mM F4TCNQ and ~100 mM (30 mg $mL^{-1}$) LiTFSI (AXD). Plotted are a) 99% RR P3HT, b) 97% RR P3HT, c) 93% RR P3HT cast from ODCB, d) 93% RR P3HT cast from CF, and e) RRa P3HT.

4. 1D Diffractograms of Conventionally doped and AX-doped P3HT and Calculated Coherence Lengths of Undoped and AX-Doped P3HT

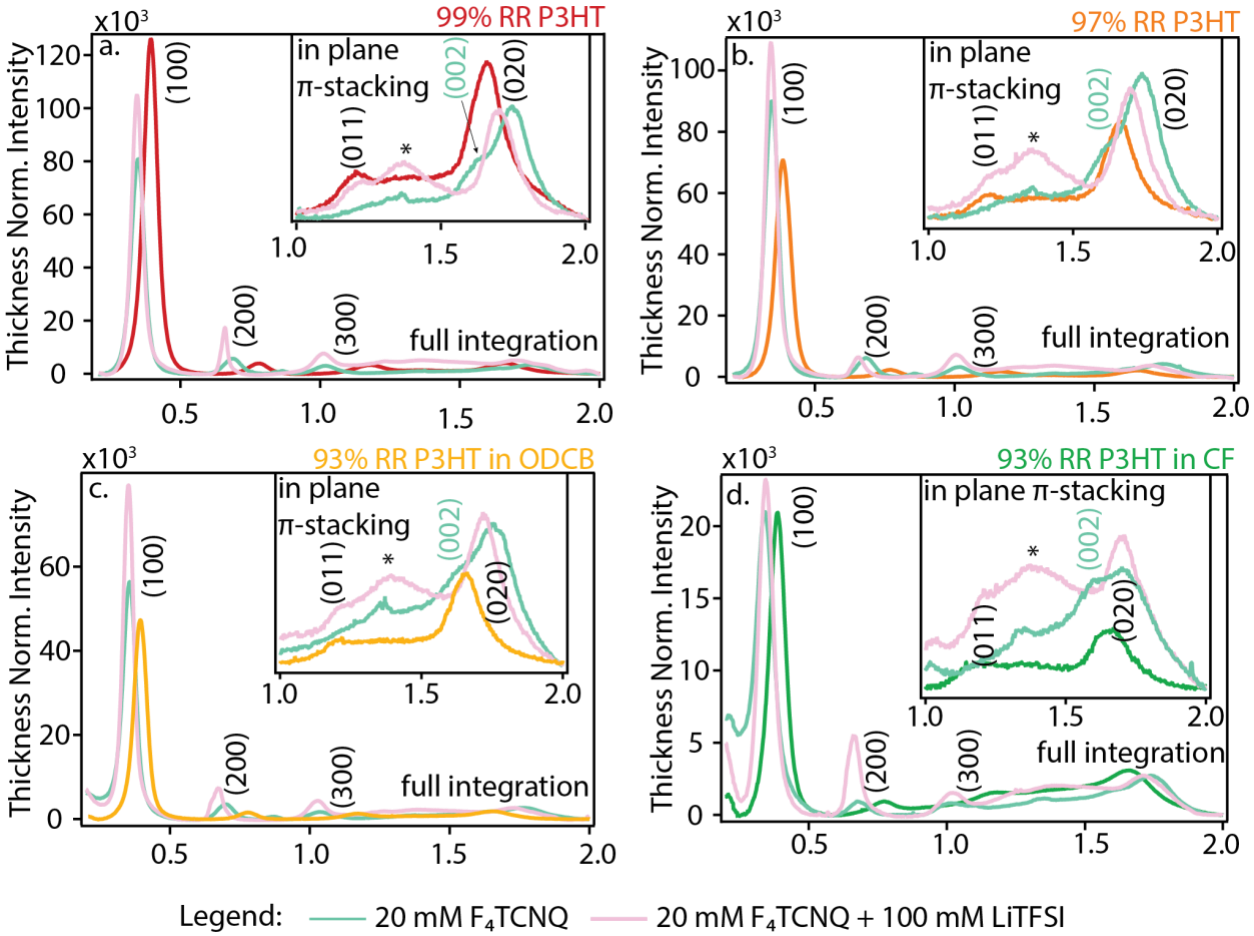


**Figure S.2.4.1 1D GIWAXS diffractograms of all polymers undoped, CD, and AXD at high $F_4TCNQ$ concentration**

Figure S.2.4.1 Radially-integrated and thickness normalized 1D diffractograms of all five crystallinities undoped, conventionally doped with ~20 mM $F_4TCNQ$ (aquamarine) and AX-doped with ~20 mM $F_4TCNQ$ and ~100 mM LiTFSI (pink). Each plot shows the full integration with the inset highlighting the in-plane $\pi$-stacking direction. In the inset, the (020) and amorphous- $\pi$ peak are highlighted.

Figure S.2.4.1a-d show the radially-integrated GIWAXS diffractograms for all five polymer environments undoped, conventionally doped (aquamarine) and AX-doped (pink). In the main text, we discussed how the (100) peak intensity increased as a result of both doping methods which led to an increase in polymer order. This is true for all polymer environments studied here except for 99% RR P3HT. Figure S.2.4.1.a shows this exception. This sample has by far the highest degree of crystallinity prior to doping, and the need for the dopant counterion to intercalate into the film through the few amorphous regions that are available disrupts some of the crystalline domains, leading to a small doping-induced disordering.

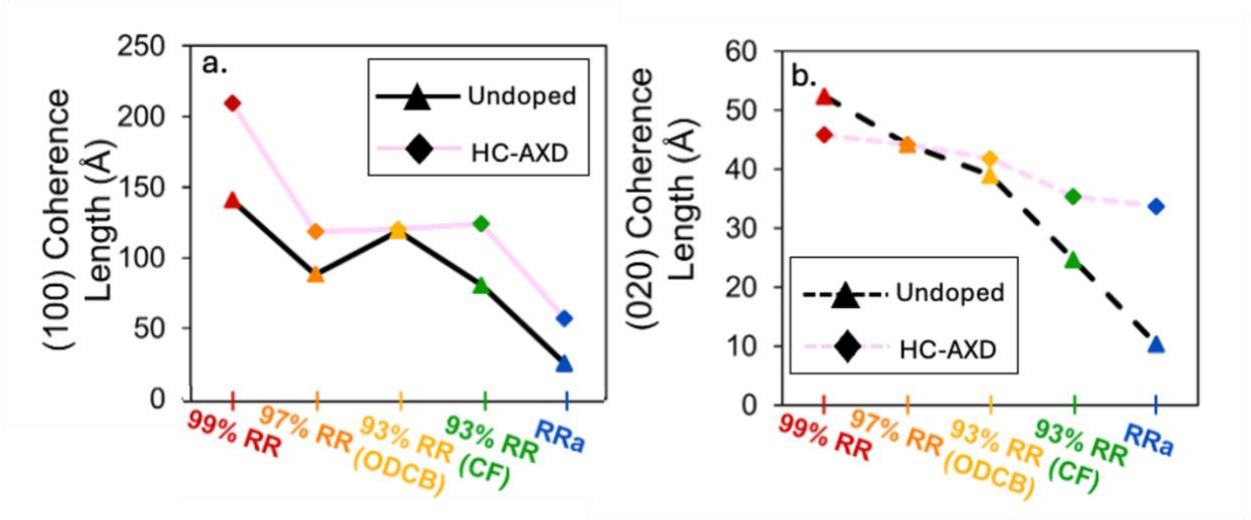


**Figure S.2.4.2 (100) and (020) Coherence Lengths of Undoped and Highly Anion-Exchange Doped P3HT**

Figure S.2.4.2 The coherence lengths of (100) and (020) peaks for the as-cast polymers (black traces) and for the polymers doped with high concentration anion-exchange (HC-AXD), shown in the pink traces.

**Figure S.2.4.2** shows the calculated coherence lengths of undoped (a) and AX doped with high concentration of F4TCNQ (b). These coherence lengths can provide information about the size of the crystalline domains within the material. They were calculated using the Scherrer equation and the inverse of the peak widths.

**Table S.2.6.1** shows the conductivity, mobility, and carrier density values as well as the errors associated with those that are plotted in Figure 2.5 in the main text.

**Figure S.2.6.1** shows the correlation plot that was used to estimate the carrier density and mobility values for 99% RR P3HT and RRa P3HT, values of which are shown in Table S.2.6.1. The P1 peak areas were first weighed by their relative oscillator strength then obtained using the OriginPro program following the guidelines highlight in ref [93]. Once P1 peak integrations were preformed, they were plotted against the corresponding carrier density measured from Hall. We then integrated the P1 peaks for the samples that could not be measured by Hall and found the approximate carrier density by plugging the area in for x in the linear relationship equation

highlighted in **Figure S.2.6.1**. Using the extrapolated carrier densities, we were able to calculate the mobility from the measured conductivity and thickness values. The extrapolated values for 99% RR P3HT and RRa P3HT are shown in Table S.1.6.1.

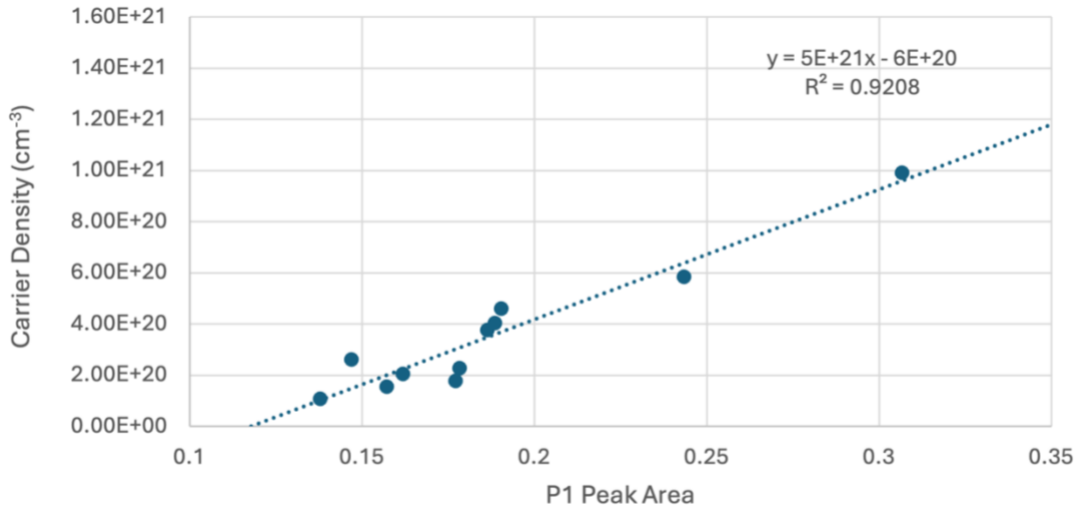


**Figure S.2.6.1 Correlation Plot used to Extrapolate Carrier Density and Mobility Values for 99% RR and RRa P3HT**

Figure S.2.6.1 A correlation plot between the P1 peak area and the measurable carrier densities of the three measurable polymers, 97% RR P3HT, 93% RR P3HT cast from both ODCB and CF. The relationship shows a clear linear dependence between the two parameters. The linear equation and the goodness of fit parameter are also presented in the plot.

**Table S.2.6.1 Values Obtained by Hall Effect Measurements**

Table S.2.6.1 Contains all the values obtained by Hall effect measurements presented in Figure 2.5 in the main text.

| Polymer | Conductivity (S * cm$^{-1}$) | | | |
|---|---|---|---|---|
| | ~3.5 mM $F_4TCNQ$ CD | ~3.5 mM $F_4TCNQ$ AXD | ~20 mM $F_4TCNQ$ CD | ~20 mM $F_4TCNQ$ AXD |
| 2% 99% RR P3HT ODCB | 6.5 | 19.98 | 9.69 | 48.64 |
| 2% 97% RR P3HT ODCB | 4.22 | 9.52 | 5.86 | 36.98 |
| 2% 93% RR P3HT ODCB | 0.64 | 2.54 | 1.03 | 24.16 |

| | | | | |
|---|---|---|---|---|
| 1% 93% RR P3HT CF | 0.3 | 2.24 | 0.76 | 22.69 |
| 1% RRa P3HT CF | N/A | 0.16 | 0.07 | 5.33 |
| | Mobility ($cm^2 * V^{-1} * s^{-1}$) | | | |
| | ~3.5 mM $F_4TCNQ$ CD | ~3.5 mM $F_4TCNQ$ AXD | ~20 mM $F_4TCNQ$ CD | ~20 mM $F_4TCNQ$ AXD |
| 2% 99% RR P3HT ODCB | 0.182 | 0.47 | 0.226 | 0.689 |
| 2% 97% RR P3HT ODCB | 0.070 ± 0.001 | 0.146 ± 0.003 | 0.080 ± 0.001 | 0.46 ± 0.02 |
| 2% 93% RR P3HT ODCB | 0.022 ± 0.001 | 0.061 ± 0.004 | 0.031 ± 0.001 | 0.15 ± 0.02 |
| 1% 93% RR P3HT CF | 0.019 ± 0.001 | 0.061 ± 0.004 | 0.030 ± 0.001 | 0.075 ± 0.004 |
| 1% RRa P3HT CF | N/A | 0.006 | 0.002 | 0.032 |
| | Carrier Density ($cm^{-3}$) x1e20 | | | |
| | ~3.5 mM $F_4TCNQ$ CD | ~3.5 mM $F_4TCNQ$ AXD | ~20 mM $F_4TCNQ$ CD | ~20 mM $F_4TCNQ$ AXD |
| 2% 99% RR P3HT ODCB | 2.2 | 2.7 | 2.7 | 4.4 |
| 2% 97% RR P3HT ODCB | 3.8 ± 0.1 | 4.04 ± 0.07 | 4.60 ± 0.07 | 5.9 ± 0.2 |
| 2% 93% RR P3HT ODCB | 1.8 ± 0.2 | 2.60 ± 0.08 | 2.06 ± 0.09 | 10 ± 1 |
| 1% 93% RR P3HT CF | 1.1 ± 0.6 | 2.3 ± 0.2 | 1.57 ± 0.07 | 19 ± 1 |
| 1% RRa P3HT CF | N/A | 1.66 | 2.56 | 10.3 |

# Chapter 3

# Formation of Li-$F_4$TCNQ Complex During High Concentration Anion-Exchange Doping of Semiconducting Polymers

## 3.1 Introduction

Conjugated polymers are a promising class of organic materials for use in electronic devices such as thermoelectrics, solar cells, and organic photovoltaics.[62–64,66–68] Although their electrical conductivity is inherently low, the electrical properties can be improved by doping the polymer by either adding (*n*-doping) or removing (*p*-doping) an electron from the backbone.[14,41] The charge carriers created this way are accompanied by a distortion of the polymer backbone from aromatic to quinoid; the charge, unpaired spin, and structural rearrangement are collectively referred to as a polaron. In order to keep the system electrically neutral, a counterion generated by the doping process is also inserted into the polymer matrix.[41]

Recently, Yamashita *et al.* developed a new doping technique in which a molecular oxidant is introduced to the polymer in the presence of a high concentration of inert salt.[51] This method, referred to as anion-exchange (AX) doping, uses mass action to exchange the dopant counterion for a salt anion. AX doping provides the benefits of facile tunability of the choice of counterion as well as increased stability of the doped polymer films. This method also increases the energetic driving force for doping, thus improving the electrical conductivity compared to conventional doping methods. Because of these advantages, AX doping has been used to understand the role of

counterion size in determining the electrical properties,[34,59,95] as well as to explore the interaction between counterions and environmental factors such as humidity.[52]

AX doping has been studied using multiple different polymers and initiator dopants.[21,39,43,44,47,51,52,74,96–98] A standard combination includes the conjugated polymer poly(3-hexylthiophene-2,5-diyl) (P3HT), the well-studied molecular oxidant 2,3,5,6-tetrafluoro-tetracyanoquinodimethane ($F_4TCNQ$), and the inert salt lithium bis(trifluoromethane) sulfonimide (LiTFSI), the chemical structures of which can be found in **Figure 3.1**.

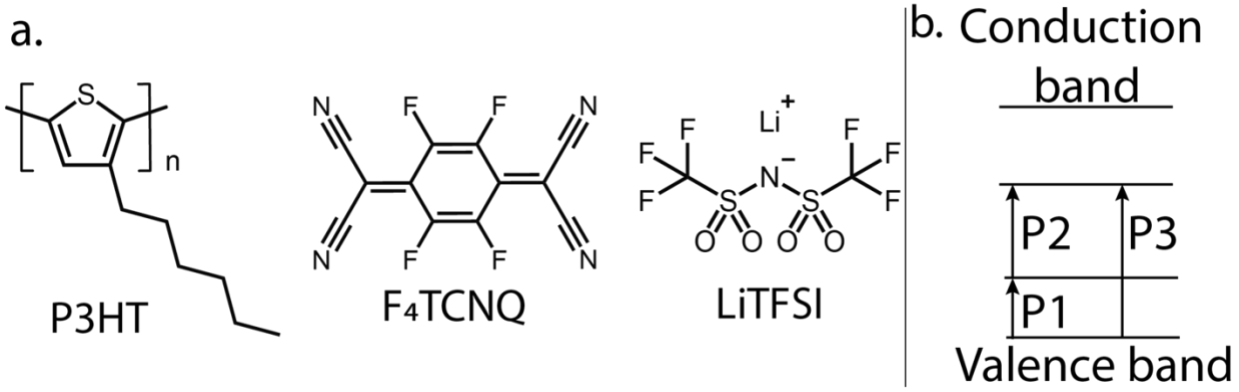


**Figure 3.1 Chemical Structures of Materials and Doped-Polymer Energy Diagram**
Figure 3.1 A) Structure of the polymer used in this study, P3HT, the initiator dopant, $F_4TCNQ$, and the salt used in AX doping, LiTFSI. B) An energy diagram of a doped conjugated polymer with the polaron optical transitions labeled.

Chemical *p*-type doping of P3HT forms two new intraband states within its bandgap between the polymer's valence band and conduction band. Upon doping, three new optical transitions emerge which correspond to the polaron transitions, labeled P1, P2, and P3 in the energy diagram of a doped polymer in **Figure 3.1b**. These transitions can be observed using FITR and UV-Vis spectroscopy, which is used to confirm doping. For example, when conventionally doping with $F_4TCNQ$ alone (as seen in **Figure 3.2a**, **b**, **d**, and **e**) the doped polymer shows both a P1 and P2 transition peak, confirming the formation of polarons. Because the $F_4TCNQ$ anion has absorption features in the UV/visible/NIR spectral region, we also can confirm its presence within the doped

polymer matrix. The $F_4TCNQ^-$ peaks (1.4, 1.6, 1.8, and 3.0 eV) are highlighted in **Figure 3.2a**, **b**, **d**, and **e** with an asterisk.

As previously stated, the AX doping method exchanges out the dopant counterion for the salt anion by mass action. The absence of $F_4TCNQ^-$ anion peaks suggests a successful exchange process as it is no longer the counterion to the charged carrier. The solid traces in **Figures 3.2a**, **3.2b**, and **3.2d** are AX doped with LiTFSI and suggest a successful counterion exchange, due to the disappearance of the $F_4TCNQ^-$ counterion peaks.

Although many studies have been published using AX doping,[39,43,51,52,99,100] the chemistry that takes place during this process involves more than simple mass action ion exchange. For example, we see the presence of two new electronic absorption peaks at 2.0 and 3.7 eV (which we refer to as the *Z* and *Z*' peaks, respectively, highlighted in **Figure 3.2a**, **3.2d**, and **3.2e**) that are not apparent in conventional doping. These absorption features have not been discussed or assigned in the literature despite being present in at least one other study independent from our group.[101] The purpose of this Chapter is to explore these two peaks that are associated with AX doping and determine what new electronic species is created via this process. Through the course of this Chapter, we will consider four different possible assignments for these peaks, including: (1) a P3 forbidden transition, (2) a charge transfer complex (CTC) between the polymer and initial dopant, (3) a dianion of the initial dopant formed via a double-doping process, or (4) a Li-$F_4TCNQ$ complex formed during the exchange process. A description of each potential assignment and its plausibility is discussed in the following paragraphs.

One idea is that the feature near 2.0 eV might be the P3 transition (cf. **Fig. 3.1b**), although P3 transitions in doped conjugated polymers are typically symmetry forbidden.[102,103] However, for P3HT, the P3 transition is a possibility because it is expected to absorb around 2.0 eV based on

**Fig. 3.1b**, which indicates that the energy of the P3 transition should be the sum of the energies of the P1 (0.5 eV) and P2 (1.5 eV) transitions. Thus, it is possible that the AX doping process could produce some type of structural change drastic enough to disrupt the symmetry such that the P3 transition is more strongly allowed.

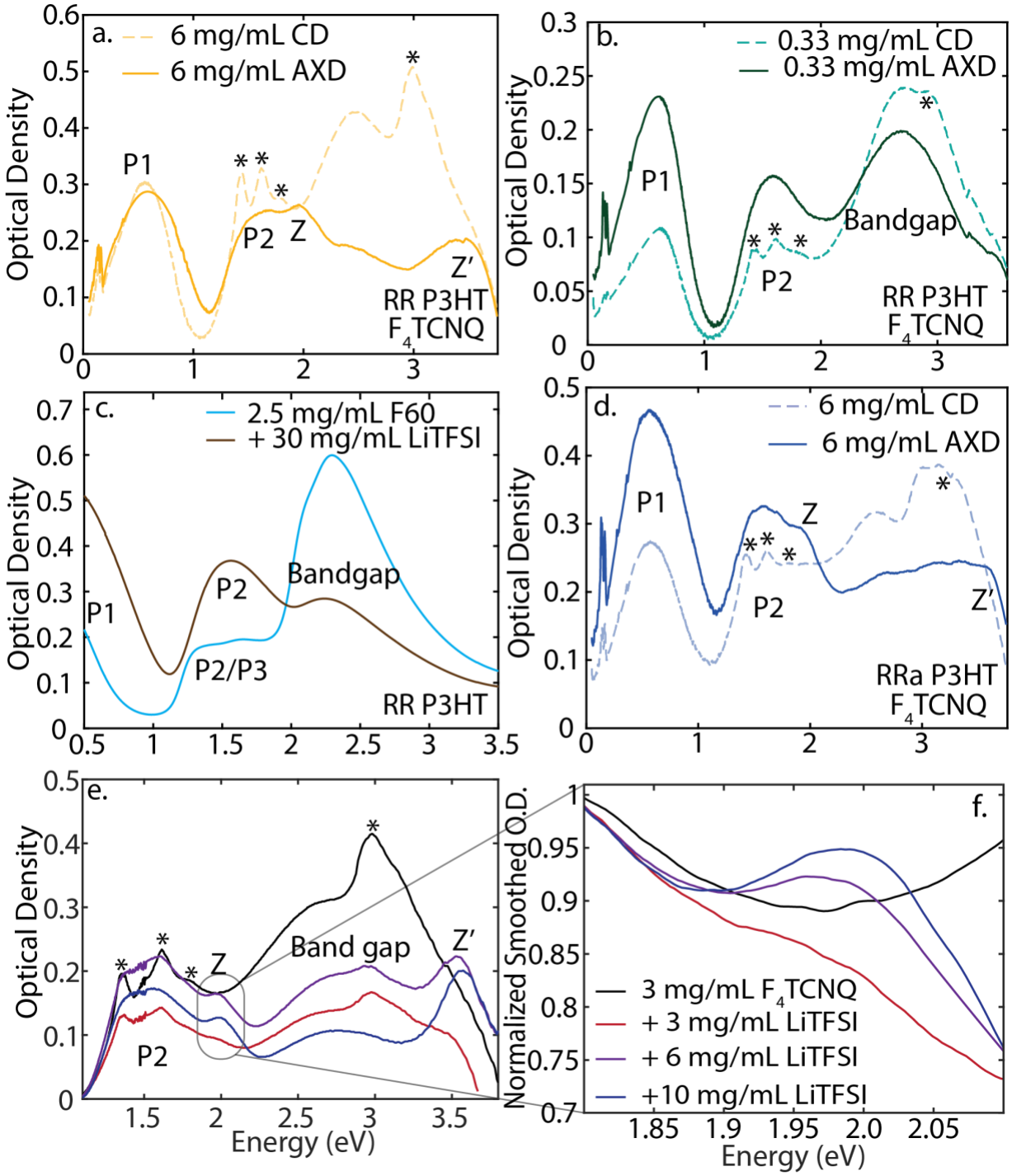


**Figure 3.2 Absorption Spectra of Doped P3HT Highlighting the *Z* and *Z'* Peaks**

Figure 3.2 A) Absorption spectra of regioregular (RR) P3HT conventionally doped (CD) with 6 mg $mL^{-1}$ $F_4TCNQ$ (dashed yellow trace) and anion-exchange doped (AXD) with 6 mg $mL^{-1}$ $F_4TCNQ$ and 30 mg $mL^{-1}$ LiTFSI (solid yellow trace). In the plot, the *Z* (2.0 eV) and *Z'* (3.7 eV) peaks are labeled as well as the polaron transition peaks and the $F_4TCNQ^{1-}$ absorption features which are denoted by an asterisk. B) Absorption spectra of RR P3HT doped with 0.33 mg $mL^{-1}$ of $F_4TCNQ$ (dashed teal trace) and AXD with 0.33 mg $mL^{-1}$ of $F_4TCNQ$ and 30 mg $mL^{-1}$ of LiTFSI (black trace). There is no evidence of either *Z* or *Z'*

peaks in the AXD sample. C) Absorption spectra of RR P3HT conventionally doped with 2.5 mg $mL^{-1}$ dodecaborane (DDB) perfunctionalized with (2,3,4,5,6-pentafluorobenzyloxy) (DDB-F60) plotted in blue. Plotted in brown is RR P3HT anion-exchange doped with 2.5 mg $mL^{-1}$ DDB-F60 and 30 mg $mL^{-1}$ LiTFSI. Of note is the lack of *Z* and *Z*' peaks in the AXD absorption spectrum with DDB-F60 as the initiator. D) Absorption spectra of regiorandom (RRa) P3HT conventionally doped (CD) with 6 mg $mL^{-1}$ $F_4TCNQ$ (dashed blue trace) and anion-exchange doped (AXD) with 6 mg $mL^{-1}$ $F_4TCNQ$ and 30 mg $mL^{-1}$ LiTFSI (solid blue trace), with the *Z* (2.0 eV) and *Z'* (3.7 eV) peaks labeled as well as the polaron transition peaks. E) Absorption spectra of RR P3HT doped with 3 mg $mL^{-1}$ $F_4TCNQ$ with 0, 3, 6, and 10 mg $mL^{-1}$ of LiTFSI plotted in black, red, purple, and blue, respectively. The $F_4TCNQ^{1-}$ peaks are highlighted at 1.4, 1.6, 1.8 and 3.0 eV, the neutral species is also pointed out at 3.2 eV. The P2 polaron transition peak and the bandgap are labeled including the *Z* and *Z'* peaks. F) Normalized absorption spectra of the *Z* peak plotted from 1.8 to 2.1 eV. The Z peak appears when the initiator dopant and salt are at least at a 1:1 molar ratio.

Typically, chemical doping results in integer charge transfer, ICT, in which an electron is entirely removed from the polymer backbone and transferred to the dopant. There are some extreme doping conditions, however, that result in placement of the dopant such that there is a high amount of orbital overlap so that electron density is shared between the polymer and the $F_4TCNQ$ dopant, known as a CTC. CTC formation between P3HT and $F_4TCNQ$ is characterized by a broad electronic absorption feature near 2.0 eV, a CN vibrational signature at ~2200 $cm^{-1}$, and a large broadening of the P1 peak to have significant absorption at 0.65 eV.[104] Although some CTCs are typically always present in $F_4TCNQ$-doped P3HT films, a significant amount of CTC formation is difficult to produce.[104,105] CTC formation usually requires extreme processing conditions such as high temperature annealing, using a branched-side-chain polymer to force dopants into the $\pi$-stacks, or using solvents that dissolve and recrystallize the polymer. It is possible that AX doping is another example of an extreme processing condition that encourages the formation of CTCs.

Another plausible assignment for the *Z* and *Z'* peaks is that incorporating LiTFSI into the dopant solution increases the doping potential of $F_4TCNQ$ enough to double dope P3HT. Studies have shown that $F_4TCNQ^-$ is capable of oxidizing the low ionization energy polymer, p($g_4$2T-TT).[106] The absorption spectra of a synthesized $2Li^+F_4TCNQ^{2-}$ salt shows an electronic feature at

3.7 eV and vibrational stretching modes at 2166 and 2135 $cm^{-1}$.[106] Others have indicated that $F_4TCNQ^{2-}$ in solution also may have absorption features in the visible region at 481 nm (2.57 eV) and 567 nm (2.19 eV).[107,108] It is possible that the additional oxidation potential obtained through AX doping allows for the removal of two electrons per dopant from the polymer backbone, giving rise to $F_4TCNQ^{2-}$ and thus the *Z* and *Z*' peaks.

Finally, studies have used $F_4TCNQ$ to dope silver nanoparticles (Ag NPs) in order to increase their electronic capabilities in devices.[99,100,109–111] One such study suggested that a Ag-$F_4TCNQ$ complex absorbs at 2.0 eV.[111] These studies show that forming a cationic complex with $F_4TCNQ$ that produces new electronic absorption features is possible, leading us to consider the Li-$F_4TCNQ$ complex as a possible assignment for the *Z* and *Z'* peaks. The purpose of this Chapter is to sort through these four possibilities using a series of experiments and quantum chemistry calculations.

## 3.2 Formation Conditions for the *Z* and *Z'* Peaks

To determine which of these four assignments, if any, makes the most sense for the *Z* and *Z'* peaks, we first explored whether or not the peaks appear regardless of the initiator dopant. We (and others)[101] have already shown that the *Z* and *Z'* peaks appear when using the common dopant/salt combination, $F_4TCNQ$ and LiTFSI (solid traces in **Figure 3.2a** and **3.2d**), thus we used a different initiator dopant to determine if the peaks are dependent upon $F_4TCNQ$ to form. **Figure 3.2c** shows the absorption spectra of P3HT both conventionally doped with dodecaborane (DDB) perfunctionalized with (2,3,4,5,6-pentafluorobenzyloxy) (DDB-F60) (blue curve) and AX-doped with DDB-F60 and LiTFSI (brown curve). We note that in the conventionally doped sample that a flat shelf at the P2 region most likely corresponds to a low doping regime in which the symmetry of the polymer is broken and allows for a P3 peak to appear,[84] which is not observed in the AX-

doped sample. We observe an increase in doping upon addition of LiTFSI, as evidenced by a higher intensity of both the P1 and P2 peaks, as well as an increased depletion of the bandgap absorption. Of note in the AX doped sample is the lack of either the *Z* or *Z'* peaks at 2.0 or 3.7 eV. This suggests that the electronic species that absorbs at 2.0 and 3.7 eV is associated with the $F_4$TCNQ dopant.

In the original Watanabe study, $F_4$TCNQ was used as the initiator dopant with 1-ethyl-3-methylimidazolium bis(trifluoromethylsulfonyl)imide (EMIM-TFSI) as the salt.[51] Using the same concentrations of dopant and salt as in **Figure 3.2a**, they do not observe any peaks at 2.0 or 3.7 eV.[51] This suggests that the combination of $F_4$TCNQ and LiTFSI is essential in forming this new electronic species.

Having confirmed the dopant/salt combination necessary to form *Z* and *Z'*, we wanted to understand if formation of the species responsible for these peaks has a concentration dependence on either the dopant or the salt. We first limited the dopant concentration (0.33 mg $mL^{-1}$ or 1.2 mM $F_4$TCNQ) while keeping the salt in excess (30 mg $mL^{-1}$ or 105 mM LiTFSI); the spectra of the resulting doped P3HT films are shown in **Figure 3.2b**. The conventionally doped sample (dashed teal trace) shows that the polymer is indeed doped with $F_4$TCNQ, as confirmed by the presence of $F_4$TCNQ anion absorption peaks, highlighted by asterisks. The AX doped sample (solid green trace) suggests the exchange process was successful because the $F_4TCNQ^-$ peaks disappear upon the addition of LiTFSI. Of note is the lack of *Z* and *Z'* peaks in this dopant-limited case, indicating that there are specific concentration conditions for the species responsible for these peaks to form.

We also tested the AX salt content to help understand the conditions under which the new species begins to form, testing three LiTFSI concentrations while keeping the amount of $F_4$TCNQ

constant. **Figure 3.2e** shows the absorption spectra of P3HT doped with 3 mg $mL^{-1}$ (10.9 mM) $F_4TCNQ$, and AXD with 3, 6, or 10 mg $mL^{-1}$ (10.5, 20.9, and 34.8 mM, respectively) of LiTFSI. **Figure 3.2f** shows a zoom-in of the *Z* peak region at 2.0 eV, with the spectra normalized at 1.8 eV for ease of comparison. When the dopant to salt ratio is less than 1:1 (black and red traces), the $F_4TCNQ$ anion peaks are still visible indicating that the salt must be at least over a 1:1 molar ratio to fully exchange out all the original dopant counterion. Meanwhile, only when the salt is in molar excess (purple and blue traces) is the *Z* peak formed. This indicates that formation of the electronic species that absorbs at 2.0 and 3.7 eV is contingent on having an excess concentration of both dopant and salt. Therefore, for the remainder of this study, we focus on doping P3HT with 6 mg $mL^{-1}$ (21.7 mM) $F_4TCNQ$ and 104.5 mM LiTFSI (as in **Figure 3.2a** and **3.2d**) as we have found these conditions keep both the dopant and salt in enough excess to consistently form the species responsible for the *Z* and *Z'* absorption peaks.

## 3.3 Using Absorption Spectroscopy to Eliminate P3 Transition

Now that we have established the peaks have specific formation conditions, we can use a combination of experimental and theoretical studies to explore the four possible assignments. First, the idea that the *Z* peak at 2.0 eV could be the P3 transition is not consistent with the fact that the peak also appears concomitantly with *Z',* at 3.7 eV. Another reason that the *Z* peak is likely not the P3 transition comes from the fact that we studied two P3HT regioregularities that have an 0.5 eV difference in their bandgaps. The bandgap difference would suggest that RR and RRa P3HT should have their doped P3 absorptions in different positions. Using the idea that the energy of P3 is the sum of the energies of the P1 and P2 transitions, the P3 band should be at 1.9 eV for RR P3HT and 2.1 eV in RRa P3HT. As shown in the absorption spectra in **Figure 3.2a** and **3.2d**, however, the *Z* and *Z'* peaks are in the exact same position for both regioregularities. Further

confirmation of this is shown in **Figure S.1** in which we compare the conventional and AX doping of dihexyl-substituted poly(3,4-proylenedioxythiophene) (PProDOT-$Hx_2$). Even in an entirely different polymer the *Z* and *Z*' peaks are in the exact same location, indicating that neither of these peaks are associated with the P3 transition.

## 3.4 Using FTIR Spectroscopy to Eliminate CTC Formation

Although UV-Vis spectroscopy offers substantial information about AX doping, we use FTIR as another tool to probe the exchange process. The vibrational stretching modes of the cyano groups on the $F_4$TCNQ dopant ($B_{1u}$ and $B_{2u}$) absorb in an otherwise spectrally quiet region. Although the $B_{1u}$ and $B_{2u}$ modes can shift depending on the degree of polaron localization and polymer crystallinity,[112] they are generally located at ~2190 $cm^{-1}$ and ~2170 $cm^{-1}$, respectively. **Figures 3.3a** and **3.3b** show the normalized CN stretching vibrations for both the conventionally and AX doped samples of RR and RRa P3HT. The conventionally doped samples (dashed traces) show $B_{1u}$ and $B_{2u}$ modes at 2188 and 2170 $cm^{-1}$ in RR P3HT, and 2190 and 2166 $cm^{-1}$ in RRa P3HT, confirming the presence of $F_4$TCNQ counterions in the polymer matrix. The AX doped samples (solid traces), however, show nitrile stretching peaks at 2200 and 2220 $cm^{-1}$ for both RR and RRa P3HT; these frequencies are too high to be associated with $F_4TCNQ^{1-}$. While the FTIR suggests a change of counterions has occurred, it also indicates that there is still $F_4$TCNQ left in the film

We can use the absorption data in **Figure 3.2a** and **3.2d** as well as the CN vibrational mode data in **Figure 3.3** to analyze the possibility of CTC formation. The CN stretching mode at 2200 $cm^{-1}$ shown in **Figure 3.3** does suggest some CTCs were formed during the AX process in both RR and RRa P3HT. However, we do not see the large broadening of the P1 peak, a key feature of

CTC formation. While the FTIR shows that some CTCs were formed, the coexistence of *Z* and *Z*' as well as the narrow P1 peaks shown in **Figures 3.2a** and **3.2d**, suggest that not enough CTCs were made to have a significant electronic absorption, thus we can conclude that the *Z* and *Z'* peaks are not associated with CTC formation.

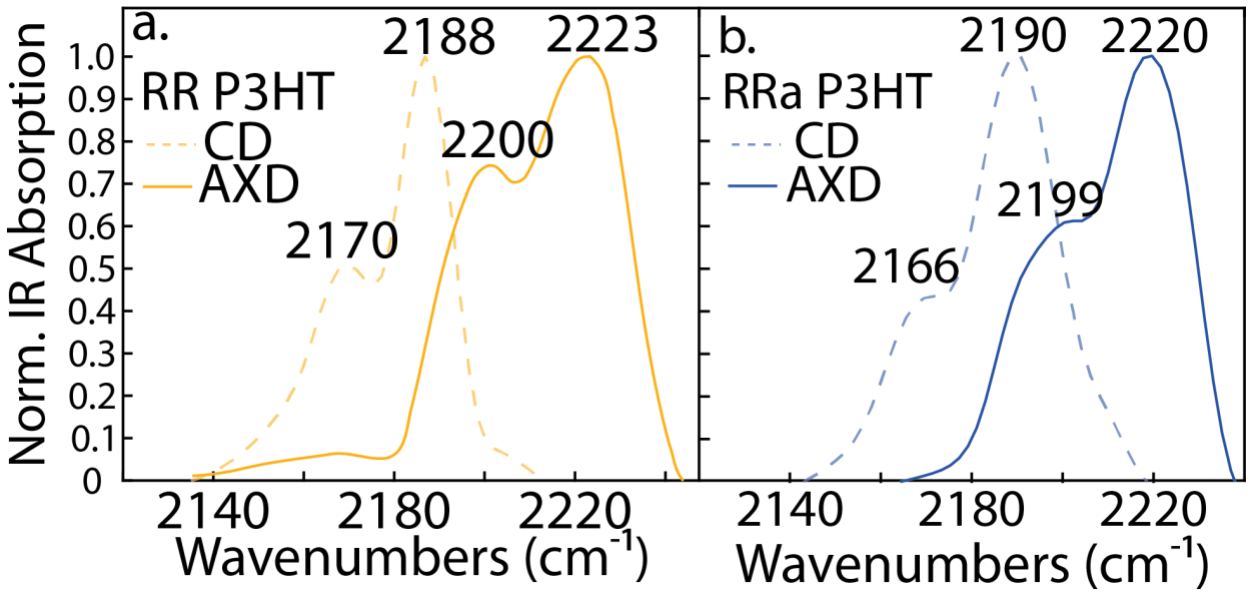


**Figure 3.3 Normalized CN Vibrational Modes in Doped P3HT**

Figure 3.3 $F_4TCNQ$ nitrile stretch vibrational spectra for a) RR and b) RRa P3HT conventionally doped (CD) with 6 mg $mL^{-1}$ $F_4TCNQ$ (dashed traces) and anion-exchange doped (AXD) with 6 mg $mL^{-1}$ $F_4TCNQ$ and 30 mg $mL^{-1}$ LiTFSI (solid traces). The CD samples show the $B_{1u}$ (~2190 $cm^{-1}$) and $B_{2u}$ (~2170 $cm^{-1}$) vibrational modes. The AXD samples show the possibility of CTCs (2200 $cm^{-1}$) and neutral $F_4TCNQ$ (2228 $cm^{-1}$).

## 3.5 Resonance Raman Spectroscopy Confirms Peaks Association with $F_4TCNQ$

We turn to Resonance Raman spectroscopy at two different excitation wavelengths to determine if the peaks are directly associated with the initiator dopant. We first perform Resonance Raman spectroscopy with 785 nm (1.58 eV) excitation, which is on resonance with the $F_4TCNQ^-$ electronic absorption. This means that we should expect to see a CN stretching vibration in the conventionally-doped samples but not in the AX-doped films where most of the counterions have

been exchanged away for $TFSI^-$. **Figure 3.4a** and **3.4b** show the 785 nm Resonance Raman data for both conventionally- and AX-doped RR and RRa P3HT, respectively. Indeed, the 785-nm Resonance Raman data shows a CN vibrational mode only for the conventionally doped samples (dashed traces). This verifies that the exchange process was successful and that there is not a significant amount of $F_4TCNQ^-$ left in the AX doped film. Therefore, we can conclude that the *Z* peak is not associated with the $F_4TCNQ$ anion.

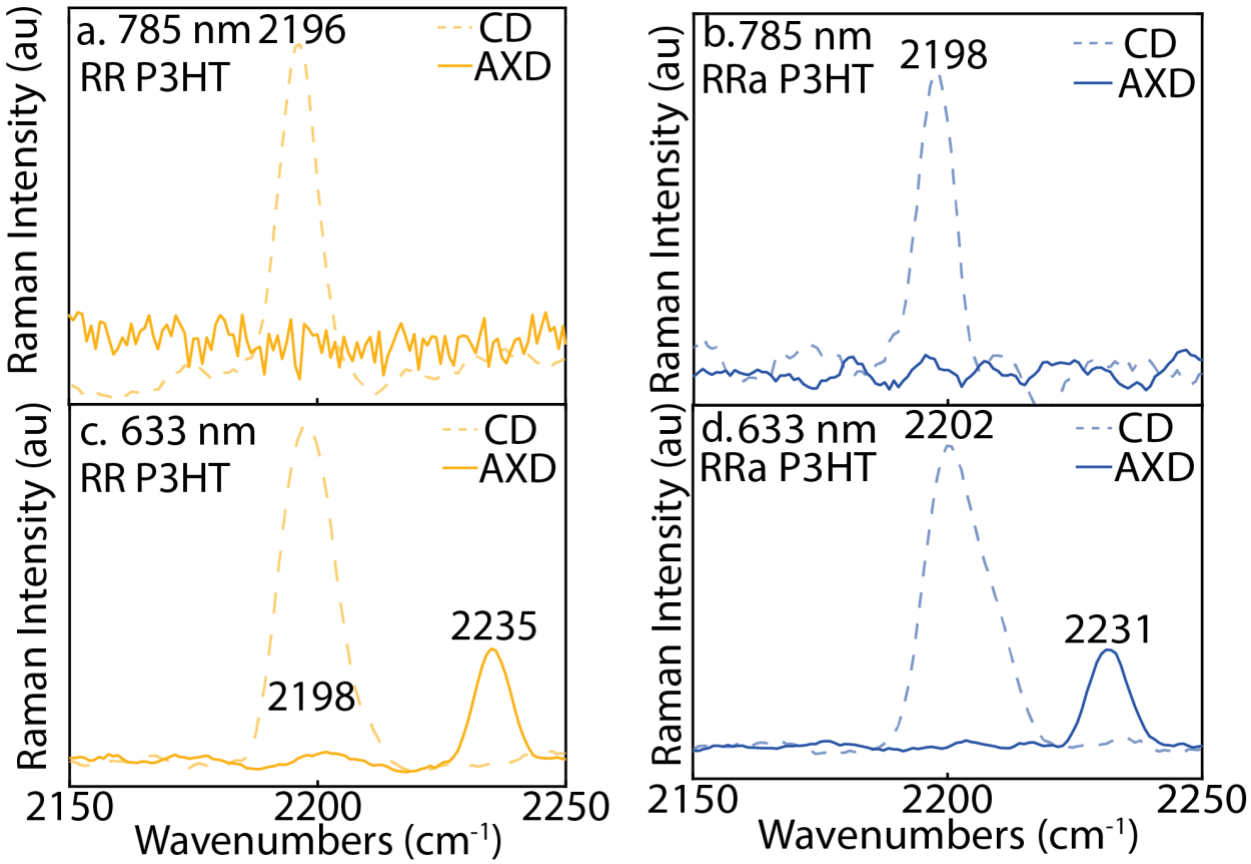


**Figure 3.4 Resonance Raman Spectroscopy of Doped RR and RRa P3HT**
Figure 3.4 785-nm excitation Resonance Raman Spectroscopy of a) RR and b) RRa P3HT conventionally doped (CD) with 6 mg $mL^{-1}$ $F_4TCNQ$ (dashed traces) and anion-exchange doped (AXD) with 6 mg $mL^{-1}$ $F_4TCNQ$ and 30 mg $mL^{-1}$ LiTFSI (solid traces). The CD samples show CN stretches at 2196 $cm^{-1}$ and 2198 $cm^{-1}$ for RR and RRa, respectively. The AXD samples show no detectable CN traces, indicating a successful counterion exchange. 633-nm excitation Resonance Raman Spectroscopy of c) RR and d) RRa P3HT. This probes the *Z* peak directly. In the CD samples both the RR and RRa P3HT have a peak at ~2200 $cm^{-1}$, corresponding to a CTC. The AXD films also have a CN stretch but it is shifted to 2235 and 2231 $cm^{-1}$ for RR and RRa P3HT, respectively. These peaks confirm that the *Z* peak is associated with $F_4TCNQ$.

We next turn to on-resonance Raman spectroscopy by exciting the *Z* peak directly at 633 nm (1.96 eV), shown in **Figure 3.4c** and **3.4d** for RR and RRa P3HT, respectively. The conventionally doped samples, shown in dashed traces, show peaks at 2198 and 2202 $cm^{-1}$ for the two polymer environments, corresponding to a CTC between the initial dopant and the host polymer. While we are directly probing the *Z* peak at this excitation wavelength, we are also probing CTCs; as discussed in the previous section, although a small number of CTCs are always formed, they are not the dominant feature and therefore not strongly evident in the absorption spectra.[104,105] In addition, the appearance of features around 2198 $cm^{-1}$ when exciting the conventionally doped samples using both 785-nm and 633-nm wavelengths, indicates that these vibrational features are standard for the $F_4$TCNQ-doped P3HT combination and not part of the species that forms the *Z* peak. The AX-doped films on the other hand, show CN vibrational modes at higher wavenumbers, 2235 and 2231 $cm^{-1}$ for RR and RRa P3HT, respectively. This indicates that while these peaks are indeed associated with the $F_4$TCNQ dopant, they are not a CTC. Out of the four theories presented as possible assignments for the *Z* and *Z'* peaks, we have shown that a P3 transition and a CTC assignment are inconsistent with the data presented. Thus, we theorize that the peaks are either associated with the $F_4TCNQ^{2-}$ or a Li-$F_4$TCNQ complex.

To explore if the *Z* and *Z'* peaks are associated with the dianion of the initiator dopant, we can compare the vibrational frequencies of $F_4TCNQ^{2-}$, which are known to appear at 2166 and 2136 $cm^{-1}$,[106–108] to the vibrational frequencies associated with the *Z* peak species. The data in **Figure 3.4c** and **3.4d** show that the vibrational frequencies associated with the *Z*-peak are nearly 100 wavenumbers blue-shifted from the $F_4TCNQ^{2-}$ modes. This suggests that the AX process is not conducive to double doping, therefore the *Z* and *Z'* peaks are not associated with $F_4TCNQ^{2-}$. We used quantum chemistry calculations to further confirm this theory due to the discrepancy in the

dianion's absorption features in the literature,[106–108] a detailed discussion can be found in the SI. The theoretical study reiterates the $F_4TCNQ^{2-}$ species does not produce the *Z* and *Z'* peaks.

## 3.6 Quantum Chemistry Calculations Suggest a Li-$F_4$TCNQ Assignment

Given that the vibrations of the $F_4$TCNQ-based species responsible for the *Z* and *Z'* peaks lie to higher frequency than the monoanion, this opens the possibility of having a lithium ion form a complex with $F_4TCNQ^-$ during the AX doping process; forming such a complex would render the $F_4$TCNQ anion insoluble, leaving it in the film. Studies using $F_4$TCNQ to dope Ag NPs show a Ag-$F_4$TCNQ complex absorbing at 2.0 eV, indicating not only that $F_4$TCNQ can form complexes with small cations, but also that the complex appears exactly where the *Z* peak absorbs.[111] To investigate this possibility, we performed quantum chemistry calculations on Li-$F_4$TCNQ complexes with multiple locations of the $Li^+$ in relation to $F_4$TCNQ, as discussed in the SI. Here, we focus on the configuration in which the $Li^+$ is placed "in line" with one of the cyano groups on the $F_4$TCNQ, a cartoon of which is shown in the inset of **Figure 3.5b**. The calculated vibrational frequencies and ground-state absorption spectrum of $[Li\text{-}F_4TCNQ]^0$ are plotted in **Figure 5a** and **5b**, respectively. The calculated IR frequencies of $F_4$TCNQ complexed with $Li^+$ (2239 $cm^{-1}$) are blue-shifted similar to the blue shift seen in the resonance Raman experiments when exciting the *Z* peak on resonance. The calculated electronic absorption for the Li-$F_4$TCNQ has peaks at exactly 2.0 and 3.7 eV, perfectly accounting for the peaks seen in experiment. Thus, we propose the *Z* and *Z'* peaks seen upon anion-exchange doping at high concentrations are associated with a Li-$F_4$TCNQ complex.

We also calculated the properties of $F_4$TCNQ complexed with tetrabutylammonium ($TBA^+$), , as shown in **Figure 3.5c** and **3.5d**, to test if any positively-charged ion could form a species that

would form the *Z* and *Z'* peaks. Unlike $Li^+$, the $TBA^+$ ion does not greatly affect the vibrations or the absorption transition of the dopant. This is due to the $TBA^+$ counterion's size, leaving its charge too far away from the $F_4TCNQ$ molecule to affect its electronic structure, while $Li^+$ has a much stronger interaction. We have shown through experimental and theoretical methods that a different initiator dopant and different cation-complexes do not form peaks at 2.0 and 3.7 eV. This further suggests the assignment of a Li-$F_4TCNQ$ complex to the *Z* and *Z'* peaks seen in the absorption spectra when AX-doped with LiTFSI.

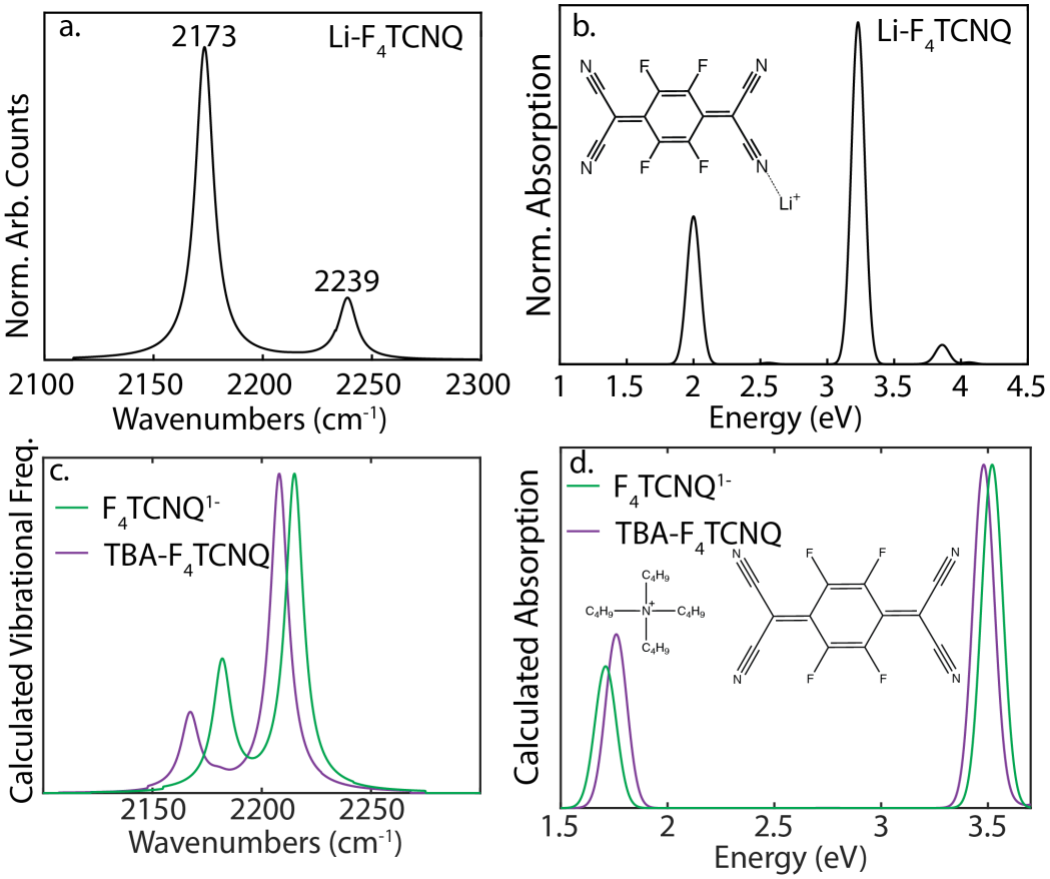


**Figure 3.5 Gaussian Calculations of $F_4TCNQ$ Complexed with $Li^+$ and $TBA^+$**
Figure 3.5. a. and b. show the calculated vibrational frequencies and excited state UV-Vis of Li-$F_4TCNQ$, respectively. The IR show that the CN stretching vibrations blue-shift compared to the dianion vibrational frequencies. The absorption spectrum shows three peaks at 2, 3.2, and 3.8 eV. These peaks correspond to the shifted $F_4TCNQ^{1-}$ peaks when forcing a complex to form between a $Li^+$ and the $F_4TCNQ$ dopant. Calculated c) vibrational frequencies and d) excited state UV-Vis of $F_4TCNQ^{1-}$ (green) and

tetrabutylammonium (TBA)-$F_4$TCNQ (purple). Both show that a large counterion does not affect the electronic structure of $F_4$TCNQ.

## 3.7 Conclusion

Using FTIR, Resonance Raman, and density functional theory, we assign the 2.0 and 3.7 eV absorption peaks that appear with anion-exchange doping to a Li-$F_4$TCNQ complex that forms during the exchange process as it encounters a nearby lithium ion. There is enough of the species to be seen spectroscopically, which indicates its relative importance electronically. By assigning these peaks, we are increasing the understanding of the anion-exchange process by highlighting the unintended products that are formed upon doping.

## 3.8 Supplemental Information for Chapter 3

### 3.8.1 *Materials*

The materials used in this study were: 93% RR P3HT and RRa P3HT which were both purchased from Reike Metals. The $F_4$TCNQ dopant and LiTFSI salt were used as purchased from Osilla LTD and Sigma-Aldrich, respectively. The additional polymer, Dihexyl-substituted poly(3,4-proylenedioxythiophene) (PProDOT-Hx2), was synthesized as described in ref [113]. The additional dopant, dodecaborane (DDB) perfunctionalized with (2,3,4,5,6-pentafluorobenzyloxy) (DDB-F60) (blue), was synthesized as described in ref [114].

### 3.8.2 *Film Preparation and Polymer Doping*

Glass substrates were cut into 1.3 x 1.3 cm pieces after which they were cleaned by a series of steps. All substrates were cleaned by sonicating them first for ten minutes in soapy water, and subsequently sonicated for five minutes in DI water, acetone, then isopropanol upon which they

are dried using nitrogen gas. The cleaned and dried substrates were then placed in a plasma etcher for 30 minutes before being transferred to a nitrogen glove box.

To study what happens during AX doping that produces the *Z* and *Z'* absorption peaks, we AX doped two different conjugated polymers: regioregular (RR) and regiorandom (RRa) P3HT. The chemical doping of RR and RRa P3HT is done by sequential processing (SqP), a method developed in our group that produces a superior film quality than blend casting[40,79]. SqP entails casting the polymer on a substrate first, followed by a second doping step using a solvent that swells but does not dissolve the polymer film. In the subsequent doping step, the initiator dopant, $F_4TCNQ$, and the inert salt, LiTFSI, are dissolved in *n*-butyl acetate (*n*-BA). 100 µL of the dopant solution is allowed to sit on top of the polymer film for 80 seconds, to allow for the doping and exchange process to unfold, before the excess solution is spun off.

### 3.8.3 *Experimental Methods*

Samples were prepared as discussed on glass substrates for UV-Visible absorption spectroscopy. UV-Vis was taken on a Jasco V-770 spectrophotometer at a scan speed of 400 nm/min from 250-3200 nm with a sampling interval of 1 nm and a slit width of 1 nm. In order to capture the entirety of the P1 peak, Fourier Transform Infrared spectroscopy (FTIR) was taken using the Agilent Technologies Cary 600 Series FTIR Spectrometer from 400-6000 $cm^{-1}$. Samples were cast onto KBr plates for FTIR. CN vibrational stretching modes were obtained from FTIR data and analyzed as described in ref [[112]]. Resonance Raman samples were cast onto silicon substrates that were prepared the same way as the glass substrates above. Resonance Raman using both 785-nm and 633-nm excitations were done by using 10% laser power with a continuous spectrum centered at 2190 $cm^{-1}$. Analysis for the Resonance Raman data were done in a similar fashion as the CN vibrational modes for the FTIR

3.8.4 *Dihexyl-substituted poly(3,4-proylenedioxythiophene) (PProDOT-Hx$_2$)*

Dihexyl-substituted poly(3,4-proylenedioxythiophene) (PProDOT-Hx$_2$) was used to further confirm P3 is an incorrect assignment as the *Z* and *Z'* peaks are in the exact same position as in RR and RRa P3HT despite the completely different polymer environment. **Figure S.3.1** shows the polymer conventionally doped (CvD) with 0.1 mg mL$^{-1}$ F$_4$TCNQ (pink trace) and anion-exchange doped (AXD) with 0.1 mg mL$^{-1}$ and 30 mg mL$^{-1}$ LiTFSI (green trace). The polymer bandgap, P2, F$_4$TCNQ$^{1-}$ and *Z* and *Z'* peaks are all labeled in the figure.

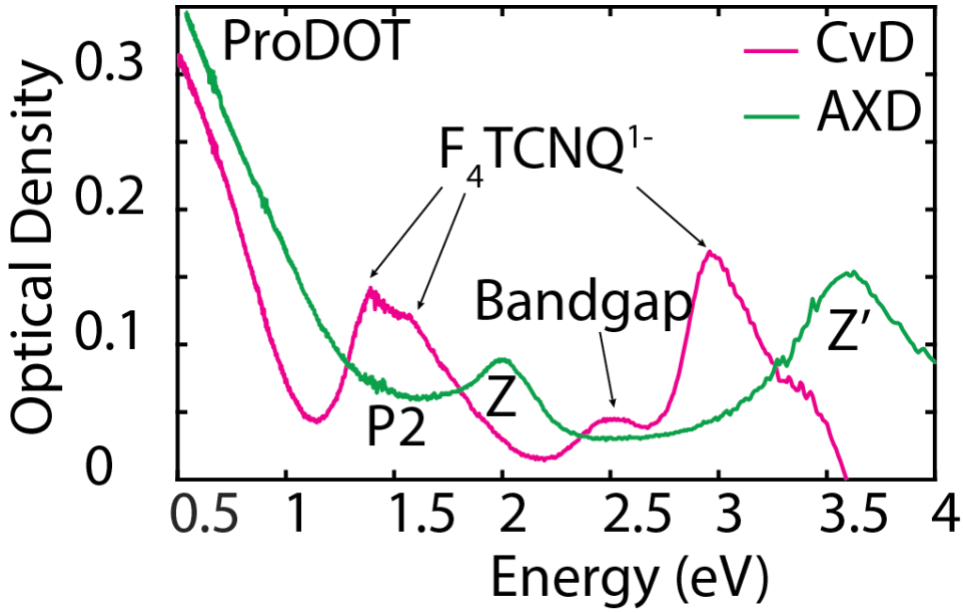


**Figure S.3.1 PProDOT-Hx$_2$ shows *Z* and *Z'* Peaks when Anion-Exchange Doped**
Figure S.3.1 Dihexyl-substituted poly(3,4-proylenedioxythiophene) (PProDOT-Hx$_2$) conventionally doped (CvD) with 0.1 mg mL$^{-1}$ of F$_4$TCNQ (pink trace) and anion-exchange doped (AXD) with 0.1 mg mL$^{-1}$ of F$_4$TCNQ and 30 mg mL$^{-1}$ LiTFSI (green trace). The F$_4$TCNQ$^{1-}$ peaks are labeled as well as the bandgap of PProDOT-Hx$_2$ which has been completely depleted upon AXD. The *Z* and *Z'* peaks are still at the exact same location in PProDOT-Hx$_2$ as they are in both RR and RRa P3HT.

3.8.5 *Calculations*

In ref [112], we performed calculations on bare F$_4$TCNQ to understand the role of electric field on the B$_{1u}$ and B$_{2u}$ stretching modes of the cyano groups on the molecule. In that study, we performed a systematic test to determine the basis set and level of theory used to balance the accuracy of the

calculations with computational expense. We found B3LYP level of theory with the 6-311++G basis set worked best for the purposes of that study. As such, all geometry optimizations, vibrational frequencies, and ground-state UV-Visible absorption spectra were calculated using B3LYP and TD-DFT when appropriate, with 6-311++G basis set. A more detailed discussion on the different levels of theory can be found in ref [112].

Different locations of $Li^+$ were used to calculate the ground-state absorption spectra of [Li-$F_4$TCNQ]$^0$. Included in the main text is the structure in which the $Li^+$ is oriented 'in-line' with a cyano group on $F_4$TCNQ. Figure S.3.2 shows the three other orientations we tested.

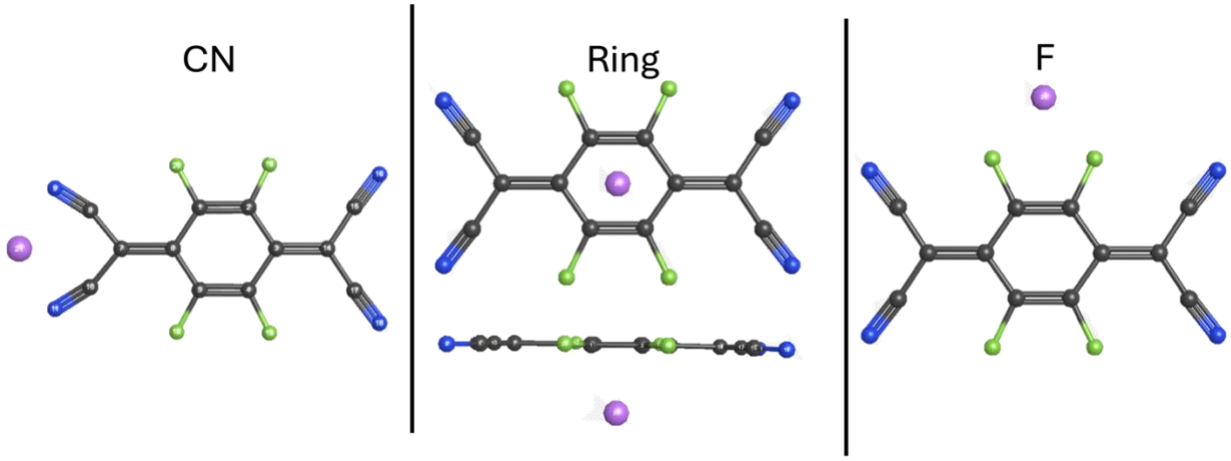


**Figure S.3.2 Various Orientations of $Li^+$ in respect to $F_4$TCNQ for [Li-$F_4$TCNQ]$^0$ Calculations**

We tested three other locations of $Li^+$ in relation to the $F_4$TCNQ molecule, the structures of which are shown in **Figure S.3.2**. We placed a Li in between two cyano groups (left panel), between the $\pi$-ring of the molecule (middle panel), and in between two fluorine atoms on $F_4$TCNQ (right panel). While we found that certain geometries are more energetically favorable in the gas-phase, we acknowledge that the relative energetics of what forms in a swollen polymer will be different. We chose to do the rest of the calculations on the 'in-line' geometry because when the

$Li^+$ was placed in between two CN groups, the $Li^+$ would slowly diffuse closer to one group than the other.

Before running calculations on $Li^+$ complexed $F_4TCNQ$, we obtained the calculated IR frequencies of $F_4TCNQ$ neutral, anion, and dianion as well as the ground-state absorption spectra of all three species. **Figure S.3.3a** shows the calculated IR frequencies of $F_4TCNQ^0$, $F_4TCNQ^{1-}$, $F_4TCNQ^{2-}$ with the corresponding maxima associated with each peak. The calculated trend agrees with experiment; the neutral species absorbs at the highest wavenumbers followed by the anion, and finally the dianion. While the calculated ground-state absorption spectra shown in **Figure S.3.3b**, does not capture the UV peaks correctly (experimentally, the anion absorbs at 3.0 eV while the neutral absorbs at 3.2 eV) it does correctly calculate that the dianion has the most blue-shifted absorption and captures the average peak of the $F_4TCNQ^{1-}$ vibrations in the visible region. The ground-state spectra show that the dianion species does not have a feature that absorbs in the visible region, thus we conclude that the *Z* and *Z*' peaks seen upon AX doping are not a result of double doping.

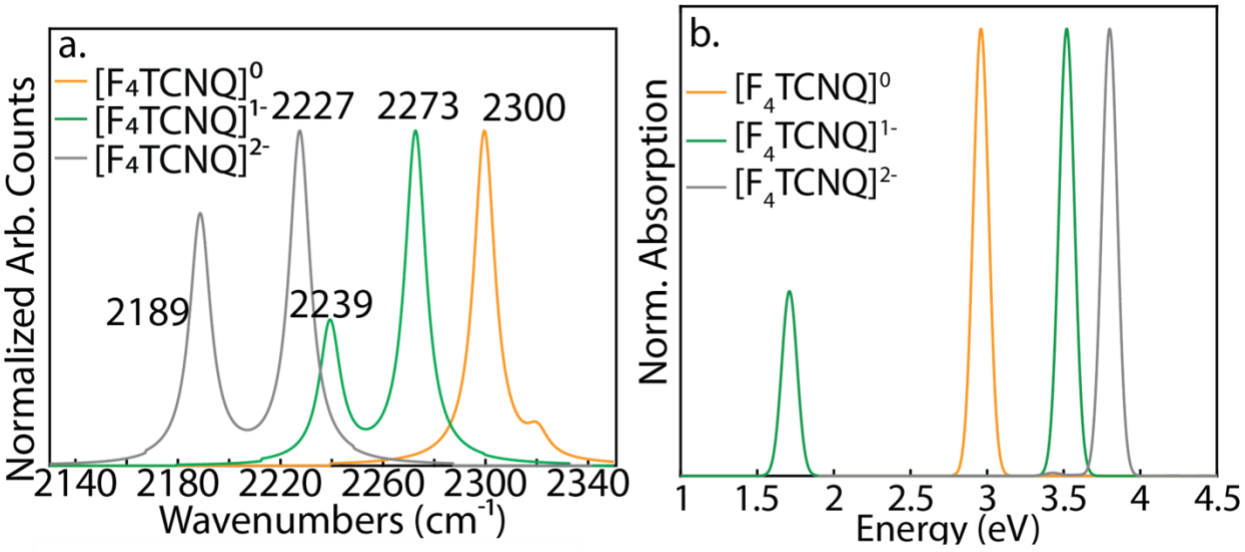


**Figure S.3.3 Calculated IR and Excited State UV-Vis of $F_4TCNQ^0$, $F_4TCNQ^{1-}$, and $F_4TCNQ^{2-}$**

Figure S.3.3 A) Shows the calculated vibrational frequencies and B) shows the calculated excited state UV-Vis of $F_4TCNQ^0$, $F_4TCNQ^{1-}$, $F_4TCNQ^{2-}$ in orange, green, and grey, respectively. The vibrational frequency and absorption spectra trends shown in the calculations match directly with the trends shown in experiment.

# Chapter 4

# Unfinished Business: The Nuances of Magic Blue Doping

## 4.1 Introduction

Many applications of doped conjugated polymers require a high conductivity which is achieved by optimizing three key parameters that are actively discussed in the literature: counterion size, polymer crystallinity, and the oxidation potential of the dopant. Larger counterions result in more delocalized polarons and therefore more highly mobile charge carriers. Crystalline polymers are more easily doped, increasing both carrier density and mobility. Dopants with larger oxidation potentials produce higher carrier densities. However, there is a give-and-take with tuning these parameters. Bipolarons, two spin-paired polarons, are readily formed by high oxidation potential dopants in amorphous sites, which leads to carriers with low mobility.[33] Crystalline regions are more resistant to solvent swelling; therefore, dopants can have a harder time intercalating into the film, producing lower carrier densities.[56] Meanwhile, doping with large counterions requires a polymer that is readily swellable to accommodate their size.[31,33]

Anion-exchange doping (as discussed in chapters 2 and 3) provides a way to tune and test the correlation of counterion size with electronic properties. One such study vapor doped poly[2,5-bis(3-tetradecylthiophen-2-yl)thieno[3,2-*b*]thiophene]-$C_{14}$ (PBTTT-$C_{14}$) with nitrosonium hexafluorophosphate ($NOPF_6$) that was subsequently anion-exchanged with either tetrafluoroborate ($BF_4^-$), tetracyanoborate ($TCB^-$), or tris(perfluoroalkyl)trifluorophosphate ($PCF^-$).[95] These four counterions have sizes varying from 5.2 Å to 8.2 Å in diameter. The authors conclude that although the strength of the local counterion-polaron interaction is indeed influenced

by the diameter of the counterion, the polymer structure and order play a more dominant role in determining electrical properties. Although this study included a fairly wide range of ion sizes, the compounding factor of different doping methods could have inadvertently affected the results.

The goal of this project is to isolate the doping mechanism of tris(4-bromophenyl)ammoniumyl hexachloroantimonate (magic blue, MB, whose structure shown in **Figure 1.3** in chapter 1 of this thesis). We tested multiple doping conditions to characterize the MB doping process and determine which sites are doped first: amorphous or crystalline. Soak duration, dopant concentration, and solvent dependence were tested and both detailed structural and electronic analyses were performed to understand how MB dopes the work-horse polymer, P3HT.

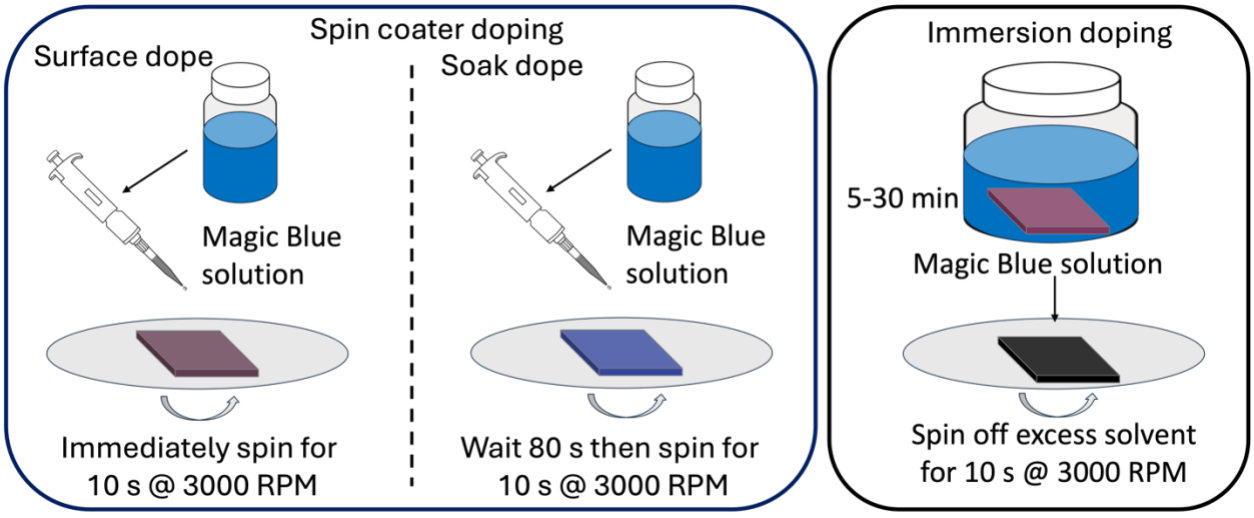


**Figure 4.1 Three Types of Doping with Magic Blue**
Figure 4.1 A schematic of the three different ways P3HT was doped using magic blue (MB). The pre-cast polymer is placed on a spin coater and 100 μL of dopant solution is pipetted on top of the film. The difference between the two types of doping are how long the dopant solution is allowed to sit on top of the film. In surface doping (left panel), the solution is spun off immediately. Soak doping, however, allows the 100 μL solution to sit on top of the film for up to 80 seconds (center panel). The right panel shows a schematic of immersion doping in which an undoped P3HT film is fully submerged in a MB solution in a sealed scintillation vial for up to 30 minutes. Once removed from the scintillation vial, the excess solvent is spun off the film using the same spinning conditions as for surface doping.

## 4.2 Methods

Two solvent systems were used to test MB doping: pure acetonitrile (MeCN) and a 3:1 *n*-butyl acetate (*n*-BA):MeCN mixture. MB is highly soluble in MeCN; however, it is not a good swelling solvent for P3HT; therefore, we used a mixture of *n*-BA and MeCN solution to promote swelling of polymer crystallites and thus enhance doping.

Three different doping techniques discussed in this chapter are: surface, soak, and immersion doping; **Figure 4.1** shows a schematic of all three. Surface and soak doping are closely related; in both methods, 100 μL of dopant solution is pipetted on top of a precast polymer film. When surface doping, we immediately spin off the solution, which does not give MB enough time to fully infiltrate the polymer matrix. Soak doping, on the other hand, allows the solution to sit on top of the film for up to 80 seconds before being spun off, removing some of the kinetic barrier to doping. Immersion doping entails fully submerging a polymer film in a sealed scintillation vial with at least 1.6 mL of dopant solution. Immersing the film allows for doping to occur on longer time scales, between 5 to 30 minutes.

## 4.3 Results and Discussion

This chapter focuses on understanding the doping mechanism of the powerful oxidant, MB. Multiple publications have used MB to dope CPs to extreme levels, obtaining conductivities of up to 3,000 $S \cdot cm^{-1}$ on aligned polymer films.[32] Some theorize that MB can achieve such high conductivities due to phase-selective doping. Phase-selective doping is a process in which a polaron is created in an amorphous region that is able to hop to crystalline sites while the counterion remains in the original amorphous pocket. This has been the proposed doping mechanism of MB due to the lack of structural change seen in X-Ray Diffraction upon intercalation

into the polymer matrix.[32] When we repeated these experiments on standard isotropic films, however, we found that, like all other dopants, MB does affect the crystal structure of P3HT. As such, we theorized that MB oxidizes the amorphous regions in the polymer first and then intercalates into the crystalline sites upon further doping.

To test our theory, we used MB to dope two different crystallinities of P3HT: 97% RR P3HT and RRa P3HT. **Figure 4.2** shows the absorption spectra of the two polymers, surface and soak doped with 0.5 mg $mL^{-1}$ of MB in a 3:1 *n*-BA:MeCN solution. The undoped spectrum (solid black trace) of a 97% RR P3HT film, shown in **Figure 4.2a**, has a large absorption peak at ~2.3 eV and has vibrational features that are indicative of the high degree of order in the polymer. As the film is surface doped (green, dashed trace) by MB, the bandgap absorption begins to deplete as the electrons are removed from the valence band. Based on the bandgap depletion, the polymer is about 30% oxidized, suggesting a relatively low doping efficiency when surface doping. We also soak-doped 97% RR P3HT, allowing the dopant solution to sit on top of the polymer film for 80 seconds before spinning off the excess. In this case, the bandgap absorption is almost completely depleted, accompanied by a significant increase in the polaron P1 peak absorption intensity, indicating a large increase in doping.

**Figure 4.2b** shows the absorption spectra of undoped RRa P3HT (grey trace), surface doped (dashed blue trace) with MB, and soak doped (solid blue trace) with MB. The general trends are similar as seen with 97% RR P3HT, although with lower overall doping levels because, as discussed in chapter 2, RRa P3HT is more difficult to oxidize. Surface doping RRa P3HT barely dopes the polymer, as evidenced by only a slight depletion of the bandgap absorption at ~2.7 eV, while soak doping completely depletes the bandgap absorption and significantly increases the P1 peak intensity. By allowing MB more time to intercalate into the polymer matrix, we observe a

significant increase in doping, indicating that MB's doping mechanism is kinetically driven.

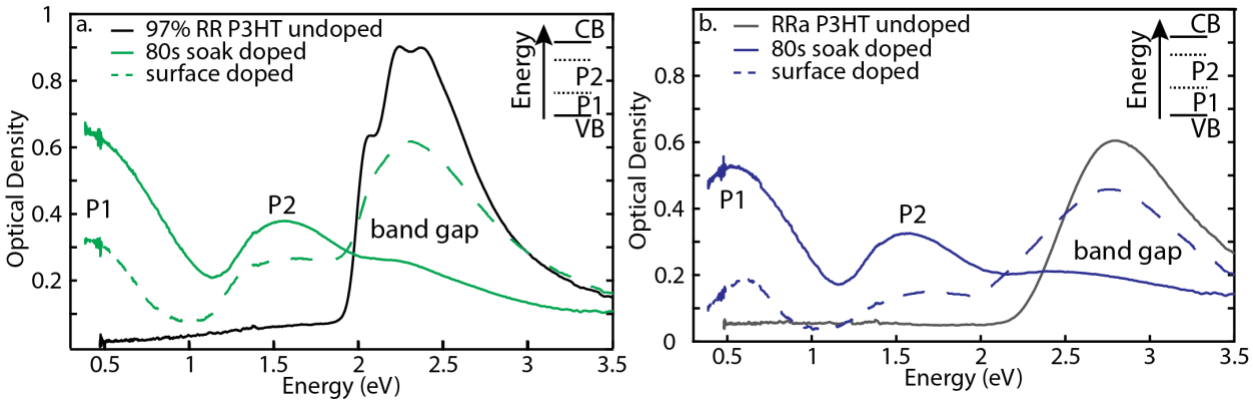


**Figure 4.2 Surface versus Soak MB Doping of 97% RR P3HT and RRa P3HT**
Figure 4.2 Absorption spectra for a) 97% RR P3HT and b) RRa P3HT surface doped (dashed traces) and soak doped for 80 seconds (solid traces) with 0.5 mg $mL^{-1}$ of MB in a 3:1 *n*-BA:MeCN solution. A) The dashed green trace is the absorption spectrum of 97% RR P3HT surface doped while the solid green trace is soak doped for 80 seconds. Both doping types show a P1 peak that have a maximum absorption red of 0.5 eV, and a P2 at ~1.6 eV. A very similar trend is seen in b) for RRa P3HT. As the polymer is doped, the bandgap depletes as a direct result of electrons occupying the P1 and P2 transitions. While the P2 is in approximately the same location as in the 97% RR P3HT, RRa's maximum P1 peak is located blue of 0.5 eV.

## 4.3.1 Soak-Timing Tests

In order to understand the kinetic process of MB doping, we did an extensive timing test in which we allowed the dopant solution to sit on top of the film for 5-second intervals from 0 to 45 seconds. **Figure 4.3a** shows that as we increased the soaking time, more MB intercalated into the film, as indicated by a nearly complete depletion of the bandgap absorption by 45 seconds that is accompanied by a P1 absorption intensity increase. To explore how the P2 transition changed as the soaking time increased, **Figure 4.3b** shows absorption spectra normalized at 0.4 eV, allowing us to make two observations: 1) the blue-edge of the P1 peak broadens and 2) the P2 peak decreases as the soaking time increases, both of which are signs of bipolaron formation. Bipolarons form when there is a significant amount of doping, allowing two polarons to become spin-paired, which further suggests MB intercalation into the crystalline sites.

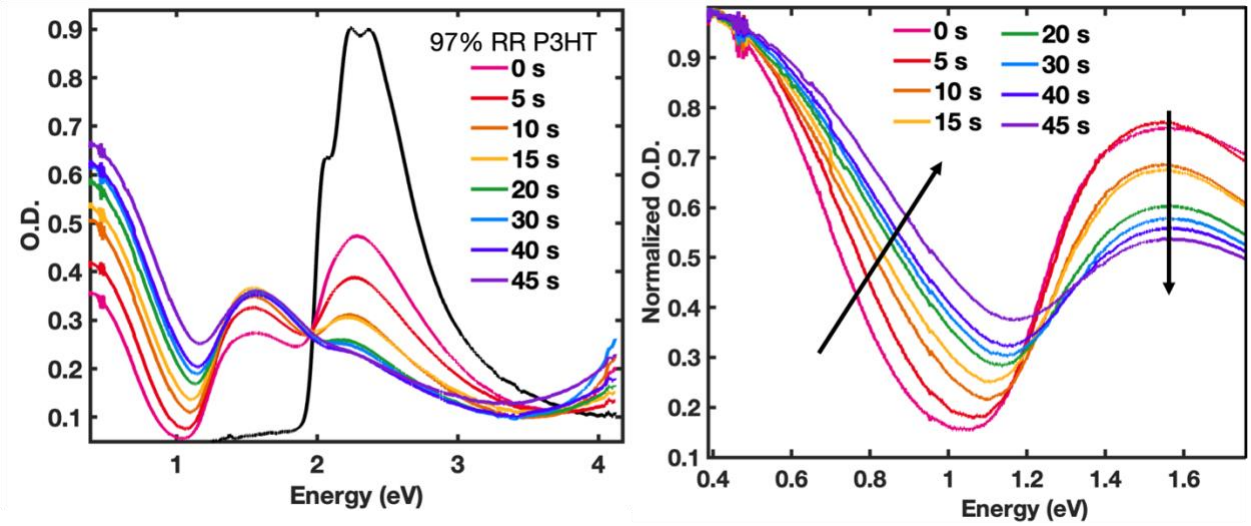


**Figure 4.3 Absorption Spectroscopy of Soak Timing Tests on MB-Doped 97% RR P3HT**
Figure 4.3. Absorption spectra of 97% RR P3HT doped with 0.5 mg $mL^{-1}$ of MB dissolved in a 3:1 *n*-BA:MeCN solvent combination. A) Unnormalized absorption spectra to highlight the doping efficiency as time increases as evidenced by a continuous increase of the P1 absorption intensity and the continuous bleach of the bandgap absorption. B) Normalized absorption spectra to show the broadening of the P1 transition and the decrease of the P2 absorption peak as time increases, an indication of bipolaron formation.

To see how the conductivity, mobility, and carrier density respond as we form bipolarons, we performed electrical measurements while increasing the MB-doping soak time. Conductivity can be enhanced by either increasing the carrier density, the carrier mobility, or both. The black trace in **Figure 4.4a** shows that the conductivity continues to increase with soaking time followed by a plateau after 30 seconds of soaking. In order to understand the plateau, we used Hall effect measurements to determine how the carrier mobility (**Figure 4.4a**, red trace) and carrier density (**Figure 4.4b**) change as a function of MB soaking time. Before 30 seconds, both mobility and carrier density increase with soaking time, explaining the steady rise in conductivity. After 30 seconds of soaking time, however, the carrier mobility experiences a significant drop while the carrier density continues to increase. The sharp drop in mobility is a result of charge carriers becoming paired and therefore trapped, while a continuous increase in carrier density indicates that polarons are still being formed; this increased carrier density is confirmed spectroscopically by the continuous depletion of the polymer bandgap absorption. Thus, our preliminary timing tests

show that when given enough time to intercalate into the film, MB is capable of forming bipolarons in a crystalline polymer due to its high oxidation potential.

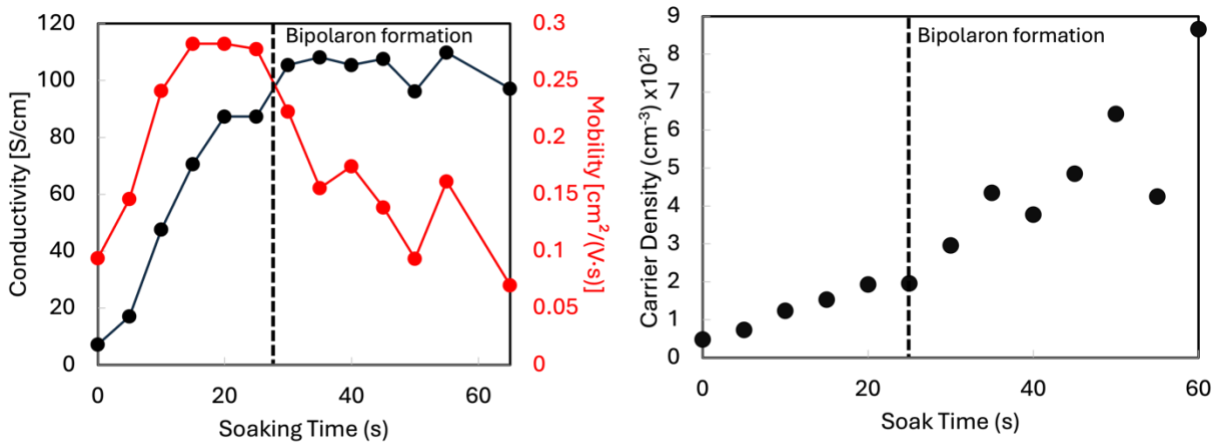


**Figure 4.4 Electrical Measurements of Soak Timing Tests on MB-Doped 97% RR P3HT**
Figure 4.4 Shows electrical measurements of the 97% RR P3HT soak doped with magic blue as a function of time. A) Shows the conductivity in black, and the carrier mobility in red. The black dashed line at 25 seconds highlights the point at which we believe bipolarons are forming. B) Carrier density is plotted with the same 25-s time highlighted.

## 4.3.2 Concentration Dependence of MB Doping

Beyond the kinetic component addressed by the soak-timing experiments, we also wanted to test the concentration dependence of MB doping. **Figure 4.5** shows the absorption spectroscopy of 97% RR P3HT soak doped for 80 seconds with varying concentrations of MB in a 3:1 *n*-BA:MeCN mixture. As we increase the concentration of MB, we observe an increase in doping indicated by a continuous depletion of the bandgap absorption as well as an increase of the P1 peak intensity. The spectra suggest that as the concentration reaches 1 mg $mL^{-1}$ of MB, bipolarons are being formed, which is confirmed using electrical measurements. **Table 4.1** shows the mobility, carrier density, and conductivity values for the three highest MB concentrations. As we increase dopant concentration, the conductivity increases until the point at which bipolarons begin to form.

Then, the conductivity decreases from 15 S $cm^{-1}$ when doping with 0.5 mg $mL^{-1}$, to 11 S $cm^{-1}$ with 1 mg $mL^{-1}$, despite a nearly order of magnitude enhancement of the carrier density. This conductivity decrease is due to a dramatic loss in carrier mobility. The oxidation potential of MB is high enough to form bipolarons in a crystalline polymer despite being easier to form in amorphous environments, which suggests a structural change upon MB intercalation.

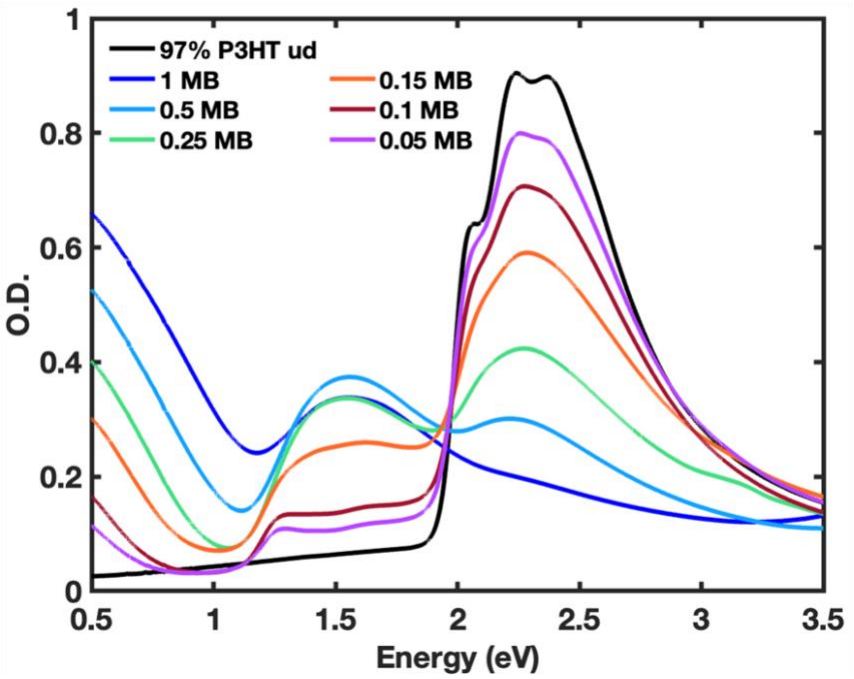


**Figure 4.5 Absorption Spectra of the Concentration Dependence of MB Doped 97% RR P3HT**
Figure 4.5 Absorption spectra of 97% RR P3HT doped with varying concentrations of MB in 3:1 *n*-BA:MeCN solution. As the concentration of MB increases, doping continues to increase as evidenced by the increased bandgap depletion and the P1 peak intensity increase. However, we note that the P2 absorption band decreases in intensity as the concentration is increased from 0.5 mg $mL^{-1}$ MB to 1 mg $mL^{-1}$ MB, an indication of bipolaron formation.

**Table 4.1 Electrical Measurements of the Concentration Dependence of MB Doped 97% RR P3HT**
Table 4.1 Shows the mobility, carrier density, and conductivity values obtained by Hall effect measurements. The data shows as dopant concentration increases, the carrier density increases, consistent with spectroscopy. However, the mobility drops significantly at 1 mg/mL MB, due to bipolaron formation.

| MB Concentration (mg· $mL^{-1}$) | Mobility ($cm^2$· (V· s)$^{-1}$) | Carrier Density ($cm^{-3}$) | Conductivity (S· $cm^{-1}$) |
|---|---|---|---|
| **0.25** | 0.12 | $8.5 \cdot 10^{19}$ | 1.6 |
| **0.5** | 0.24 | $3.9 \cdot 10^{20}$ | 15 |

| | | | |
|---|---|---|---|
| **1** | 0.03 | $2.2 \cdot 10^{21}$ | 11 |

### 4.3.3 Structural Effects on MB Doping

Current unpublished studies in our group suggest that bipolarons form more readily in amorphous polymer regions. Despite 97% RR P3HT being highly crystalline, MB is able to form these spin-paired species, suggesting a structural change to accommodate the additional carriers. With this in mind, we turn to Grazing Incidence Wide Angle X-ray Scattering (GIWAXS) to understand how MB affects the crystal lattice of P3HT.

**Figure 4.6** shows directional 1D integrations of GIWAXS diffractograms of MB-doped 97% RR P3HT. The out-of-plane integration can probe the distance between the side-chains, or the lamellar region, as shown in **Figure 4.6a**. The main figure highlights the (100) peak while the inset shows a closer look at the (200) and (300) overtones. First, we note that the (100) peak changes in intensity with dopant concentration: at low dopant concentrations (red, orange, yellow traces), the (100) peak increases in intensity but does not shift from the undoped sample (black trace, hidden behind the green trace), indicative of an increase in order. When doping with 0.2 mg $mL^{-1}$ of MB (light blue trace) however, the peak begins to shift to lower *q* which is correlated with a larger *d*-spacing; this indicates that the side-chains are now spaced further apart to accommodate the counterion. We observe a continuous shift to lower *q* as we continue to increase MB concentration, which is accompanied by a decrease in the (100) peak intensity. These two changes in the GIWAXS is a clear indication that the counterion has not only infiltrated the crystalline region, causing a phase transition, but has highly disrupted the crystal structure as well. We have seen this type of disruption of crystal lattices upon bipolaron formation in previous studies and it is because bipolarons are preferably formed in amorphous regions.[54]

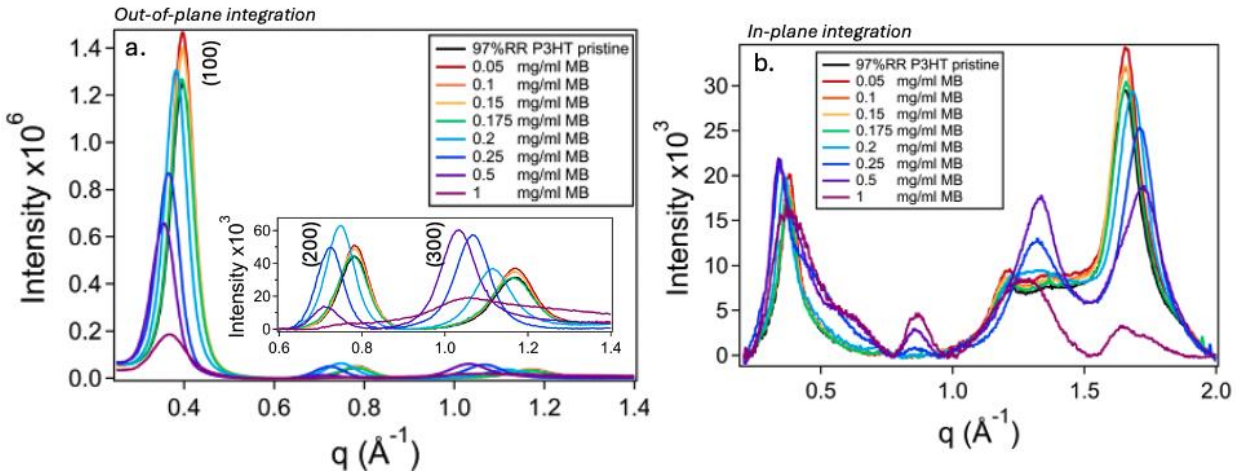


**Figure 4.6 1D GIWAXS of 97% RR P3HT Doped with Varying Concentrations of MB**
Figure 4.6. 1D integrations of GIWAXS samples. A) shows the out-of-plane integrations of 97% RR P3HT soak doped for 80 seconds with varying concentrations of MB in a 3:1 *n*-BA:MeCN solvent solution. The inset shows a closer look at the (h00) overtones. B) shows in-plane integrations, which inform us about the π-stacking distances.

## 4.4 Conclusions and Future Directions

Magic blue is a powerful oxidant with a high doping efficiency. We have shown that doping conjugated polymers with MB has a kinetic component, as shown via the dependence of doping level with soaking time. We have also shown that MB is capable of forming bipolarons in a crystalline polymer due to its disruption of the crystal structure upon dopant intercalation. The structural data obtained in this study shows that at low doping concentrations of MB, amorphous regions are doped first due to a kinetic limitation of the doping process. As the MB concentration increases, the crystalline sites are doped until bipolarons are formed and the polymer's ordered regions are disrupted to accommodate the new electronic species. Thus, we conclude that MB dopes amorphous regions first, followed by crystalline regions as doping continues.

This chapter highlights preliminary exploration on the doping mechanism of MB. To build a coherent story, I detail three additional studies that I believe would be informative. First, doping aligned P3HT films with MB and obtaining structural analysis will inform us more clearly if the

dopant intercalates into the ordered or disordered regions. It would also serve as a comparison to previous studies in the literature that have concluded the MB counterion is located only in the amorphous sites in aligned-P3HT samples.[32]

Next, comparing the electronic characteristics between P3HT films doped with MB and DDB-$F_{72}$ would be helpful as they have similar oxidation potentials and neither counterion is flat like $F_4$TCNQ, thus the effects of dopant size and shape can be further studied. By matching carrier densities of MB and DDB-$F_{72}$ doped P3HT, we can focus on the mobility differences between the two dopants. We have shown that carriers created by DDB-$F_{72}$ doping have a high mobility due to the low coulombic interaction between counterion and polaron.[31,33] If the mobility of carriers in MB-doped P3HT at the same doping level is higher, it would suggest that the counterions are indeed situated farther away from the polarons than what is seen when doping with DDB-$F_{72}$, despite the smaller size of the counterion.

Finally, studies have reported higher electrical conductivities when anion-exchanging with MB as the initiator dopant rather than with $F_4$TCNQ as the initiator.[115] Understanding this phenomenon would help pinpoint the location of the MB counterion by exchanging it with the same salt anion in both samples. By normalizing to the carrier density, we can explore the mobility differences between MB and $F_4$TCNQ anion-exchanged films to explore why there is such a high conductivity difference.

## 4.5 Acknowledgements

This work was done in collaboration with Amanda Nguyen, an undergraduate student in the Schwartz lab. Amanda has done amazing work in our group, picking up the science quickly. My favorite part of this project was getting to be her mentor. Amanda is an incredibly gifted student

who will do wonderful things as a graduate student at Northwestern University. The structural data was obtained by Nesibe Akmansen-Kalayci from the Tolbert lab who has been an incredible addition to the collaboration. This work will be continued by Abigail Slimp, a joint graduate student in the Schwartz and Tolbert labs.

# Chapter 5

# Theoretical Calculations of Tungsten Tetraboride ($WB_4$)

## 5.1 Introduction

Transition metal borides have many useful properties rooted in metal-boron bonds. For example, it has been discovered that rhenium diboride ($ReB_2$) has superhard properties.[116] The hardness of a material is described using the Vickers Hardness scale as shown in **Figure 5.1**. A material is considered superhard if it has a Vickers Hardness above 40 GPa. While $ReB_2$'s measured hardness is 30 GPa, well under the threshold of superhard, at certain crystallographic orientations, it can scratch a diamond's surface.[116] Using theoretical calculations, we can understand how the bonding between the transition metal and the boron atoms influence the material properties.

Recently, experimentalists have discovered cheaper variations of $ReB_2$ including tungsten tetraboride ($WB_4$)[117] and tungsten diboride ($WB_2$)[116,118], both of which have Vickers Hardness values above 40 GPa. Moreover, when either material is doped through atomic substitution, the hardness changes, but the effect of dopant placements in the lattice and the electronic origin of hardening, remains unclear. This chapter highlights my work on developing an accurate and cost-effective theoretical model to understand the intrinsic/extrinsic hardening effects of doped tungsten borides.

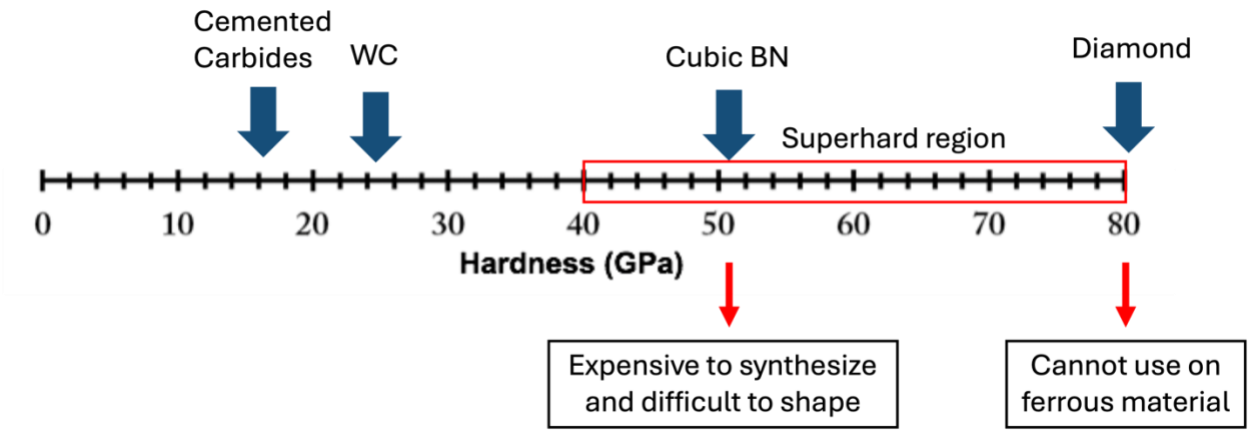


**Figure 5.1 Vickers Hardness Scale**
Figure 5.1 Diagram of Vickers Hardness scale with examples of superhard materials

## 5.2 Theoretical Methods

Tungsten boride structures were optimized with Density Functional Theory (DFT) using the Vienna Ab-initio Simulation Package.[119–122] Plane-augmented-wage pseudopotentials for all atoms were used with the Perdew-Burke-Enzerhof exchange-correlation function.[123,124] This method produces lattice parameters commensurate with the experimentally obtained structures. The theoretical structures were optimized as 2x2x2 supercells containing 130 atoms, with a Gamma centered k-point grid.

Upon completion of the geometry optimization, I used a few different methods to understand the bonding of the materials including Electron Localization Functions (ELF)[125], Bader charges[126], and LOBSTER calculations.[127–130] ELF calculations give a spatial representation of the electron density within a covalent bond. Bader charges give an approximation of the total electronic charge on an atom. LOBSTER is a software that is used to obtain the integrated crystal orbital Hamilton population (ICOHP), which gives a relative value for the strength of each bond.

ICOHP is particularly useful in this study as it helps partition long range interactions between atoms. This partitioning then gives bonding and anti-bonding interactions that we integrate over energy. This integrated population determines the totality of bonding between any pair of atoms. Thus, ICOHP is applicable in this study as metal-boron, boron-boron, and transition metals are unpredictable and therefore make their implicated participation in hardness complicated.

ELF and Bader charges were obtained from VASP with specific flags from the INCAR files. The Bulk and Shear moduli were obtained from electric tensors after running elastic calculations using VASP. The elastic tensors were extracted from OUTCAR files using an in-house code written by my colleagues, Kirill Shumilov and Hang Yin.

## 5.3 Results and Discussion

### 5.3.1 Theoretical Structure Elucidation

The first step in understanding a material's bonding is elucidating its structure. The initial structure, shown in **Figure 5.2**, was optimized from an experimentally obtained crystallographic information file.[61] There are three different atomic sites in the $WB_4$ unit cell: a fully occupied boron site, a fully occupied tungsten site, and a partial occupancy site. The fully occupied positions are completely shaded in Figure 2 and represent where a B or W is always found. The fully occupied B sites form a hexagonal sheet which prove to be vital in the hardening effects of the material. A W atom is found in the partial occupancy site 66% of the time while a $B_3$-cluster is found in the site 33% of the time, this is represented by a semi-shaded atom in **Figure 5.2**.

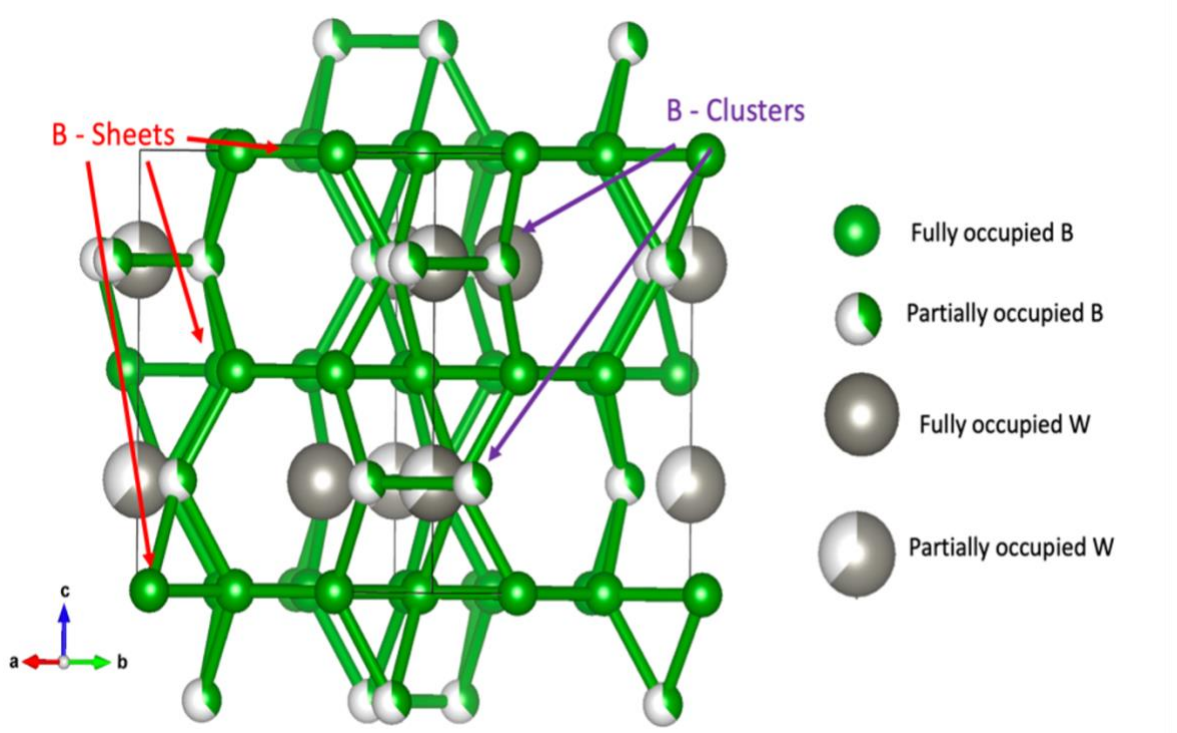


**Figure 5.2 Unit Cell of $WB_4$**
A unit cell of tungsten tetraboride ($WB_4$) obtained from experimental methods. The legend to the right details each atom. The partially occupied atoms are filled based on how often they appear in the structure. Fully occupied Bs are labeled as those in B-sheet, three of which are highlighted by a red arrow. Partially occupied Bs, highlighted by purple arrows, are known as those in a $B_3$-cluster.

To confirm the structure of pure $WB_4$, I tested the $B_3$ partial occupancy locations in respect to another $B_3$-cluster. There are four different positions two $B_3$ clusters can occupy depending on their distance and orientation to each other. **Table 5.1** shows the relaxed energy values for the optimized geometries of the four positions, labeled in terms of distance between two $B_3$-clusters. The relaxed geometries show that the most energetically favorable positions are when the $B_3$-clusters are located 3.2 or 6.4 Å apart. **Figure 5.3a** and **5.3b** show the two energetically favorable structures with the clusters highlighted in red. When the $B_3$-clusters are 3.2 Å apart (**Figure 5.3a**), they form a 'cage-like' bond with the B-sheet between the clusters. Meanwhile, when they are 6.4 Å apart (**Figure 5.3b**) they instead form an 'hour-glass-like' structure with the B-sheets above and below. All calculations following these preliminary geometry optimizations are done on both

structures to test the hypothesis that the clusters are forced apart by the dopants which affects the bonding and therefore hardness of the material.

**Table 5.1 Relaxed Energy Values for $B_3$-clusters and Average ICOHP Bond Strengths in Pure $WB_4$**
Normalized relaxed energy values for the optimized structure of $WB_4$ with two $B_3$-clusters at varying distances. We observed that a $B_3$-cluster that is 6.4 Å apart is the most energetically favorable geometry followed closely by clusters that are 3.2 Å apart, both of which were further studied.

| Distance between two $B_3$-clusters (Å) | Normalized relaxed energy value (eV) | Average ICOHP bond strength (eV) |
|---|---|---|
| 3.2 | -8.0 | -4.114 |
| 5.2 | 0 | N/A |
| 6.4 | -9.3 | -4.095 |
| 8.2 | -0.032 | N/A |

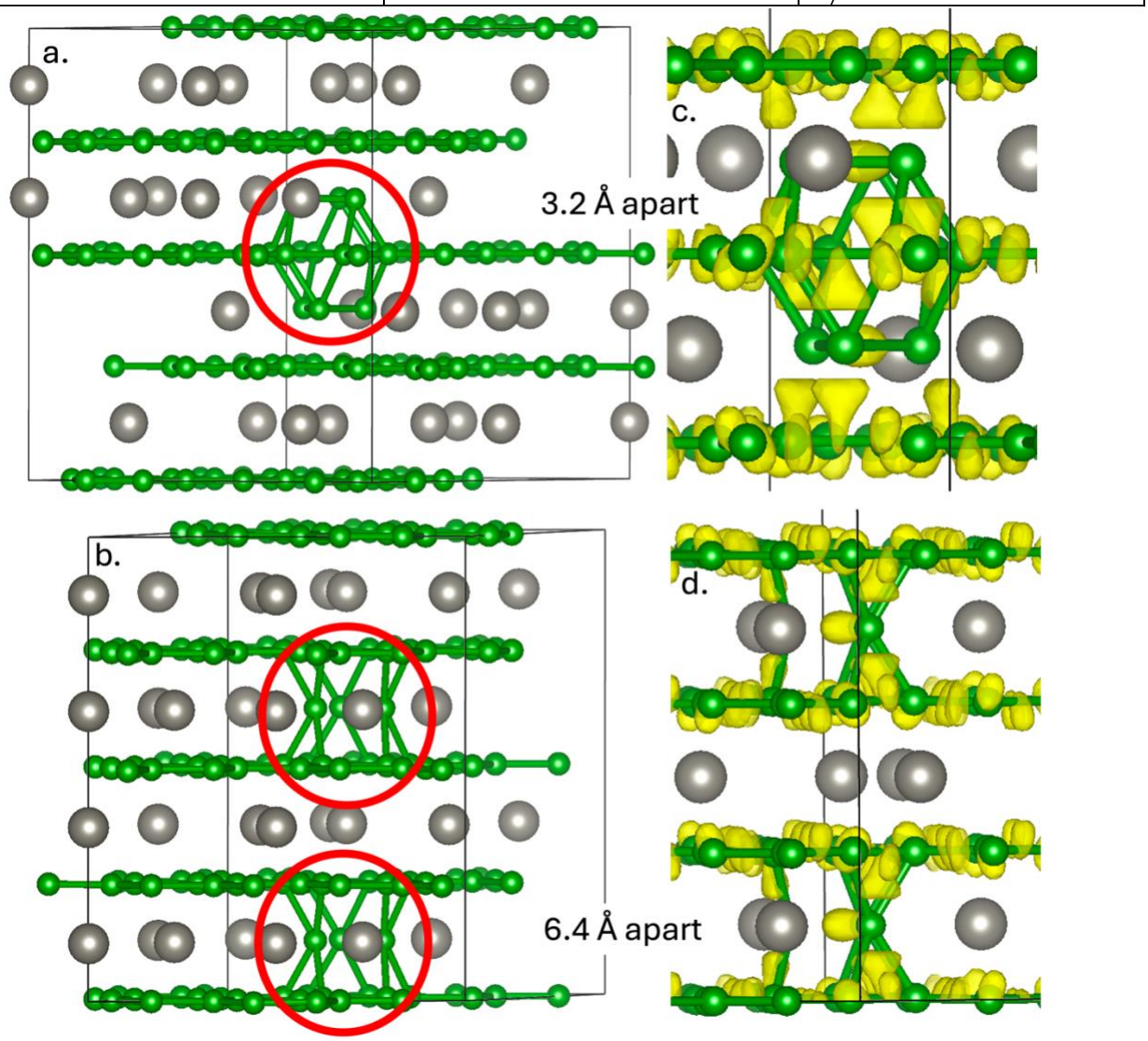


**Figure 5.3 Optimized $B_3$-cluster Structures 3.2 and 6.4 Å Apart and their ELF Analysis**

Geometry optimizations of a 2x2x2 supercell of $WB_4$ with two B3-clusters at two different distances: a) 3.2 Å and b) 6.4 Å apart. The cage or hourglass they create with the B-sheets are highlighted in red. The electron localization functions (ELF), or the electron density (in yellow), are shown pure $WB_4$ with two $B_3$-clusters c) 3.2 Å and d) 6.4 Å apart.

### 5.3.2 Bonding Analysis of the $B_3$-Clusters

While we know $WB_4$ is superhard, we cannot experimentally determine if the hardness is due to extrinsic or intrinsic effects. Therefore, we ran ELF and ICOHP calculations to understand the bonding of the $B_3$-clusters to determine what role they play in the hardening of pure $WB_4$. When used together, ELF and ICOHP analysis give an approximate electronic picture of the material. The ELF analysis, shown in **Figure 5.3c** and **5.3d**, does not show large changes between the two $B_3$-cluster structures, without ICOHP or Bader charges, we cannot determine the difference in the bonding environment.

The ICOHP analysis calculates the bond strength between a B in the $B_3$-cluster and a B in a neighboring sheet, the averages of which are found in **Table 5.1**. Similar to the ELF analysis, ICOHP data does not give a significant indication which structure has stronger bonds with its neighboring B-sheets. While the data in **Table 5.1** suggests the bonds are stronger when the $B_3$-clusters are 3.2 Å apart, they are only stronger by 0.03 eV, a value that is not statistically significant. As such, we cannot determine which structure has stronger bonds in the pure $WB_4$ material. If the average bond strength of the 3.2 Å $B_3$-clusters is indeed higher, it could mean that it is more resistant to volume changes resulting in a higher bulk modulus. However, due to its rigidity, the shear modulus, or how resistant a material is to shearing deformation, could be lower thus affecting the overall hardness of the material. In the next section, we explore how the $WB_4$ structure and bonding changes when doped with C, Si, and Zr.

### 5.3.3. Si, Zr, and C Doped $WB_4$

It has been experimentally shown that doping $WB_4$ with Si, Zr, and C changes the bulk modulus significantly[61]; theoretical calculations are used to understand why. Before understanding the bonding of doped-$WB_4$, we ran geometry optimizations to pinpoint the dopant locations in the unit cell. We optimized the geometry with each dopant placed in four different atomic positions: (1) replacing a B in the B-sheet, (2) replacing a B in the $B_3$-cluster, (3) replacing a fully occupied W, or (4) in place of a partially occupied W. **Table 5.2** includes the formation energies for each optimized geometry. Si and Zr are most energetically favorable when they sit in the partially occupied W position, while C, due to its similar size, is most favorable in the B-sheet.

**Table 5.2 Formation Energies of Doped-$WB_4$**
Formation energies obtained from geometry optimizations of $WB_4$ doped with C, Si, and Zr in four different positions: a B-sheet, a $B_3$-cluster, a fully occupied W site, or a partially occupied W site. C prefers to sit in the B-sheet while both Si and Zr replace an entire $B_3$-cluster and sit in the partially occupied W site.

| Atomic position in $WB_4$ | C doped (eV) | Si doped (eV) | Zr doped (eV) |
|---|---|---|---|
| Full occupancy B (B-sheet) | -131.5651 | -131.0374 | -126.0493 |
| Partial occupancy B (a B in the $B_3$-cluster) | -130.5202 | -129.1073 | -124.8632 |
| Full occupancy W | -126.6632 | -128.8535 | -124.7533 |
| Partial occupancy W | -125.8823 | -131.8139 | -127.4159 |

Upon obtaining the optimized geometries, we calculated the ICOHP bond strengths. Instead of comparing the average bond strengths between the clusters and sheets, to capture an accurate bonding analysis common across all dopants, we use hexagonal ICOHP sums. **Figure 5.4** shows an example of pure $WB_4$ without W along the y-axis, to show the boron clusters a) 3.2 and b) 6.4 Å apart, while c) shows $WB_4$ along the z-axis with two highlighted sets boron atoms. The purple triangle highlights a $B_3$-cluster while the red hexagon highlights the nearest neighbor Bs the cluster is bonded to directly. Only the bonds between the $B_3$-cluster (triangle) and the directly bonded B (hexagon) are summed and presented in **Table 5.3**.

**Table 5.3 Hexagonal Sums for Pure and Doped-$WB_4$**
Hexagonal sums of the nearest neighbor bonded to the B3-cluster in pure WB4, C-doped, and Si-doped WB4. This shows that the B3-clusters are always less tightly bound to the B-sheet when the clusters are 6.4 Å apart.

| Structure Type | 3.2 Å apart (eV) | 6.4 Å apart (eV) |
|---|---|---|
| Pure $WB_4$ | -105.485 | -103.008 |
| C-doped $WB_4$ | -104.652 | -103.508 |
| Si-doped $WB_4$ | -105.627 | -101.775 |

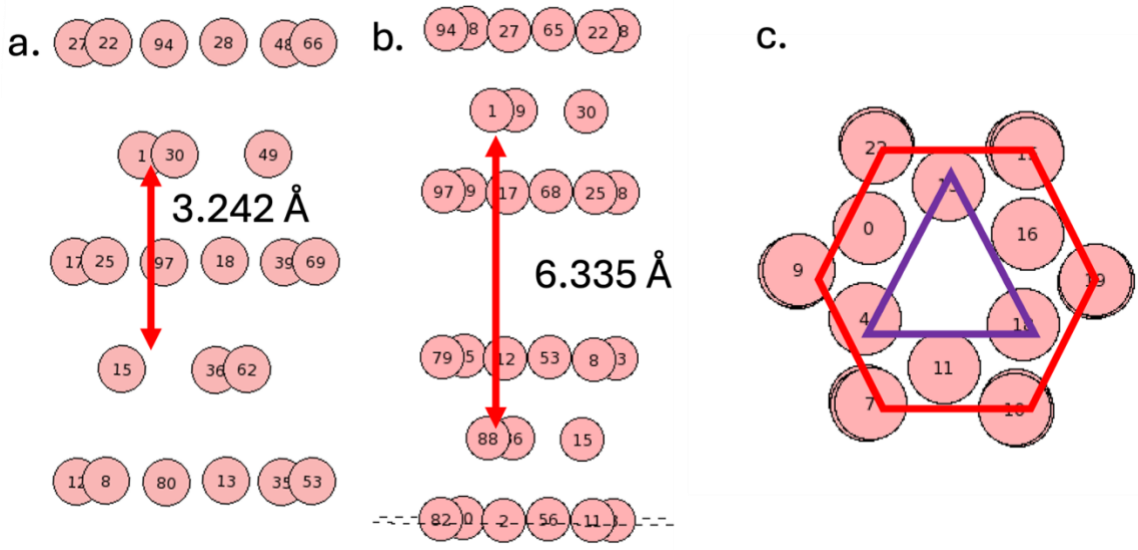


**Figure 5.4 Hexagonal Sums**
A schematic of how hexagonal sums were calculated. Only the bond strengths obtained from ICOHP of the B in the red hexagon bonded to $B_3$-cluster (purple triangle) were summed in order to obtain values presented in table 3.

**Table 5.3** shows the hexagonal sums of the two different $B_3$-cluster structures doped with C and Si compared to pure $WB_4$. Between the two structures, $B_3$-clusters 6.4 Å apart all have weaker bonds to their B-sheets compared to when the clusters are close together. This suggests that the 'cage-like' structure that is formed with the single B-sheet when the clusters are 3.2 Å apart are strong and rigid in both the pure and doped forms of $WB_4$. Because C is preferentially located in the fully occupied B site, C-doped $WB_4$ does not have homogenous B-sheets. This inhomogeneity results in the weakest bonds when the $B_3$-clusters are in a 'cage-like' configuration. This could be due to C's higher electronegativity pulling electron density away from other B's in the B-sheet

that contribute to the bonding in the hexagonal sum. Meanwhile, Si-doped $WB_4$ shows a large structural dependence. It has the highest hexagonal sum when the $B_3$-clusters are in a 'cage-like' configuration but the weakest sum when they are in an 'hour-glass' structure; this suggests a difference in bonding type. Recall that Si is preferentially located in a partially occupied W site, located in the same plane as the $B_3$-clusters. While the electronegativity of Si is lower than that of W, its size is much smaller. Si's size could have large effects on the hexagonal bonding sum if it influences the spacing between the clusters and sheets. In the next section, we explore how hardness of the samples change depending on the location of the $B_3$-clusters and the dopants.

### 5.3.4 Hardness Calculations of Pure and Doped $WB_4$

Upon determination of the two most energetically-favorable structures, we calculate the bulk and shear moduli from elastic simulations. The bulk modulus informs us on how incompressible the material is while the shear modulus informs us about the material's resistance to shape change. Experimentalists are able to measure the bulk modulus using diamond-anvil strength measurements[61,118], however the main goal is to obtain the yield strength as it is directly correlated to the Vickers Hardness. The yield strength is related to the differential strain and shear modulus using equation 5.1 as shown below.

$$DS = \frac{t}{G} \qquad \text{Eqn 5.1}$$

In which $DS$ is defined as the differential strain and is obtained from experiment, $G$ is the shear modulus, which is obtained from theory, and $t$ is the yield strength. Because the shear modulus is difficult to measure, experimentalists rely on theoretical calculations to obtain $t$. We use the experimentally obtained bulk modulus to compare with calculated values prior to using a

calculated $G$ to obtain an approximate $t$. **Table 5.4** shows the experimental and calculated bulk moduli for pure and doped $WB_4$ with the two different $B_3$-cluster configurations.

**Table 5.4 Experimental versus Calculated Bulk Modulus Values**
Experimentally obtained bulk modulus values for pure, C-, and Si-doped WB4 compared to the calculated values.

| Structure | Experimental Bulk Modulus (GPa)[61] | Computational Bulk Modulus (GPa) 3.2 Å apart | Computational Bulk Modulus (GPa) 6.4 Å apart |
|---|---|---|---|
| Pure $WB_4$ | 350 | 276.3 | 277.4 |
| C-doped $WB_4$ | 269 | 271.3 | 278.6 |
| Si-doped $WB_4$ | 287 | 270.3 | 272.2 |

While the simulations do not correctly capture the experimentally obtained bulk modulus values, we can make comparisons within the calculations. Si-doped $WB_4$ has the lowest calculated bulk modulus values in both $B_3$-cluster configurations, both of which are lower than that of the calculated pure $WB_4$. This implies extrinsic factors would be the result if experiment found an increase in bulk modulus value from pure $WB_4$. Because we found the experimental bulk modulus decreases for Si-doped $WB_4$, it suggests that doping decreases the hardness of the material. Meanwhile, C-doped $WB_4$ shows an increase in bulk modulus when the $B_3$-clusters are farther apart. In this configuration the ICOHP hexagonal sum is weaker than when the clusters are 3.2 Å apart. The combination between lower bond strength and higher bulk modulus compared to pure $WB_4$ suggests the material is less rigid and capable of higher stress resistance, resulting in a harder material. In this chapter I have shown how theoretical calculations can improve the understanding of transition metal borides by gaining insight in the geometry and bonding of the material.

## 5.4 Conclusions

Transition metal borides have been widely studied due to their unique mechanical properties. Different molecular structures of transition metal borides diversify the material properties and

applications, ranging from superhard cutting tools that are more affordable and more easily processed than diamond[131], to a more effective superconducting qubit for quantum information science.[132] My research goal was to address the electronic and vibronic origins of the diverse boride properties, with the goal of developing an understanding that would permit rational materials manipulation, and property tuning through composition and external stimuli, such as pressure or anisotropic stress.

## 5.5 Acknowledgements

This project would not have been possible without the experimental collaboration with Drs. Sarah Tolbert and Richard Kaner. Shanlin Hu was the graduate student who obtained the experimental data shown throughout this chapter. As I switched groups while still working on this project, I thank my collogues, Kirill Shumilov and Hang Yin for continuing the research.